USING INTERFEROMETRIC SYNTHETIC APERTURE RADAR DATA TO IMPROVE ESTIMATES OF HYDRAULIC HEAD IN THE SAN LUIS VALLEY, COLORADO

A DISSERTATION
SUBMITTED TO THE DEPARTMENT OF GEOPHYSICS
AND THE COMMITTEE ON GRADUATE STUDIES
OF STANFORD UNIVERSITY
IN PARTIAL FULFILLMENT OF THE REQUIREMENTS
FOR THE DEGREE OF
DOCTOR OF PHILOSOPHY

Jessica Anne Reeves

March 2013

I certify that I have read this dissertation and that, in my opinion, it is fully adequate in scope and quality as a dissertation of Doctor of Philosophy.

_____

(Rosemary Knight) Principal Advisor

I certify that I have read this dissertation and that, in my opinion, it is fully adequate in scope and quality as a dissertation of Doctor of Philosophy.

_____

(Howard Zebker)

I certify that I have read this dissertation and that, in my opinion, it is fully adequate in scope and quality as a dissertation of Doctor of Philosophy.

_____

(Mark Zoback)

Approved for the University Committee on Graduate Studies.

_____

Abstract

Remotely sensed Interferometric Synthetic Aperture Radar (InSAR) deformation data have recently been used to study confined aquifer systems in urban/arid areas. The deformation measured at the surface by InSAR is a consequence of changes in hydraulic head in the underlying confined aquifer system. Deformation in agricultural areas, such as the San Luis Valley, Colorado, is difficult to measure using InSAR because changes in the height of the vegetation can degrade the measurement by altering the positions of individual radar scatterers. Nonetheless, agricultural areas like the San Luis Valley are of great interest because of the link between the groundwater resources and the local economy.

The San Luis Valley is an 8000 km^2 valley, located mostly on the northern side of the Colorado-New Mexico border. The valley has a vibrant agricultural economy that is highly dependent on the effective management of limited water resources. State regulation established that hydraulic head levels within the confined aquifer system should be maintained within the range experienced in the years between 1978 and 2000.

Effective management of water resources in the San Luis Valley requires both seasonal changes in hydraulic head as well long term trends during this time period.

In this study we had three main goals: 1) to determine if high quality InSAR data can be collected in the San Luis Valley, 2) to determine the uncertainty of the InSAR deformation measurements, and 3) to determine to what extent the InSAR deformation data can be used to improve estimates of hydraulic head in the San Luis Valley.

We found that high quality InSAR data could be acquired from the San Luis Valley. Many small areas, left unwatered by the center-pivot irrigation systems, yield high quality InSAR data when processed using Small Baseline Subset analysis. The InSAR deformation measurements showed the same seasonal periodicity as the hydraulic head data from monitoring wells. Because no other ground-based deformation measurements have been made in the San Luis Valley we decided to use InSAR data and aquifer test data to estimate hydraulic head. We found good agreement between the estimated hydraulic head values and the measured head values made at wells (within the error bars of the head estimates). However, we acknowledge that using aquifer test data in the analysis led to errors in the hydraulic head estimates that were too large to provide the level of accuracy required for effective groundwater management.

The next step in our research was to more accurately determine the uncertainty in the InSAR deformation measurements. Addressing the uncertainty in InSAR measured deformation is critical if these data are to be used for groundwater applications as a basis

for management decisions. We developed a novel algorithm that uses supplementary hydrologic data to identify InSAR acquisitions whose measurements may have been corrupted with uncertainty due to atmospheric phase effects. We then proceeded to quantify the uncertainty in the InSAR deformation measurement due to decorrelation of radar signals. Finally, we determined how to set Small Baseline Subset analysis thresholds in order to achieve an acceptable level of uncertainty for a given application. In this way groundwater managers can provide an ideal level of uncertainty and the deformation data can be processed accordingly.

In the final chapter of this work we explored ways in which the relationship between InSAR measured deformation and measurements of hydraulic head can be combined to increase the spatial and temporal density of hydraulic head measurements in the confined aquifer system. Unlike previously studied aquifer systems, where attempts were made to match the deformation predicted by a transient groundwater flow models to the InSAR measured deformation, we focused on estimating the parameter most important for groundwater managers in the San Luis Valley, the hydraulic head. We showed how and when we can improve the estimates of hydraulic head by exploring the relationship between the spatially and temporally dense InSAR deformation data and the sparse hydraulic head measurements. We found that at three well locations where the changes in hydraulic head were sufficiently large and the aquifer sediments were relatively compressible the InSAR deformation measurements can be reliably used to estimate hydraulic head during times when no well measurements were acquired.

Acknowledgments

Going to graduate school was hands down the best decision I ever made. Not because of all the amazing groundbreaking science I have done, I use the word groundbreaking loosely of course, but because of all the amazing people that have helped me along the way. Stanford is a place of humans helping humans make discoveries.

The one and only Rosemary Knight is to thank for making me the scientist I am today. Although my writing skills are still in progress, as shown in this thesis, I can only hope that some of her other amazing abilities have rubbed off on me. Howard Zebker is the best co-advisor a girl could ask for. He has an amazing ability to tell you that your work is completely wrong without making you feel terrible; a real perk in an advisor. Willem Schreuder and Eric Harmon were the best collaborators on Earth. They answer emails at all times of the day, any day of the week. I would also like to say thanks to Mark Zoback, one of my committee members from the beginning. Although Mark has very little experience in the world of hydrogeology

he was always able to pick out the flaw in my scientific reasoning. And last but not least, Peter Kitanidis, without your classes and help with the final chapter of this thesis I am sure I would still be processing data right now, so thank you.

Almost more important than the technical support was the emotional support that was provided by the people around me. Most importantly Katherine Dlubac and Denys Grombacher, who always knew what I was going through better than anyone. A special thanks to my past officemates Annemarie Baltay and Justin Brown. Needless to say, best office ever. However, topping all the people at Stanford are my dearest of friends: Dan Aukes, Mike Stern, Kristen Ericksson and Zach Brown. Let me just say, stay classy and thanks for stopping by.

If anyone is to thank for me both starting and finishing this Ph.D. it is my parents. They yelled at me until they were blue in the face to leave Toronto for California, and luckily I went. They made me appreciate how lovely it is to work on challenging and new problems every day. I would also like to un-thank my brother David for beating me out of school, way to make an older sister feel bad. And finally, thank you David Cameron. From day 1 to day 1944 you saw it all, and made sure I toughed it out.

Funding for my research has come from a number of sources: the Stanford School of Earth Sciences, the Nelson Award, and NASA. Thank you so much for making a philosophical doctor out of me.

Contents

List of Figures

List of Tables

Chapter 1
Introduction

1.1 Problem Definition, groundwater in the San Luis Valley

The San Luis Valley (SLV) is an 8000 km^2 high-altitude valley, located mostly on the northern side of the Colorado-New Mexico border. The Rio Grande River runs through the center of the SLV to the downstream states of New Mexico and Texas. The valley has a vibrant agricultural economy that is highly dependent on the effective management of limited water resources. In addition to providing irrigation water to over 600,000 acres of productive cropland, the surface water and groundwater in the SLV serve a variety of municipal and commercial interests, and provide invaluable ecological benefits throughout the valley. Water management in the valley is further complicated by the obligation to deliver a portion of the water in the Rio Grande River to New Mexico and Texas each year, in compliance with the 1938 Rio Grande Compact. In 2006 the Confined Aquifer Rules decision made by the State of Colorado held that the San Luis basin was over-appropriated and that any new appropriations from the confined aquifer

must be fully augmented/replaced [*Kuenhold*, 2006]. Further, legislation passed in 2004 established that hydraulic head levels within the confined aquifer system should be maintained within the range experienced in the years between 1978 and 2000. What is required in the SLV is the ability to manage the various demands for water from the confined aquifer system while ensuring long-term sustainability. For these reasons groundwater managers in the SLV are interested in both seasonal changes in hydraulic head as well long term trends during this time period.

The Colorado Water Conservation Board and the Colorado Division of Water Resources have developed the Rio Grand Decision Support System (RGDSS), a project run by a number of co-operating organizations including the Rio Grande Water Conservation District (RGWCD) to quantitatively study the water resources in the SLV (http://www.rgwcd.org/Index.htm). The RGDSS includes a hydrogeologic database and a MODFLOW finite-difference groundwater flow model that can be used to evaluate historic and proposed groundwater management practices, develop a groundwater budget, and identify areas for future research. The groundwater model created for the RGDSS was derived from detailed studies of the SLV by federal, state and local agencies that span more than 100 years, and includes remote sensing data, site specific geophysical data, aerial photography, hydrologic data and agricultural records. One of the main goals of the RGDSS groundwater model is be able to predict hydraulic head in the confined aquifer system. In doing so the model becomes a viable tool in terms of management and regulation under the Confined Aquifer Rules decision.

The critical challenge for the RGDSS, and the main motivation for the research presented here, is acquiring sufficiently dense data to characterize the spatially heterogeneous, time-varying behavior of the hydraulic head in this large-scale (8000 km^2) model. At present the MODFLOW groundwater flow model is not able to predict hydraulic head everywhere in the confined aquifer system due to a derth of calibration points, i.e. hydraulic head measurements from monitoring wells [*RGDSS*, 2005]. With only 328 wells monitoring hydraulic head in the confined aquifer system it is easy to understand why these data cannot supply enough information to fully characterize this 8000 km^2 area.

1.2 Motivation, the use of remotely sensed InSAR data

Remote sensing data can provide measurements with high spatial and temporal resolution over large areas. Of particular relevance to the characterization of groundwater systems is Interferometric Synthetic Aperture Radar (InSAR), a remote sensing method that maps the relative ground surface deformation. The deformation of the ground surface, derived here from InSAR data, is directly related to changes in the thickness of the confined aquifer due to recharge and withdrawal of groundwater. Synthetic Aperture Radar (SAR) is a microwave imaging system, which uses a radar antenna mounted on an airborne or satellite-based platform to transmit and receive electromagnetic (EM) waves. The difference in the phase of the EM wave as measured between two acquisitions can be related to deformation of Earth's surface. The European Space Agency's (ESA) ERS-1 and ERS-2 satellites collected data over the San Luis Valley (SLV) from 1992 to 2001 and again from 2005 to 2011. The final processed deformation measurements derived

from the ERS data have a spatial resolution of 50 m with a temporal sampling of 35 days. The change in thickness of the confined aquifer system may be able to inform groundwater managers in the SLV about groundwater levels in the confined aquifer system during that important time period during the 1990's.

InSAR has been used a number of times with the goal of investigating groundwater problems in urban/arid areas [*Galloway et al.*, 1998; *Amelung et al.*, 1999; *Watson et al.*, 2002; *Schmidt and Burgmann*, 2003; *Hoffmann et al.*, 2001; *Hoffmann et al.*, 2003; *Bell et al.*, 2008; *Wisely and Schmidt*, 2010; *Calderhead et al., 2011; Gonzalez et al., 2011*]. The SLV is an agricultural area, where crop growth, irrigation, land erosion, and harvesting cycles can all seriously degrade the InSAR data by perturbing the positions of individual radar scatterers. Although it is important to understand hydraulic head changes in urban areas, agricultural areas like the SLV are of great interest because of the link between the groundwater resources and the local economy.

There are three main ways in which InSAR data have been previously used to address groundwater problems: 1) to map the spatial extent of aquifer system deformation, 2) to estimate aquifer compressibility parameters, and 3) to calibrate groundwater flow models. Preliminary research on this topic began with the use of InSAR deformation measurements to map aquifer system deformation [*Galloway et al.*, 1998; *Amelung et al.*, 1999; *Watson et al.*, 2002] as well as monitor deformation over time [*Schmidt and Burgmann*, 2003]. The relationship between hydraulic head levels in a confined aquifer and the thickness of a confined aquifer, which will be discussed in Section 2.2 'Aquifer

deformation background', has been previously used to estimate aquifer compressibility parameters [*Hoffmann et al.*, 2001; *Hoffmann et al.*, 2003; *Bell et al.*, 2008; *Wisely and Schmidt*, 2010]. These parameters are some of the necessary inputs to any transient groundwater flow model.

A number of authors have used InSAR deformation data as added constraints for transient groundwater flow models, with the goal of improving the predictability of the hydraulic head [*Hoffman, 2003; Calderhead, 2011; Gonzalez, 2011*]. It is important to note that these studies focused on areas where the authors observed permanent deformation due to excessive groundwater extraction. In general the InSAR data were used to calibrate the model-predicted permanent deformation. For example *Hoffmann et al.* (2003) calibrated a MODFLOW finite difference groundwater flow model for the Antelope Valley, California. The estimated aquifer compressibility parameters allowed the model to reproduce leveling line surveys measuring surface deformation, but the ability of the model to predict hydraulic head was not improved. *Calderhead et al.* (2011) used the InSAR deformation measurements as additional calibration parameters in a regional scale model of the Toluca Valley, Mexico. By using InSAR, they showed that these data can provide spatially dense estimates of the aquifer compressibility parameters. *Gonzalez et al.* (2011) observed long term inelastic deformation in the Guadalentín Basin, Spain. They too modeled the deformation and incorporated the InSAR deformation data as calibration parameters. However, in both *Gonzalez et al.* (2011) and *Calderhead et al.* (2011) the authors did not discuss the predictive capabilities of the groundwater flow model.

In our research we use an approach that does not involve developing a large over-parameterized groundwater flow model. Rather, our goal is to use the direct relationship between deformation and hydraulic head at the well locations to interpolate and extrapolate the hydraulic head data both spatially and temporally.

1.3 Objectives and Contributions

The San Luis Valley (SLV) is of particular interest because of the regulations set forward by the Confined Aquifer Rules decision in 2006. Although the Rio Grande Decision Support System (RGDSS) has attempted to predict hydraulic head using a MODFLOW groundwater flow model, the lack of spatially and temporally dense hydraulic head measurements has made it difficult to use this model to implement the courts ruling. It is thus the prime objective of this work to evaluate whether or not InSAR deformation data can be used to estimate hydraulic head in the SLV. The main questions addressed here are:

1. Can high quality deformation measurements be made in the agricultural areas of the SLV?
2. What are the uncertainties associated with the InSAR deformation measurement in the SLV?
3. Can we estimate hydraulic head from InSAR deformation measurements made in the SLV?

This work constitutes the first systematic investigation into the application of InSAR deformation measurements to estimate hydraulic head in an agricultural area. More specifically the contributions of this work are as follows:

- Modification of a time-series processing algorithm to properly estimate deformation signals produced by seasonal pumping and recharge of groundwater aquifers in agricultural areas.
- Development of an extensive time-series of InSAR deformation maps for the San Luis Valley, Colorado, visualizing the spatial and temporal characteristics of land surface deformation in this region.
- Verification that high quality InSAR deformation measurements can be made in agricultural areas like the San Luis Valley.
- Estimatation of the uncertainty in the InSAR deformation measurements and propagated this uncertainty through the data processing chain.
- Adaptation of a time-series processing algorithm such that high quality data are selected based upon the uncertainty of the final deformation time-series.
- Investigation of the spatial structure of the InSAR measured deformation dataset and the hydraulic head dataset in the SLV.
- Prediction of hydraulic head back in time at three well locations in the SLV.

Chapter 2
Theoretical Background

2.1 InSAR Background

In this section we outline the basics of Interferometric Synthetic Aperture Radar (InSAR) processing, with specific reference to the measurement of deformation in the San Luis Valley (SLV), Colorado. We begin by outlining the components of the interferometric phase measurement and the InSAR processing flow. The different components of the uncertainty in the deformation are outlined as the theoretical background for Chapter 5. We end this section with an introduction to an advanced processing technique known as Small Baseline Subset (SBAS) analysis, which we used to process the data from the SLV.

2.1.1 InSAR imaging of deformation

Synthetic Aperture Radar (SAR) is a microwave imaging system, which uses a radar antenna mounted on an airborne or satellite-based platform to transmit and receive electromagnetic (EM) waves. The ERS-1 and ERS-2 satellites used in this study have a

repeat cycle of 35 days and operate at a frequency of 5.3 GHz. The antenna footprint maps a continuous 100 km wide swath along the direction of flight (the azimuth direction), which is known as a track. Perpendicular to the azimuth direction is the range direction, moving out away from the satellite's path (see Figure 2.1). In order to ease processing each track of data is divided into square frames (See Figure 2.2). Each pixel in a frame contains a complex number describing the reflected amplitude and phase of the EM wave from a resolution cell on the ground, which in this study is on the order of 5 m by 25 m.

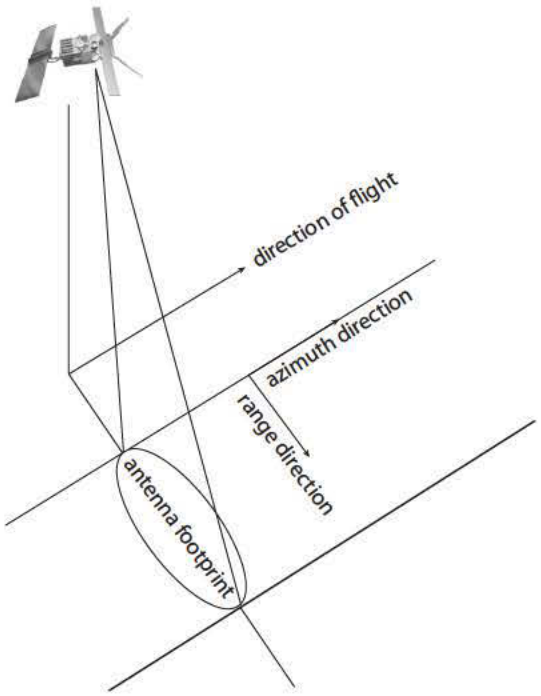

Figure 2.1: The imaging geometry for satellite based SAR systems.

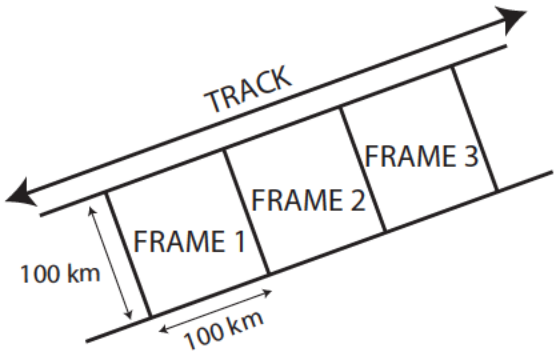

Figure 2.2: A schematic of the packaging of SAR data into tracks and frames, approximately 100 km by 100 km.

Standard InSAR processing techniques combine two SAR scenes of the same area, acquired at different times. Calculating the difference in the phase component ($\Delta\phi$) of the reflected signals is known as radar interferometry, and the image of $\Delta\phi$ for all pixels is known as an interferogram [*Zebker et al.*, 1994]. Data are collected along the line-of-sight (LOS) direction, from the antenna to Earth's surface. The look angle is defined as the angle between the LOS and the normal to Earth's surface. For the ERS satellites the look angle is approximately 23 degrees, so the change in LOS distance from the antenna to the surface is approximately equal to the change in vertical distance to the surface. If the effects of topography are removed then $\Delta\phi$ can provide an accurate measure of the change in the elevation of the land surface. Pixels are often spatially averaged to correspond to a 50 m by 50 m resolution cell to improve the signal-to-noise ratio of the observed interferometric phase. Because of the cyclic nature of phase, $\Delta\phi$ will only be known within 2π radians; this is called the wrapped phase. The process of estimating and adding the unknown correct integer multiple of 2π to $\Delta\phi$ is called phase unwrapping [*Chen and Zebker, 2002*].

The measured difference in the phase of the two signals $\Delta\phi$ is the sum of six parts [*Zebker et al.*, 1994; *Ferretti et al.*, 2000]:

$$\Delta\phi = \Delta\phi_{def} + \Delta\phi_{topo} + \Delta\phi_{orb} + \Delta\phi_{ip} + \Delta\phi_{atm} + \Delta\phi_{n} \tag{2.1}$$

where $\Delta\phi_{def}$ is the phase change due to the deformation of the ground surface, $\Delta\phi_{topo}$ is the phase change due to topography, $\Delta\phi_{ip}$ is the phase change due to integer phase ambiguities, $\Delta\phi_{orb}$ is the phase change due to orbital errors, $\Delta\phi_{atm}$ is the phase change due to atmospheric phase effects and $\Delta\phi_{n}$ is the phase change due to random phase noise. The different components can be considered signal or noise in different applications, however for this study we are interested in the phase change due to the deformation of the ground surface. $\Delta\phi_{def}$ is related to the deformation (Δd) by

$$\Delta\phi_{def} = \frac{2\pi}{\lambda}(2\Delta d) = \frac{4\pi}{\lambda}\Delta d, \tag{2.2}$$

where λ is the wavelength of the radar system (see schematic in Figure 2.3). The noise components $\Delta\phi_{topo}$ and $\Delta\phi_{orb}$ must be removed and the noise components $\Delta\phi_{ip}$, $\Delta\phi_{atm}$ and $\Delta\phi_{n}$ must be mitigated in order to accurately determine $\Delta\phi_{def}$. To follow is a description of how the components $\Delta\phi_{topo}$ and $\Delta\phi_{orb}$ can be removed from the measurement of the change in phase. We will reserve the detailed discussion about quantification of the other components of uncertainty until section 2.1.2.

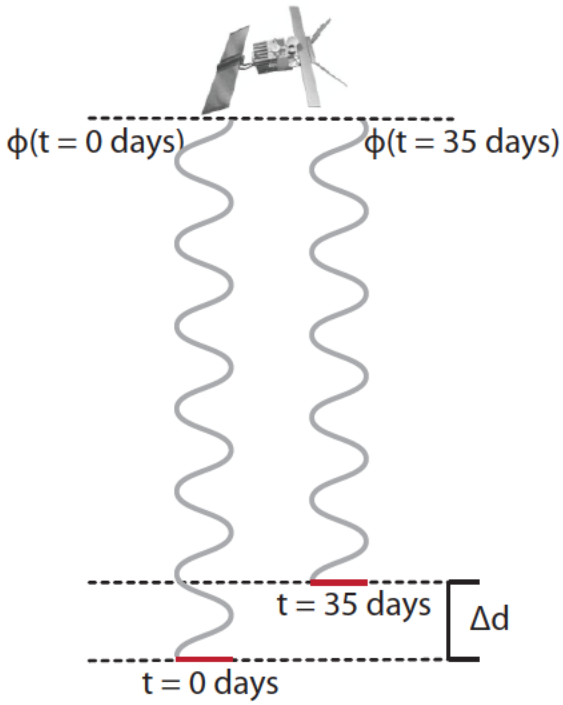

Figure 2.3: A schematic of how the change in phase of the EM wave relates to the change in surface deformation.

$\Delta\phi_{topo}$ arises if the satellite views the surface from a slightly different parallax angle at the two acquisition times. This means that different points on the surface will be at different positions from the antenna. $\Delta\phi_{topo}$ can easily be removed if there is accurate information about the imaging geometry and the surface topography from a digital elevation model (DEM) that has an elevation accuracy between 10 and 100 m [*Zebker et al.*, 1994; *Hanssen*, 2001]. If there are significant errors in the DEM, advanced processing techniques are used to correct for this effect. This correction is called the topographic correction and will be discussed further in section 2.1.3.

Using incorrect orbital parameters to process SAR data also adds uncertainty to the InSAR deformation measurement ($\Delta\phi_{orb}$). Modest orbital parameter errors result in a nearly planar change in phase across the interferogram that can be much larger than the deformation component of the phase. This planar trend can be removed by subtracting a best-fit plane from each interferogram [*Lauknes et al.*, 2005].

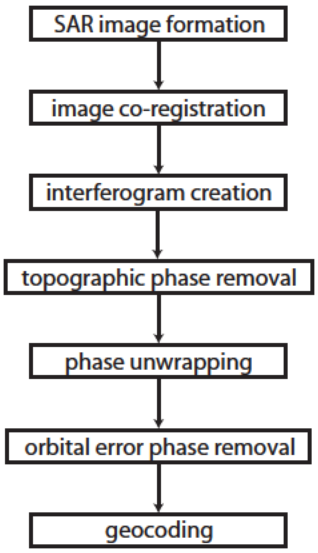

Figure 2.4: Processing flow to create deformation images.

Figure 2.4 outlines the processing flow to go from SAR images to deformation images. First, the two SAR images are co-registered, which means that they are spatially aligned using the amplitude returns of the radar. The interferogram is formed by subtracting the phase of scene 1 from the phase of scene 2 for all pixels. $\Delta\phi_{topo}$ is removed using a digital elevation model, as discussed previously in this section. Then phase unwrapping is applied, where the modulo 2π phase is converted into an absolute phase measurement. On the unwrapped phase the $\Delta\phi_{orb}$ is removed as described in this section. And finally the

result is geocoded, latitude and longitude co-ordinates are determined, so that the exact location of the deformation at each pixel is known.

2.1.2 Uncertainty in the InSAR deformation measurement

Three major components remain and contribute to uncertainty in the measurement of interferometric phase: integer phase ambiguities ($\Delta\phi_{ip}$), atmospheric phase effects ($\Delta\phi_{atm}$) and decorrelation of radar signals ($\Delta\phi_{n}$). When we do not remove these uncertainty components we can see in equation 2.3 that this uncertainty will propagate through to an uncertainty in the InSAR deformation measurement:

$$\Delta d = \frac{\lambda}{4\pi}\Delta\phi = \frac{\lambda}{4\pi}\left(\Delta\phi_{def} + \Delta\phi_{ip} + \Delta\phi_{atm} + \Delta\phi_{n}\right). \qquad (2.3)$$

These components were discussed at length in *Hanssen* (2001). In Chapter 5 of this thesis we will address two of these components: atmospheric phase effects and decorrelation of radar signals, as we have found that these two components have the largest effect on the uncertainty of the InSAR deformation measurement in the SLV. An outline of the theory behind these two components is given in this section. The other component, integer phase ambiguities, did not have a large effect on the uncertainty of the deformation in the SLV. We will, however, discuss the theory behind this component in the paragraph to follow.

InSAR data processing includes a step called phase unwrapping, in which phases measured modulo 2π are converted into a relative phase measurement by estimating and

adding the correct number of integer cycles of phase into the measurement. If there is a considerable amount of noise in the data the algorithm will incorrectly estimate the phase by some integer multiple of 2π, this is known as an integer phase ambiguity ($\Delta\phi_{ip}$). *Usai* (2003) proposed a method for estimating this component of uncertainty by recognizing the "closed-loop" condition of the change in phase in three interferograms:

$$\phi_{t_1 t_2} + \phi_{t_2 t_3} + \phi_{t_3 t_1} = 0, \tag{2.4}$$

where $\phi_{t_i t_j}$ is the interferometric phase from scene i and scene j. However, using this method with more interferograms is not simple and has not been attempted on datasets with a large number of interferograms [*Gonzalez and Fernandez*, 2011]. As in *Gonzalez and Fernandez* (2011), poor quality interferograms from the SLV were omitted, allowing us to assume that this component of uncertainty is small.

If the atmospheric humidity, temperature, and pressure change significantly between the two SAR scenes, the refractive index of the atmosphere will change. As the EM wave passes through the atmosphere, the velocity of the EM wave will change and affect the measured phase. The phase change due to atmospheric effects ($\Delta\phi_{atm}$) is uncorrelated in time, because the atmosphere changes randomly from one acquisition day to the next, but correlated in space, because cloud cover, temperature, and pressure are continuous in space over distances on the order of hundreds of meters [*Hanssen*, 1998; 2001]. For these reasons it is common to use temporal and spatial filtering to remove this error component [*Zebker et al.*, 1997; *Ferretti et al.*, 2001]. However, these atmospheric effects are highly

variable, often dominating the change in phase observed in interferograms. The limited number of scenes used in any single analysis makes the associated uncertainty difficult to quantify. *Simons et al.* (2002) estimated the uncertainty due to atmospheric phase effects by looking at the root mean squared (RMS) difference between each interferogram and all other interferograms in one data set. Because they knew that any surface deformation in their study area was occurring slowly, they were able to attribute the RMS difference to the uncertainty due solely to atmospheric phase effects. However, this method assumes the same amount of uncertainty for every pixel in a given interferogram and does not accurately represent the spatial variations in the uncertainty. *Onn and Zebker* (2006) used Global Positioning System (GPS) estimates of water vapor to decrease the amount of uncertainty in the InSAR deformation measurements, in some cases as much as 31%. However, this analysis involves having a network of GPS measurements available, which is not the case for many field sites.

A more recent study by *Knospe and Jonsson* (2010) investigated how atmospheric phase effects vary spatially. In order to isolate the uncertainty due to atmospheric phase effects they processed two interferograms that spanned a single day. They assumed that no deformation was taking place over the time span of that day($\Delta\phi_{def} = 0$), and that $\Delta\phi_{ip}$ and $\Delta\phi_{n}$ were also very small. This means that the measure phase change was all due to changes in atmospheric conditions. They then created two variogram models that quantified the spatial variability of the uncertainty. The variogram models were then used to represent the uncertainty due to atmospheric phase effects for a synthetic data set. They showed that the uncertainty in the final deformation estimates was less when the

variogram models were used to estimate the uncertainty due to atmospheric phase effects. However, they stated that it is important to know which variogram model best represents the uncertainty due to atmospheric phase effects for a given data set. Many applications would not have a set of interferograms that span a single day, and hence would not produce an appropriate variogram model of the uncertainty due to atmospheric phase effects. In Chapter 5 we discuss how this component of uncertainty can be mitigated in the data from the SLV.

The phase change due to phase noise ($\Delta\phi_n$) is caused by signal decorrelation and cannot readily be compensated for without sacrificing spatial resolution. For a given pixel in an interferogram the coherence is calculated as a quality measure for the phase difference $\Delta\phi_n$ between two SAR scenes at that point. The complex coherence (γ) is defined as follows:

$$\gamma = \frac{\left\langle S_1 S_2^* \right\rangle}{\sqrt{\left\langle S_1 S_1^* \right\rangle \left\langle S_2 S_2^* \right\rangle}} \tag{2.5}$$

where $\langle\ \rangle$ denotes the expected value, S_1 and S_2 are the complex values of SAR scene 1 and SAR scene 2, and S_1^* and S_2^* are the complex conjugates of SAR scene 1 and SAR scene 2 for a small sample of pixels around the pixel in question. Often the magnitude of the complex coherence is used, referred to as only the coherence, which can range from 0 to 1. An interferogram is described as coherent/well correlated, if many of the pixels have coherence near 1; or as incoherent/decorrelated, if many of the pixels have coherence near 0.

The coherence can be described as the product of the thermal coherence γ_{therm}, the spatial coherence γ_{spat} and the temporal coherence γ_{temp} [*Zebker and Villasenor*, 1992]:

$$\gamma = \gamma_{therm} \cdot \gamma_{spat} \cdot \gamma_{temp} , \tag{2.6}$$

where γ_{therm} quantifies the system noise, a characteristic of the system configuration; γ_{spat} is a factor corresponding to the viewing angle of the satellite between the acquisition of the two scenes, as described above as a parallax effect. The reflection from a scattering area viewed at one angle will be different when viewed at another angle. This change in viewing angle is quantified by the spatial distance between the two satellite positions, the spatial baseline.

The most difficult effect to deal with is the temporal coherence γ_{temp}. Temporal decorrelation follows from wavelength-scale changes in the positions of scatterers within each resolution cell between the acquisition times of the two scenes. The time between two scenes is called the temporal baseline; long temporal baselines tend to decrease γ_{temp}. A surface can decorrelate with time due to processes or activities such as seasonal vegetation changes, erosion of the land surface, agricultural activity, or construction. The best way to mitigate this effect is to form interferograms from scene pairs with small temporal baselines. This concept of using scene pairs with small baselines will be discussed further in the following section where it is implemented via an advanced processing technique.

2.1.3 Small Baseline Subset (SBAS) analysis

The SLV is an agricultural area where crop growth, irrigation, land erosion and harvesting cycles can all change the height of the imaged surface between the acquisition of any two SAR scenes, leading to decorrelation of the signals. A recently developed technique, small baseline subset (SBAS) analysis, combines the coherent areas in a series of interferograms to produce a map of deformation time-series [*Berardino et al.*, 2002]. Phase decorrelation is minimized by imposing constraints on the temporal and spatial baselines for each pair of scenes that are interfered.

The basic principle underlying SBAS is proper interferogram selection combined with a least squares (LS) analysis of the phases in the resulting unwrapped interferograms. Interferogram selection is illustrated in Figure 2.5, a plot of spatial versus temporal baseline for all available SAR scenes from an area. Each scene is shown as a circle with the spatial and temporal baselines plotted relative to the first scene. Lines, which signify an interferogram, connect scenes if the spatial and temporal baselines are below some selected threshold. In general, a smaller spatial baseline leads to better coherence, therefore the goal is to minimize the spatial baseline threshold for the set of interferograms. The temporal baseline threshold is dependent on how rapidly the height of the vegetation changes with time in a given area and so, for example, could be 6 years for areas in an arid climate, but a few months for vegetated areas. Each group of connected scenes is known as a small baseline subset. As long as the subsets overlap for some period of time, a singular value decomposition (SVD) can be used to solve for a

time-series of deformation, relative to the first scene.

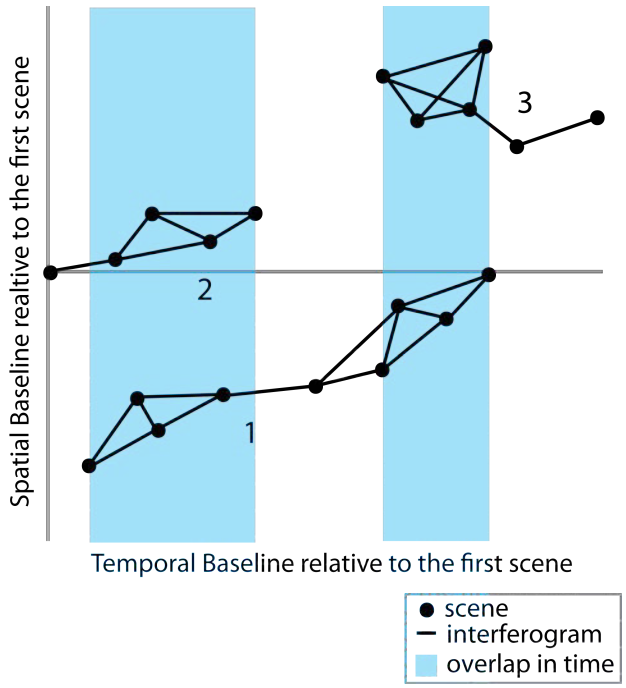

Figure 2.5: Example spatial vs. temporal baseline plot with 3 small baseline subsets. Subset 1 and 2 overlap in the first blue shaded region, and subset 1 and 3 overlap in the second blue shaded region. This dataset will be able to produce a time series that spans from the first scene to the last scene plotted.

The mean coherence for every pixel is then calculated and a threshold applied, such that only highly coherent pixels are used in the remainder of the analysis. In the development of the SBAS method, *Berardino et al.* (2002) and *Lauknes* (2004) determined values for the threshold: they set thresholds $\gamma > 0.25$ in at least 30% of the interferograms and $\gamma > 0.3$ in at least 30% of the interferograms respectively. The goal of setting this threshold is to select pixels that have high coherence through time while still selecting enough pixels to properly unwrap the interferometric phase.

We will now review the mathematical formulation from *Berardino et al.* (2002) that describes the SBAS technique as performed on the selected pixels. Let us consider N + 1 SAR scenes acquired at times (t_0, t_1,…, t_N). Each scene must be able to interfere with one other scene, so the minimum number for each subset is two scenes. If N is odd, the number of different interferograms M is given by:

$$\frac{N+1}{2} \le M \le N\left(\frac{N+1}{2}\right). \tag{2.7}$$

If we consider the j^{th} interferogram made with SAR scenes at t_A and t_B we can define the change in phase measured at each pixel position in terms of range direction and azimuth direction (x,r) as follows:

$$\begin{aligned}\Delta\Phi(x,r) &= \Phi(t_B,x,r) - \Phi(t_A,x,r) \\ &\approx \frac{4\pi}{\lambda}\left[d(t_B,x,r) - d(t_A,x,r)\right],\end{aligned} \tag{2.8}$$

where $d(t_B,x,r)$ is the deformation at time t_B relative to zero deformation at time t_0 and $d(t_A,x,r)$ is the deformation at time t_A relative to zero deformation at time t_0. If we look at all deformation relative to the time t_0 then the phase time series becomes $\Phi(t_i,x,r) \approx 4\pi d(t_i,x,r)/\lambda$, for i = 1,…, N. For this initial description of the analysis we ignore all phase change due to atmospheric effects, topographic effects and phase noise,

as our goal in processing is to remove all components of the signal not related to the deformation. We also assume that the phase for each pixel is properly unwrapped. For the remainder of the solution we will look at the deformation time series for one pixel, so the (x,r) dependence drops out.

We have N unknowns for the phase which are needed to compute deformation relative to t_0:

$$\Phi^T = [\Phi(t_1),...,\Phi(t_N)] \tag{2.9}$$

and we have M data points from the computed interferograms:

$$\Delta\Phi^T = [\Delta\Phi_1,...,\Delta\Phi_M]. \tag{2.10}$$

We relate our data to our unknowns with M equations as follows:

$$\Delta\Phi_j = \Phi(t_{B_j}) - \Phi(t_{A_j}) \qquad j = 1,...,M \tag{2.11}$$

where $\Phi(t_{A_j})$ is the phase at the time of scene A and $\Phi(t_{B_j})$ is the phase at the time of scene B. This gives us a system of M equations and N unknowns with the matrix representation:

$$\mathbf{A}\Phi = \Delta\Phi. \tag{2.12}$$

The matrix $\mathbf{A}$ outlines the set of interferograms from the available data. We can solve for Φ in equation 2.11 by inverting the matrix $\mathbf{A}$, i.e. performing a SVD of $\mathbf{A}$. The formulation given with equations 2.7 – 2.12 is the basic least squares inversion problem. In practice there are other steps that account for prior information about the type of deformation, the topographic correction, and atmospheric effects. For thoroughness we outline the steps of what we call 'conventional SBAS analysis', which is based upon the processing flow described in *Berardino et al*. (2002).

The processing flow for conventional SBAS analysis is shown in Figure 2.6. Square boxes are used to define objects and circles to define actions performed on those objects. In *Berardino et al*. (2002) prior information about the deformation is used to define a low-pass deformation model that can capture the low frequency component of the deformation. This model is often chosen to be a simple linear, quadratic or sine function. The authors start by unwrapping the interferometric phases and then apply 'Inversion 1', shown in Figure 2.6. 'Inversion 1' estimates the parameters of the low-pass deformation model and the topographic correction. The phase associated with these two components is then subtracted from the wrapped interferometric phases. The remaining phase is associated with atmospheric phase effects and decorrelation. This phase is unwrapped and then added back to the phase associated with the low pass deformation model. On these data 'Inversion 2' is applied, yielding a phase estimate at each acquisition time.

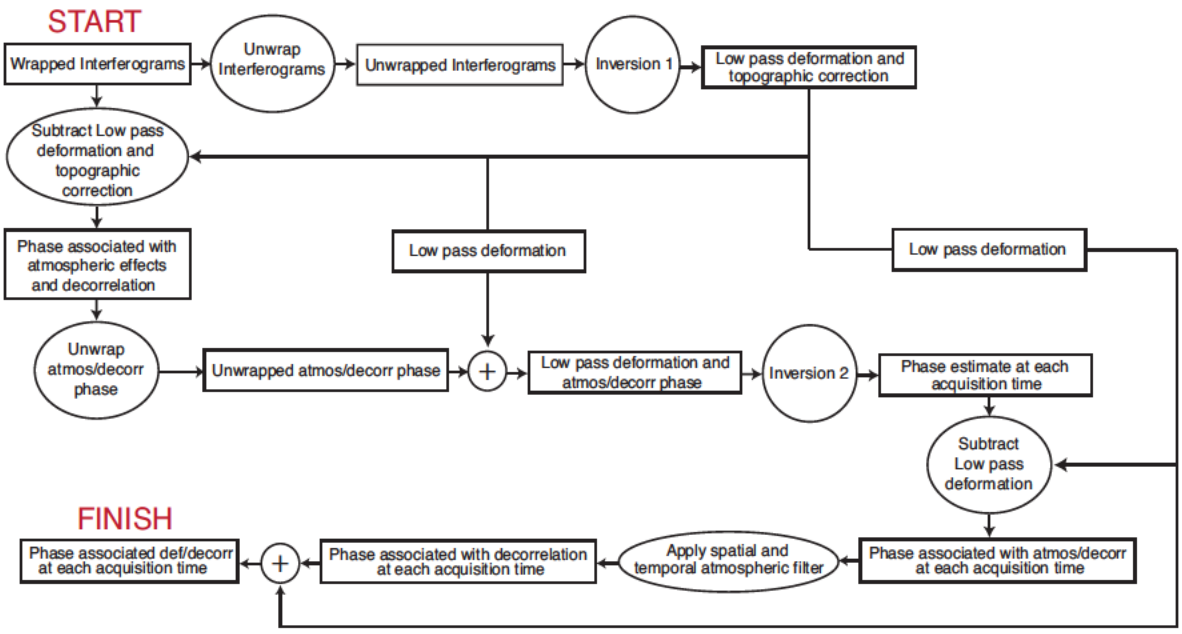

Figure 2.6: The conventional Small Baseline Subset (SBAS) analysis processing algorithm from *Berardino et al.* (2002).

The phase estimate at each acquisition time initially contains uncertainties due to atmospheric phase effects and decorrelation of radar signals. To isolate these uncertainties the low pass deformation is subtracted again. Because the phase associated with atmospheric phase effects is not correlated over time and is well correlated in space a temporal filter and spatial filter can be applied to diminish the effect of the atmosphere on the phase measurement. The remaining phase measurement is added back to the low pass deformation component and the result is a time-series of phase without uncertainties due to atmospheric phase effects. This conventional form of SBAS analysis will act as a starting point for a modified version of SBAS analysis presented in section 5.5. The modified version is specific to applications involving deformation due to seasonally variable groundwater extraction and recharge.

2.2 Aquifer deformation background

In this section we outline the basics of aquifer deformation theory. We begin by reviewing the analytical equations that relate changes in hydraulic head in confined aquifer systems to aquifer system deformation. We finish this section with a short review of coupled hydromechanical systems that will be considered at the field site in the San Luis Valley (SLV), Colorado.

2.2.1 Theoretical definitions

An aquifer is a geologic system, often taking the form of a permeable sedimentary unit, from which economical amounts of water can be pumped. Aquifers can be unconfined, if the system is exposed to atmospheric pressure, or confined, if the system is kept at a pressure higher than atmospheric. Aquitards or confining layers are low permeability layers that confine fluid pressures in the underlying confined aquifers. The low permeability material of the confining layer is generally clay or silt. We review below a summary of aquifer deformation theory as it applies to InSAR deformation data [*Hoffmann*, 2003].

The theory of aquifer deformation was first formalized in terms of Terzaghi's theory of poroelasticity [*Terzaghi*, 1925]:

$$\sigma' = \sigma - p \tag{2.13}$$

where the σ', effective stress, is equal to σ, the total stress on the aquifer system, minus p, the pore pressure. One can express a change in pore pressure, Δp, as a change in hydraulic head, Δh, which can be measured from wells that are sampling the aquifer system [*Fetter*, 2001]:

$$\Delta h = \Delta p / \rho g \tag{2.14}$$

where g is acceleration due to gravity and ρ is the density of water. In confined aquifer systems one assumes that the total stress does not change ($\Delta\sigma = 0$), i.e. the stress induced by the overburden is not changing. However, stress change occurs as water is withdrawn from the pore space ($-\Delta h$). The decrease in pore water pressure results in an effective stress increase ($\Delta\sigma'$), which is born by the aquifer system skeleton

$$\Delta\sigma' = -\rho g \Delta h \tag{2.15}$$

It is the change in effective stress that causes the deformation of sediments.

Terzaghi's theory was expanded upon by *Biot* (1941) to investigate the effects of 3D deformation. If the following assumptions are made: a) down into Earth is one of the principle stress directions and b) the lateral extent of the aquifer is much greater than the vertical extent, then only the vertical portion of the effective stress (σ_z') is relevant. The partial differential equation that results from combining Darcy's Law for fluid flow with the continuity equation is known as the one dimensional diffusion equation:

$$\frac{K_v}{\rho g}\frac{\partial^2 p}{\partial z^2} = (\alpha + n\beta)\frac{\partial p}{\partial t} \quad . \tag{2.16}$$

In this equation K_v is the vertical hydraulic conductivity of the aquifer system [m/s], α is the compressibility of the rock matrix [1/(N/m^2)], β is the compressibility of the fluid [1/(N/m^2)], and n is the porosity. Substituting hydraulic head for pore pressure in equation 2.15 gives

$$K_v \frac{\partial^2 h}{\partial z^2} = \rho g(\alpha + n\beta)\frac{\partial h}{\partial t} \quad . \tag{2.17}$$

The term $\rho g(\alpha + n\beta)$ represents the compressibility of the system, and is known as the specific storage (S_s). The specific storage is a material property defined as the volume of water expelled from a unit volume of the aquifer system due to a unit decline in hydraulic head [*Todd*, 1980].

Analytical solutions are known for equation 2.17 given certain boundary conditions. For an aquifer system with initial thickness b_0, initial hydraulic head h_0 and a step decrease in hydraulic head Δh_b at each of the layer boundaries ($\pm b_0/2$) the solution is an infinite series [*Carslaw and Jaeger*, 1959]:

$$\Delta h(z,t) = h(z,t) - h_0 = \Delta h_b - \frac{4\Delta h_b}{\pi}\sum_{m=0}^{\infty}\frac{(-1)^m}{2m+1}e^{-\frac{\pi^2}{4}\frac{t}{\tau_m}}\cos(\frac{(2m+1)\pi z}{b_0}) \tag{2.18}$$

$$\text{where } \tau_m = \frac{\left(\frac{b_0}{2}\right)^2 S_s}{(2m+1)^2 K_v}.$$

All of the terms in this series are not necessary to get a good estimate of the change in hydraulic head as a function of depth and time. A value of particular interest is the time constant associated with the first term in the series; $\tau_{(m=0)} = \tau_0$. τ_0 is the deformation time constant and represents the time after which the hydraulic head in the layer is 93% equilibrated with the boundary conditions [*Scott*, 1963; *Riley*, 1969].

Given this solution of the flow equation the link can be made between the change in hydraulic head and the change in aquifer thickness. In a confined aquifer system water is derived both from reduction of pore space (α) and expansion of the pore water (β).

$$\begin{aligned} S_s &= S_{sk} + S_{sw} \\ S_{sk} &= \rho g \alpha \\ S_{sw} &= \rho g n \beta \end{aligned} \qquad (2.19)$$

where S_{sk} is the skeletal specific storage and S_{sw} is the specific storage of water. S_{sk} is responsible for most of the water production as it is generally two to three orders of magnitude larger than S_{sw} (water is essentially an incompressible fluid).

We now show the derivation of the analytical solution for the equivalent change in aquifer thickness caused by a symmetric decrease in hydraulic head. The definition of α according to *Fetter* (2001) is:

$$\alpha = \frac{-(\Delta V_t)/V_{t0}}{\Delta\sigma'} \tag{2.20}$$

where ΔV_t is the change in total volume (thickness) and V_{t0} is the original total volume. Looking at only the vertical displacements:

$$\alpha_z = \frac{-\Delta b/b_0}{\Delta\sigma'_z} \tag{2.21}$$

where Δb is the change in thickness of a given volume and α_z is the rock matrix compressibility in the vertical direction. Substituting the change in effective stress in the vertical direction, $\Delta\sigma'_z$ from equation 2.13 into equation 2.19 gives:

$$\alpha_z = \frac{-\Delta b/b_0}{-\rho g \Delta h}. \tag{2.22}$$

We rearrange equation 2.22 and substitute the relation for S_{sk} from equation 2.19 to get

$$\rho g \alpha_z b_0 = \frac{\Delta b}{\Delta h}$$

$$S_{sk} b_0 = \frac{\Delta b}{\Delta h}$$

$$S_k = \frac{\Delta b}{\Delta h} \quad . \tag{2.23}$$

The skeletal storage coefficient is a new parameter equal to the product of the compressibility of the aquifer system and the initial thickness of the aquifer system, $S_k = S_{sk} b_0$. Defining things in this way shows that, for a given aquifer system, there is a linear relationship between the change in thickness and the change in stress of a given unit that is governed by the skeletal storage coefficient.

We next substitute Δh from equation 2.18 into equation 2.23 and calculate the integral over the total height of the aquifer system. The thickness changes as a function of time as follows

$$b(t) = \int_{-b_0/2}^{b_0/2} S_{sk} \Delta h(t,z) dz = S_{sk} b_0 \Delta h (1 - \frac{8}{\pi^2} \sum_{k=0}^{\infty} \frac{e^{-\frac{\pi^2}{4}\frac{t}{\tau_k}}}{(2k+1)^2}) \ . \qquad (2.24)$$

This equation is not entirely applicable to real aquifer systems as time variant boundary conditions complicate this simple solution. However, it is possible now to identify the approximately linear relationship between hydraulic head and aquifer system compaction.

Up until now the discussion has involved lumped aquifer and aquitard properties for any aquifer system. However, the two types of hydrogeologic units, aquifers and aquitards, deform in one of two ways: ‘elastically’ or ‘inelastically’, depending on the stress history and the current state of stress. *Poland et al.* (1975) describe the difference between elastic and inelastic deformation as follows. Aquifers deform primarily elastically at the depths of typical groundwater production. However, aquitards require two skeletal storage terms

$$S_{sk} = \begin{cases} S_{ske} \rightarrow \sigma'_z < \sigma'_{z(max)} \\ S_{skv} \rightarrow \sigma'_z \geq \sigma'_{z(max)} \end{cases} . \qquad (2.25)$$

If the effective stress is less than any previously experienced effective stress, known as the maximum effective stress ($\sigma'_{z(\max)}$), then the aquitards will deform elastically and all deformation is recoverable. However, if $\sigma'_{z(\max)}$ is exceeded the aquitards will begin to deform inelastically and there will be permanent non-recoverable deformation. Often $\sigma'_{z(\max)}$ is referred to as a minimum preconsolidation head (h_{pc}). In many cases linearizing equation 2.24 can approximate elastic deformation

$$\frac{\Delta b}{\Delta h} = S_{ke} \text{ for } h > h_{pc} . \qquad (2.26)$$

Lab tests have shown that the relation for inelastic deformation in fine-grained sediments is approximately logarithmic [*Jorgensen*, 1980]. If, however, the changes in effective stress are small, Δh less than 100 m, then a linear equation arises as well [*Leake and Prudic*, 1991]:

$$\frac{\Delta b}{\Delta h} = S_{kv} \text{ for } h < h_{pc} . \qquad (2.27)$$

It is important to remember that in equations 2.26 and 2.27 we assume that the head throughout the layer has equilibrated with the hydraulic head at the boundaries. The time scale for this realization is τ_0 which, from equation 2.18, is proportional to the skeletal storage term. Because values of S_{kv} are generally ten to one hundred times larger than

values of S_{ke}, the time constant for elastic deformation is on the order of days while the time constant for inelastic deformation can be on the order of years or decades [*Ireland et al.*, 1984; *Riley*, 1998]. For a typical aggregate thickness of an aquifer system, S_{kv} of the aquitards is so large that it can be assumed to represent the inelastic storage coefficient for the entire aquifer system [*Poland et al.*, 1975].

The analytical solution for the 1-D diffusion equation discussed above shows that there is a time scale for equilibrating the hydraulic head throughout a layered aquifer system. This time scale will vary based on stress conditions and aquifer material properties. In the next section we will discuss how this theory may be applied to a complex aquifer system like the SLV.

2.2.2 Coupled hydromechanical systems

The assumptions made during the analytical formulation of equation 2.26 may not be valid for the hydro-mechanical model that has been created for the SLV. In general it is not true that a symmetric change in head occurs at each boundary of the aquifer system (see assumptions for solution of equation 2.17). Figure 2.7 is a simple sketch of the movement of water in a valley type confined aquifer system. The confined aquifer system is kept under pressure by an aquitard or confining layer, and recharged from the edges of the valley floor by water runoff. This stored water is then extracted from irrigation wells

in the central area of the valley. In the 1-D diffusion equation the hydraulic head gradient given accounts only for flow in the vertical direction and is not able to account for the horizontal flow through the system that may also cause a deformation of the ground surface.

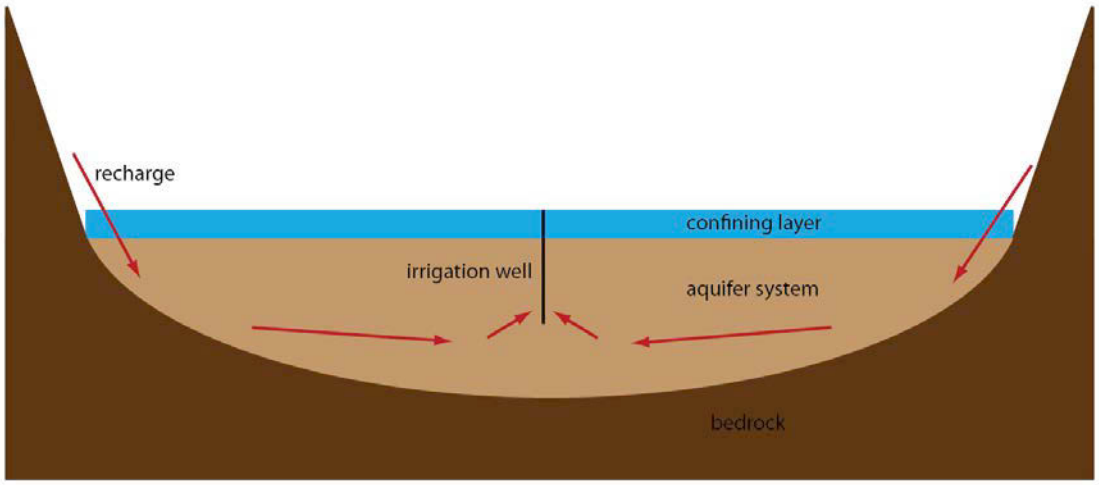

Figure 2.7: The typical movement of water in a valley type aquifer system.

The area between the confining layer and the aquifer system in Figure 2.7 is enlarged in Figure 2.8. By visualizing this conceptual system we can better understand the hydro-mechanical response to different boundary conditions, stress histories and layer properties. Figure 2.8 is a sketch of the flow of water when pumping first starts in the center of the valley. The pumping creates an area of low hydraulic head while the recharge from the valley walls creates an area of high hydraulic head. If the hydraulic head in the confining layer is equal to the hydraulic head in the aquifer system then water will flow horizontally through each layer to the wells. In this scenario if the recharge from the valley walls does not replenish the water removed through the wells, elastic

deformation of both the confining layer and the aquifer system will occur. If the hydraulic head in the confining layer drops below the preconsolidation head then that part of the system may deform inelastically.

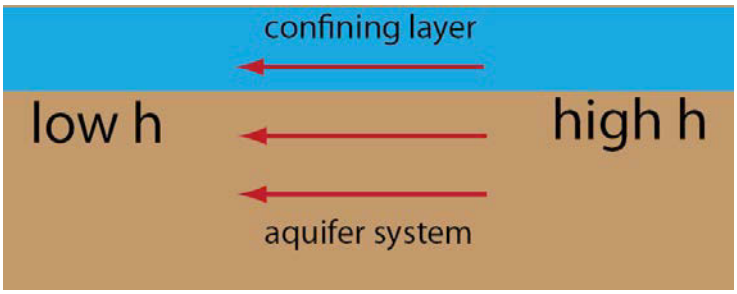

Figure 2.8: When the hydraulic head in the confining layer is equal to the hydraulic head in the aquifer system then water will flow horizontally through each layer from the valley rim to the wells.

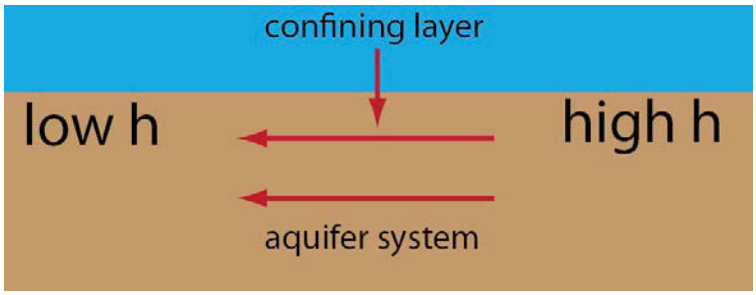

Figure 2.9: When the hydraulic head in the confining layer is greater than the hydraulic head in the aquifer system and water will begin to flow from the confining layer to the aquifer system.

Figure 2.9 shows another scenario where the aquifer system material is much more conductive than the confining layer. In this case, water is mainly being extracted from the aquifer system and the hydraulic head in that layer drops. Over some time the hydraulic

head in the confining layer becomes greater than the hydraulic head in the aquifer system and water will begin to flow from the confining layer to the aquifer system. The rate at which this process occurs depends upon the vertical hydraulic conductivity of the confining layer and the thickness of this confining layer. If the hydraulic head in the confining layer drops below the preconsolidation head then that layer will begin to deform inelastically. This deformation is in addition to any elastic deformation that may also be occurring in the aquifer system due to the decrease in hydraulic head in that layer.

As is shown in the scenarios above deformation that is measured at the surface by InSAR is a result of a number of different mechanisms other than what was expressed in the 1-D diffusion equation. For this reason, more complicated methods, such as finite difference modeling, have been used to represent the hydrogeologic system. In the chapter to follow we will outline all of the hydrogeologic, hydraulic head and Synthetic Aperture Radar (SAR) data collected in the SLV.

Chapter 3
Overview of available data

There are two main goals for this chapter: 1) to introduce the field site, 2) to outline all of the available data in the San Luis Valley (SLV). We will first discuss the geographic regions of the SLV, which will become pertinent when we introduce the complex hydrogeology. We will summarize the work of the Rio Grande Decision Support System (RGDSS) to build hydrogeologic layer maps and parameter zones for aquifer properties. Then we will introduce the Synthetic Aperture Radar (SAR) and hydraulic head data.

3.1 Introduction to the field site

The San Luis Valley (SLV) is a rift valley in south-central Colorado bounded by igneous, metamorphic, and sedimentary bedrock of the Sangre de Cristo and San Juan mountain ranges. The basin has a graben structure, known as the Baca graben, and contains valley fill that consists of interbedded deposits of sand, clay, gravel, and some

layers of volcanic rocks [*Hearne and Dewey*, 1988]. The boundary of the SLV is defined by the extent of the sediments that fill the San Luis Basin which extends down into New Mexico [*Emery et al.*, 1973].

The geology of the SLV is complex, and most of the hydrogeologically important layers do not extend across the entirety of the Valley. Thus, to understand the SLV's geologic structures and their hydrologic functioning, the RGDSS documentation describes this layering by reference to distinct geographic regions of the Valley as well as vertical hydrogeologic layers. Geographic regions of the San Luis Valley that are pertinent to the hydrogeology are shown in Figure 3.1 (outlines shown in white) and are as follows:

Closed Basin: The portion of the Valley that lies north of both the Rio Grande River and Costilla County. This is the part of the Rio Grande Basin in Colorado where the streams drain to the San Luis Lakes (the southeastern Closed Basin) and adjacent territory, and do not normally contribute to the flow of the Rio Grande.

San Luis Hills: A prominent series of mesas and eroded hills in the southern Valley. The Rio Conejos flows along the western side of the San Luis Hills. The Rio Grande cuts through the San Luis Hills downstream of its confluence with the Rio Conejos.

Conejos and Alamosa River Valleys: The southwestern portion of the Valley, south of the Rio Grande and north and west of the San Luis Hills.

Costilla County: The southeastern portion of the valley contains the Trinchera Creek valley, the Costilla Plain, the foothills of the Culebra Range, and San Pedro Mesa.

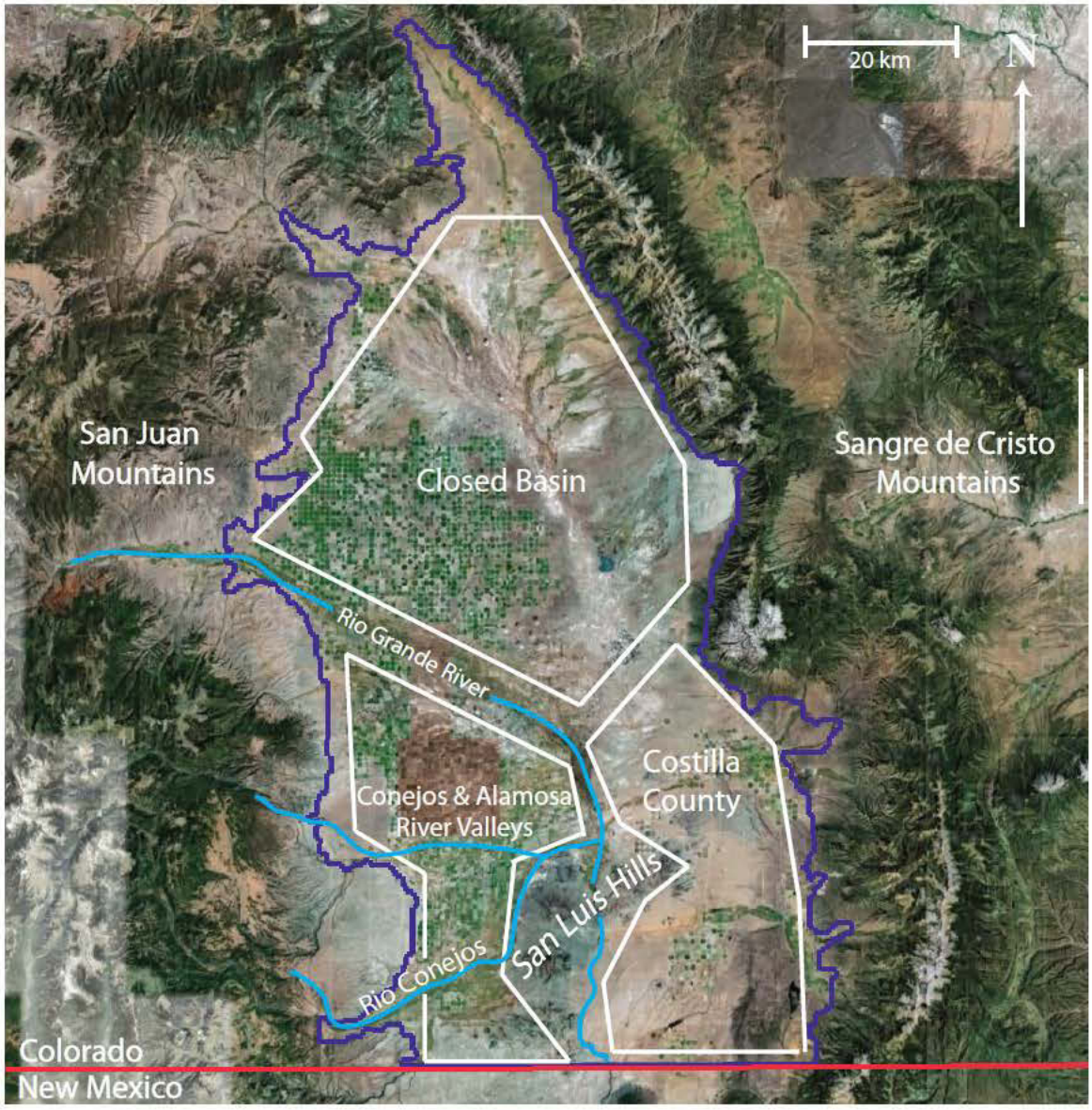

Figure 3.1. Geographic boundaries (defined by white lines) and the outline of the San Luis Valley (defined by the purple line). The red line is the state boundary between Colorado and New Mexico.

3.2 Hydrogeologic data

There are two aquifers in the SLV, the unconfined aquifer and the confined aquifer system. These two aquifers are separated by a confining layer known as an aquitard. Figure 3.2 is a schematic cross section of how the geology varies from north to south in the SLV. In this section we discuss the data used by the RGDSS to create the hydrogeologic layer maps, give lithologic descriptions of the hydrogeologic layers and then show how measured aquifer parameters were assigned to the different hydrogeologic layers.

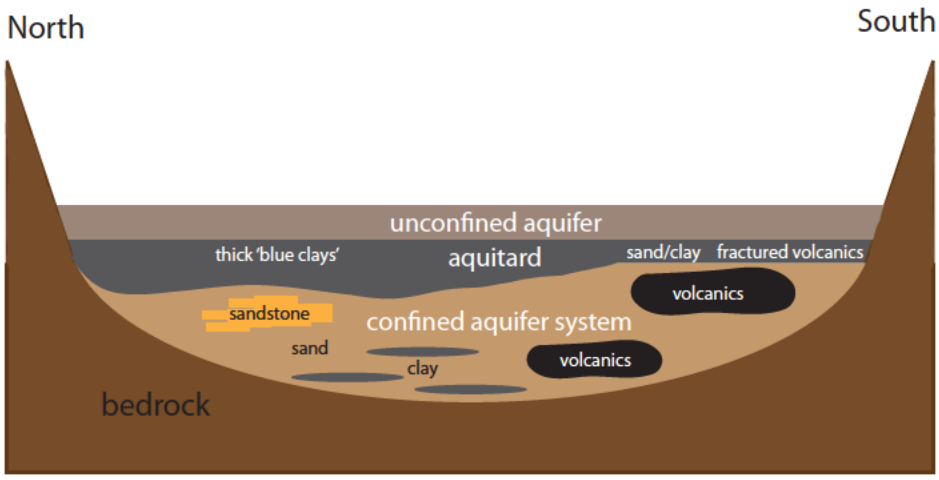

Figure 3.2: A schematic showing the variable geology of the hydrogeologic layers from north to south in the San Luis Valley.

3.2.1 Hydrogeologic layers

The RGDSS set up the conceptual hydrogeologic model with five distinct hydrogeologic layers: the unconfined aquifer (layer 1), the aquitard (layer 2), and the

confined aquifer system (layers 3 – 5). They determined the relative thickness of the layers by creating a database of driller's logs. The lithologic data came from three sources: the RGDSS piezometer logs, the State Engineer's Office (SOE) reports and various geophysical logs. The Department of Defense Groundwater Modeling System (GMS) was used to interpolate between the various lithologic data using a kriging method.

Three cross sections of the hydrogeologic layers are given in Figure 3.3. We can see that the thickness of the layers varies significantly from north to south in the valley. It is important to note that the lithology of these layers also varies from north to south. Below we provide a generalized geologic description of the layers (beginning with the top layer):

Layer 1: **Unconfined aquifer** – This layer contains mainly sand, gravel, and cobbles, with minor thin (<10 ft.) clay units. The layer thickness ranges from 15 to 150 m.

Layer 2: **Aquitard** – This layer contains lacustrine sediments, clay dominated with generally less than 25% sand or gravel content. It is known as the 'blue clay' layer in some areas of the valley and in other areas it appears as unfractured volcanic rocks [*Emery et al.*, 1973; *Hearne and Dewey*, 1988]. Considered as a whole this layer acts as an aquitard to confine deeper layers. However, the sand layers within this clay-dominated series do still constitute an aquifer in

some parts of the SLV. This layer is over 120 m thick in the center of the Closed Basin and 1 m thick near the edges of the valley (see cross section B – B' in Figure 3.3). In Costilla County this layer does not exist, rather a series of discontinuous clay and sand layers act as the aquitard (see cross section C – C' in Figure 3.3).

Layer 3: **Confined aquifer system** – In the northern portion of the SLV this layer contains mainly sand, although clay layers do still appear. Sand or sandstone layers make up at least 50% of the interval (see Figure 3.2). This is generally interpreted to be the most productive portion of the confined aquifer system. In the southern portion of the SLV layer 3 is composed of the Hinsdale and Servilleta Basalts (see Figure 3.2). In the Conejos and Alamosa River valleys it is interbedded with the Hinsdale Formation basalt lava flows. In Costilla County this layer contains the Servilleta Formation, consisting primarily of basalt lava flows located south of the San Luis Hills. These lava-flow layers vary from thin and highly fractured to very thick and unfractured. The thick and unfractured lava flows form a confining layer or aquitard. In some areas the permeability is very high, and hence this layer is considered a productive portion of the confined aquifer system.

Layer 4: **Confined aquifer system** – This layer is predominantly sand and gravel with up to 50% clay in most areas of the SLV. In Costilla County, this layer also contains volcanic/volcaniclastic rocks. Evidence indicates that in some

locations this formation consists of poorly cemented sandstone and conglomerate interbedded with up to 50% clay.

Layer 5: **Confined aquifer system** – This layer is more clay rich than layer 4, generally of low hydraulic conductivity. This layer only occurs in the Baca graben area, the most central part of the valley (see cross section B – B' in Figure 3.3). Due to its depth and low hydraulic conductivity it is not generally considered a productive aquifer.

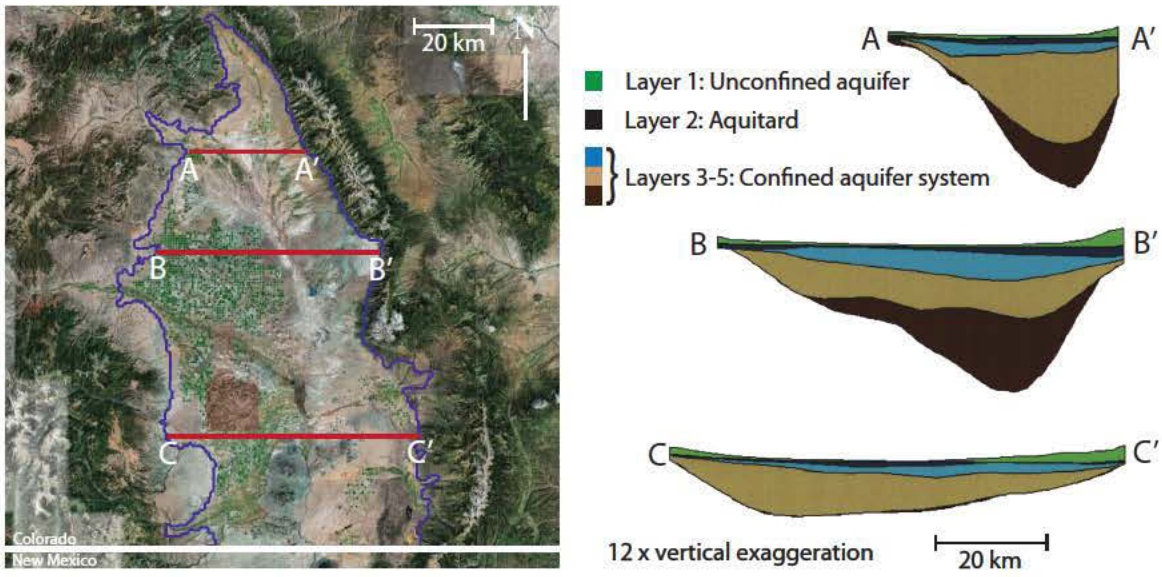

Figure 3.3. Cross-sections of the hydrogeologic layers across the SLV [*HRS Water Consultants Inc.*, 2002]

The available geologic and geophysical evidence shows that the hydrogeologic layers of the confined aquifer system are hydraulically connected to each other and in some locations to the unconfined aquifer. Next we will review how aquifer parameters,

collected by performing aquifer tests, were assigned to the different hydrogeologic layers.

3.2.2 Aquifer parameters

There were 148 and 151 aquifer tests for the unconfined aquifer and the confined aquifer system respectively. Estimates of aquifer parameters were made by performing aquifer tests and using traditional curve-matching methods of data analysis *[Harmon, 2001].* These parameters were then assigned to the hydrogeologic layers described in the previous section. Because the hydrogeology in the SLV is so variable from north to south and east to west, HRS Water Consultants created parameter zones that honor these changes in the horizontal plane. The estimates of aquifer parameters were then parsed directly into these different zones.

An aquifer test involves pumping water out of the aquifer system at a pumping well and inducing a drawdown of the hydraulic head at monitoring wells some distance away. The well that the water is pumped from is referred to as the aquifer test well. Once pumping is finished the hydraulic head levels rebound. During this rebound the hydraulic head change through time is measured at the aquifer test well. This measurement is compared to an analytical solution of the hydraulic head change (e.g. Theis equation or Hantush-Jacob formula). The transmissivity (T) and the storage coefficient (S) are the estimated aquifer parameters that allow the analytical solution to match the measurements. For an accurate measure of S at least one other well must be monitored other than the aquifer test well.

The estimated aquifer test parameters were assigned to the hydrogeologic layers based on the interval of the aquifer system screened at the aquifer test well. Once all the aquifer parameters were assigned to a hydrogeologic layer they were distributed the horizontal place by interpolating, through kriging, the estimated parameters within a parameter zone. The combined use of kriging with parameter zones ensures the exact value of the aquifer parameter is honored at the measurement location, while maintaining the general distribution of geologic materials.

3.3 Hydraulic head

Hydraulic head measurements in the SLV are either made in open wells or using piezometers. For most open wells the well casing is effectively attached to the aquifer material for the entire screened interval. The casing has a part that extends beyond the height of the ground surface, this is known as the 'stickup'. The depth to water (DTW) is measured from the stickup to the water level in the well. That value is then referenced to the height of the ground surface, which has been surveyed or taken from a topographic map. If the height of the ground surface is taken from a topographic map then it is generally known to within a foot.

Each RGDSS piezometer has a 4-inch diameter screened interval where gravel was packed in the annulus between screen and borehole. The intervening 4-inch diameter casing intervals were filled with Portland cement. Above the uppermost screened interval the annulus between casing and borehole was filled with Portland cement. The casing and screen are locked into place along the entire length of the piezometer by the friction

between borehole and gravel pack (or Portland cement), and by the friction between casing/screen and cement or gravel pack. It is expected that the casing expands and contracts synchronously with the compression and rarefaction of the aquifer/aquitard. The hydraulic heads at the piezometer locations are also measured against a stickup and referenced to the height of the ground surface.

The RGDSS database contains information about the well network with tables that are linked to the location, position of the screened interval and the ground level elevation of each well. There are over 1200 wells in the SLV, but at only 328 wells are there hydraulic head measurements in the confined aquifer system. In the chapter to follow we will review the hydraulic head data to determine which of the 328 wells can be used in conjunction with the InSAR deformation data.

3.4 Synthetic Aperture Radar (SAR) data

SAR data for the SLV were acquired from two sources: the Western North American Interferometric Synthetic Aperture Radar Consortium (WInSAR) and the European Space Agency (ESA). In this study data from the ERS-1 and ERS-2 satellites were used, covering the period from 1992 to 2000. Figure 3.4 shows the RGDSS model boundary and the spatial extent of available scenes. Table 3.1 shows the number of scenes that were acquired over the SLV.

This study focused on track 98 and frame 2853, which has 50 scenes with good spatial coverage of the valley. Scenes from 2001-2005 could not be used because of problems

with the satellite's navigational system. For this study we focused on scenes from 1992 – 2000 (31 scenes), which would be able to provide valuable information for the Confined Aquifer Rules decision of 2006 (see Chapter 1). In section 2.1.1 we discussed that the average sampling of ERS SAR data is on the order of once every 35 days. However, because we are working with historic data the satellite was not necessarily acquiring data each time it revisited the area over the SLV. Therefore our dataset has fairly irregular sampling, approximately one acquisition every 3 months.

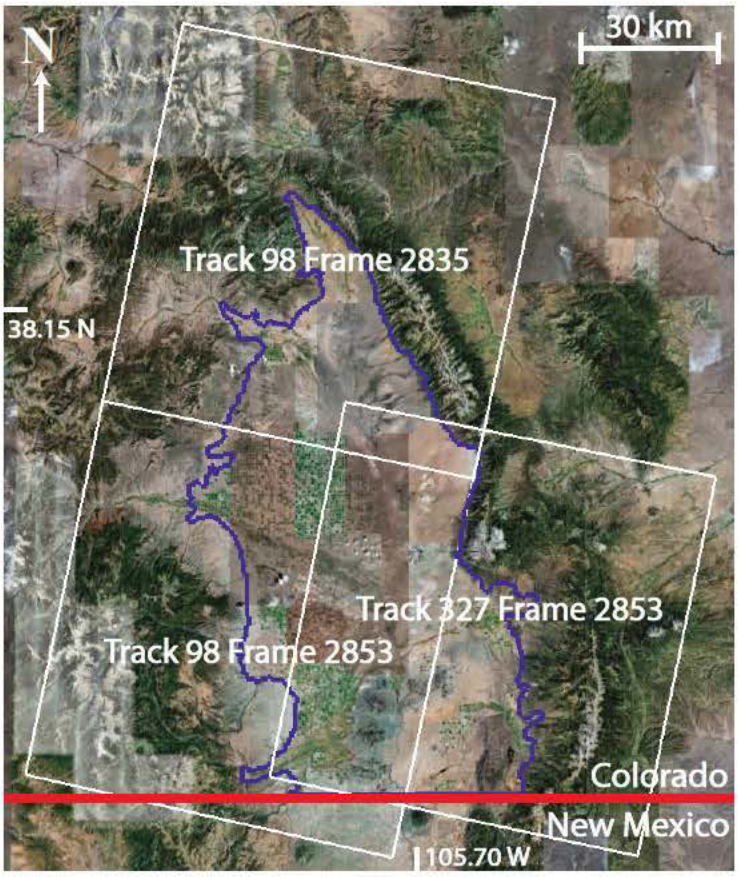

Figure 3.4: The RGDSS model boundary (purple), available InSAR data (white), and the state line between Colorado and New Mexico (red) (source of background image: Google Earth map with European Space Agency track and frame overlays).

Table 3.1: SAR acquisitions over the SLV, see Figure 4.1 for the location of each frame.

Track	Frame	# Scenes	Start	End
98	2853	50	1992	2011
98	2835	50	1992	2011
327	2853	23	1995	1999

Chapter 4
Assessment of hydraulic head data

In this chapter we will first investigate the spatial and temporal sampling of the hydraulic head data at wells in the confined aquifer system (see section 4.1). Next we need to ensure that the amount of deformation caused by changes in hydraulic head in the San Luis Valley can accurately be measured using InSAR. We calculate the average seasonal hydraulic head change at each well location and use estimates of S_{ke} to predict the amount of deformation we expect to see at the surface (see section 4.2).

4.1 Review of hydraulic head data

Of the 328 wells sampling the confined aquifer system only 69 wells had hydraulic head measurements from 1992 – 2000 (time span of InSAR data) and were located within the SAR scene (track 98 frame 2853 introduced section 3.4). An initial assessment of the data found that 19 wells had ≤ 2 hydraulic head measurements from 1992 – 2000. Because of the low temporal sampling at these 19 well locations the

hydraulic head data were not used for further analysis. In the sections to follow we discuss the spatial and temporal sampling of the hydraulic head data at the remaining 50 wells.

4.1.1 Spatial sampling of hydraulic head data

The locations of the 50 wells are shown as filled circles in Figure 4.1, with the outline of track 98 frame 2853 shown as a blue box. The size/color of the circle signifies the number of hydraulic head measurements made at that location. A majority of the wells (33) are located within the Closed Basin area of the SLV (northeast corner of the Figure 4.1).

An important piece of information about the hydraulic head data that is relevant for our study is that the wells are monitoring specific intervals of the groundwater system, while the deformation measured by InSAR is for the entire system. Therefore, an important step in any analysis of InSAR deformation and hydraulic head should be to determine the hydrogeologic interval the wells are monitoring. In the SLV information on well construction, which would provide the depth and extent of the screened interval, was not collected for all wells. Most of the wells in the SLV were initially drilled to extract water at a high flow rate. It is common that once the drillers encounter a high flowing interval drilling is stopped [*Willem Schreuder personal communication,* 2011]. Consequently, we assume that the lowest unit in the well is the interval of the aquifer being monitored.

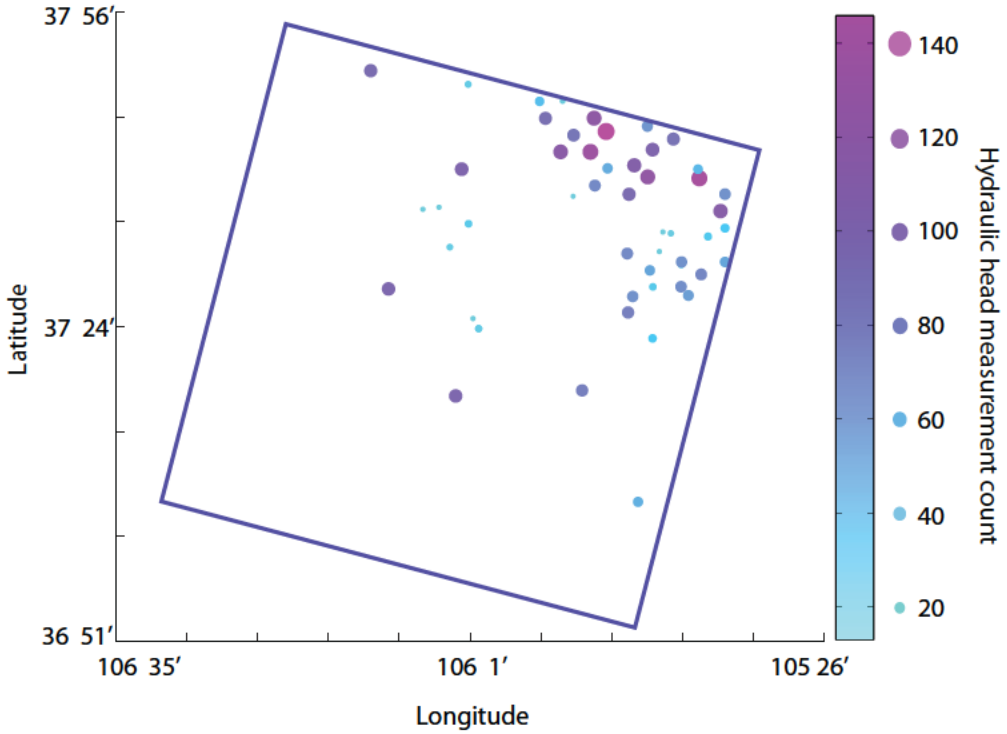

Figure 4.1: Locations of wells in the San Luis Valley are shown as filled circles. The size/color of the circle signifies the number of measurements made at that location from 1992 - 2000. The blue box shows the outline of the SAR data from track 98 frame 2853.

The locations of the wells are shown again in Figure 4.2, with the color scheme based on the interval of the aquifer system within which the wells are screened. As introduced in section 3.2 the wells have been assigned to the Rio Grande Decision Support System (RGDSS) hydrogeologic model layers. A majority of the wells are monitoring layer two (pink filled circles): 33 are within the Closed Basin, in the northeast corner of the image, one is in Costilla County and one is north of the Rio Grande River. Layer two, the Upper Alamosa or 'blue clay' layer, is clay dominated in most of the SLV (see section 3.2). In all areas but Costilla County this layer acts as the main aquitard for the underlying

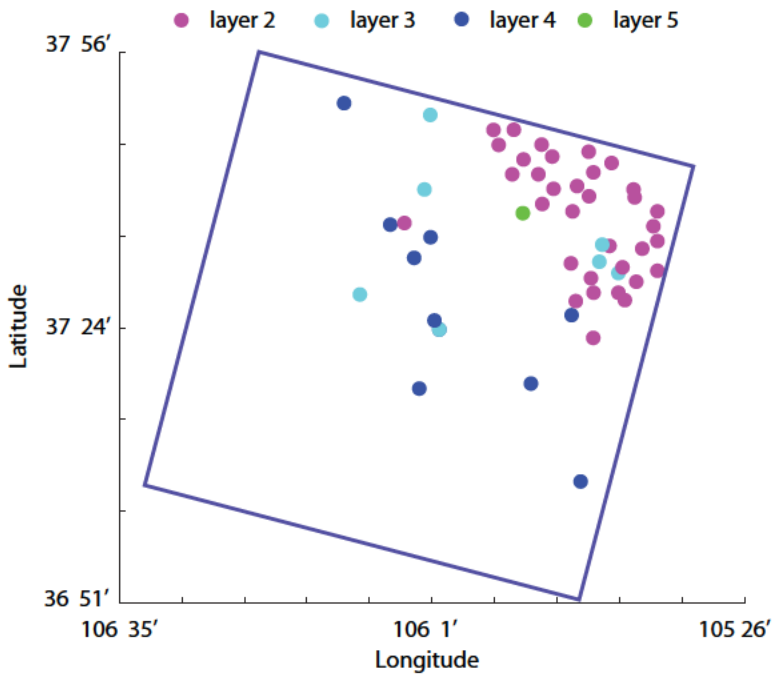

Figure 4.2: A plan view showing the location of the 50 monitoring wells where the hydraulic head change was measured from June 19, 2000 – July 24, 2000. The wells are colored based on the Rio Grande Decision Support System (RGDSS) model layer they are screened in. The blue box shows the outline of the SAR data from track 98 frame 2853.

confined aquifer system. The 33 wells monitoring layer 2 in the Closed Basin area are not monitoring hydraulic head in the confined aquifer system and are hence not relevant for this study. These wells were put in place by the United States Bureau of Reclamation (USBR) to monitor a reclamation project involving the unconfined aquifer in the Closed Basin. The two other wells monitoring layer 2 are RIO3 near Monte Vista (western side of the valley, north of the Rio Grande River) and NA03601112BAB in Costilla County (eastern side of the valley, north of the San Luis Hills). These two wells have also been

removed from the analysis to follow as they may be in areas where layer 2 is still the confining unit (see section 3.2 for more information on the continuity of the confining unit in the SLV). The remaining 15 wells were used for further analysis in this chapter.

4.1.2 Temporal sampling of hydraulic head data

The confined aquifer monitoring wells in the SLV are sampled at variable rates ranging from once per month to once per year. In order to compare these hydraulic head data with the irregularly sampled SAR dataset in the SLV the hydraulic head data were interpolated in time. A review of the 15 hydraulic head time-series showed large changes in hydraulic head over very short time periods at 10 out of 15 well locations. For example, the measurements made at well EW71C are shown in Figure 4.3. In red is the interpolation of the measurements. At certain time periods the hydraulic head measured changes drastically: June 1993, November 1993, April 1996, December 1996, November 1997, January 1997, December 1999, February 2000, June 2000 (shown with arrows in Figure 4.3). These measurements may be due to: a) sudden changes in hydraulic head when a nearby well is being used for groundwater extraction or b) errors with the measurement device. In practice hydrologists attempt to make measurements of the hydraulic head that are indicative of stable conditions [*Willem Schreuder personal communication,* 2012]. However, if a well nearby to the monitoring well is extracting water during the time of the measurement the hydraulic head at the monitoring well will not depict the stable condition of the aquifer system. At most pumped wells in the SLV hydraulic head levels rebound to stable conditions within 2 to 3 hours from the cessation of pumping [*Eric Harmon personal communication,* 2013]. It is this stable hydraulic head

that the RGDSS model aims to model, and hence we must evaluate to what extent InSAR deformation data can inform these measurements.

To remove the effects of these rapid perturbations in the hydraulic head time-series (blue markers are highlighted with arrows in Figure 4.3) a moving window average was applied to the interpolated data. The window length of the temporal filter was varied until an optimal value was found. A window length of 90 days allowed for the mitigation of these rapid perturbations without removing the entirety of the seasonal groundwater signal (see the green dashed line in Figure 4.3). The same moving window average was applied to the hydraulic head data from all 15 wells.

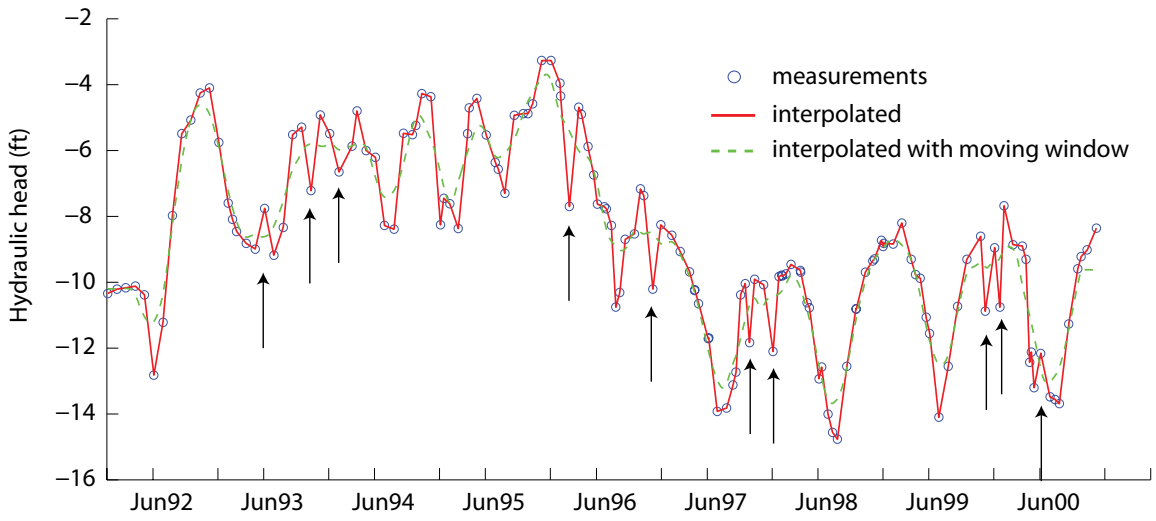

Figure 4.3: Hydraulic head measured at well EW71C shown with blue markers. The arrows signify hydraulic head measurements that may be affected by instrument errors or pumping at nearby wells.

4.2 Predicted deformation

The goal for this section is to predict the seasonal magnitude of the deformation that we expect to see at each of the remaining 15 well locations (shown in Figure 4.4). In order to do so we first assume that the deformation occurring in the SLV is elastic. This allows us to rearrange equation 2.26 as follows:

$$\Delta d = S_{ske} b^{*} \Delta h \tag{4.1}$$

where Δd is the predicted deformation at the surface, S_{ske} is the skeletal elastic storage coefficient, b^{*} is the thickness of the producing aquifer unit, and Δh is the change in hydraulic head. We can see that if the product of S_{ske}, b^{*} and Δh is small the deformation at the surface will not be large enough to be accurately measured using InSAR. For this analysis we will assume that the uncertainty in the InSAR measurement is approximately 5 mm [*Hoffman et al.,* 2002]. This means that predicted deformations of less that 1 cm will not be accurately determined by InSAR.

In order to simplify the analysis we created an aggregate variable, seasonal hydraulic head change (Δh_s), which is the average seasonal peak-to-trough change in hydraulic head. We used upper and lower bounds for S_{ske} from the literature (see Table 4.1). Where the producing lithology was not known we used the S_{ske} values for sand, as it is most likely that an aquifer is producing water from a sandy lithologic unit in the San Luis Valley. We note that there are cases for solid rock where S_{ske} can be less than 3.3E-6, but for the analysis given below we will only consider the fissured/jointed rock case. Most of

the well locations have some estimate of the producing thickness (b^*) from the RGDSS database and well driller's logs. However, it is important to note that the values estimated for b^* are highly subjective and it is possible that the producing thickness for a number of these wells is much less than the estimates we give in Table 4.2. With these three parameters (S_{ske}, b^* and Δh_s) we calculated a range for the magnitude of the seasonal deformation at each well location (see Table 4.2).

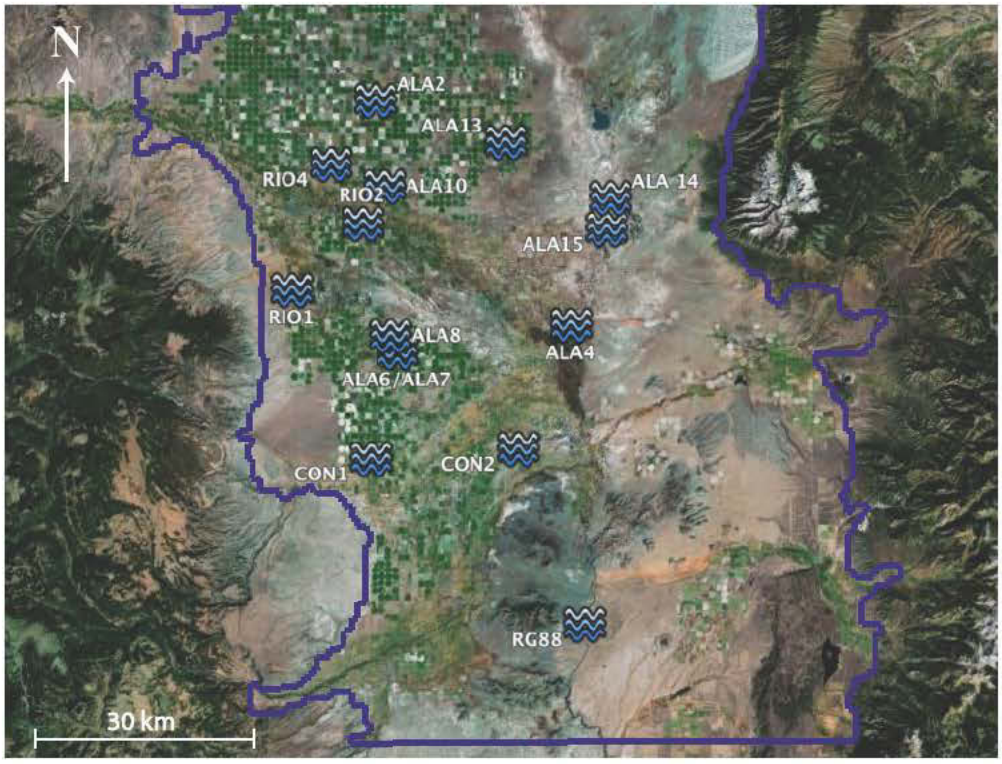

Figure 4.4: Location of the 15 wells where the predicted deformation was calculated. The purple outline is the Rio Grande Decision Support System (RGDSS) model boundary.

Table 4.1: Estimates of S_{ske} for different lithologies [*Batu*, 1998].

Lithology	***min Sske (m^{-1})***	***max Sske (m^{-1})***
Clay	*9.2 ×10-4*	*1.3 ×10-3*
Sand	*4.9 ×10-5*	*2.0 ×10-4*
Rock, fissured/jointed	*3.3 ×10-6*	*6.9 ×10-5*

We expect the deformation at eleven wells: ALA6, ALA7, ALA8, ALA13, CON1, ALA4, CON2, RIO2, RG88, ALA15 and ALA14 to be measureable by InSAR. We found that three well locations, ALA10, RIO4 and RIO1 had essentially zero seasonal hydraulic head change, therefore no deformation is predicted at those locations. The predicted deformation at well ALA2 was deemed too small to be accurately measured by InSAR. Because the lithology of the producing zone for ALA4 was more complicated than the other wells we assumed for the Δd_{min} calculation that the well was entirely producing from hard rock sediments and for the Δd_{max} calculation that the well was entirely producing from clay sediments. At wells CON1 and CON2 where basaltic rock is present we used the S_{ske} value for Rock, fissured/jointed from Table 4.1.

Based on the analysis presented in this chapter we will move forward in our study only considering the 11 wells where the predicted deformation is large enough to be accurately measured by InSAR. In the chapter to follow we will assess the quality of the InSAR data in agricultural areas of the SLV.

Table 4.2: Predicted max and min seasonal deformation for 15 well locations.

Well	***Producing lithology***	***S_{ske} range (m^{-1})***	***b^* (m)***	***Δh_s (m)***	***Δd range (cm)***
ALA6	Sand	$4.9\times10^{-5} - 2.0\times10^{-4}$	25	7.6	1 - 4
ALA7	Sand	$4.9\times10^{-5} - 2.0\times10^{-4}$	58	6.1	2 – 7
ALA8	Sand	$4.9\times10^{-5} - 2.0\times10^{-4}$	183	4.3	4 – 16
ALA13	Clay	$9.2\times10^{-4} - 1.3\times10^{-3}$	111	4.3	44 – 61
CON1	Basaltic rock	$3.3\times10^{-6} - 6.9\times10^{-5}$	127	3.0	0.1 – 3
ALA4	Hard rock/Clay	$3.3\times10^{-6} - 1.3\times10^{-3}$	302	3.0	0.3 – 100
CON2	Basaltic rock	$3.3\times10^{-6} - 6.9\times10^{-5}$	110	1.8	0.06 – 1
RIO2	Sand	$4.9\times10^{-5} - 2.0\times10^{-4}$	85	1.8	0.7 - 3
ALA2	unknown	$4.9\times10^{-5} - 2.0\times10^{-4}$	14	0.6	0.1 – 0.2
RIO1	Sand	$4.9\times10^{-5} - 2.0\times10^{-4}$	185	N/A	--
RG88	unknown	$4.9\times10^{-5} - 2.0\times10^{-4}$	186	< 0.5	1 – 2
ALA15	unknown	$4.9\times10^{-5} - 2.0\times10^{-4}$	132	< 0.5	0.8 – 1
ALA14	unknown	$4.9\times10^{-5} - 2.0\times10^{-4}$	96	< 0.5	0.6 - 1
ALA10	Sand	$4.9\times10^{-5} - 2.0\times10^{-4}$	335	N/A	--
RIO4	Sand	$4.9\times10^{-5} - 2.0\times10^{-4}$	183	N/A	--

Chapter 5
Assessment of InSAR deformation data

5.1 Introduction

The goal of this thesis is to use InSAR deformation data to estimate hydraulic head in the San Luis Valley (SLV), Colorado. The first step, and the focus of the present chapter, is to determine whether high quality InSAR data can be obtained in the SLV. The work completed in this chapter of the thesis was published in the journal Water Resource Research [*Reeves et al.,* 2011].

The SLV is an agricultural area, where crop growth, irrigation, land erosion, and harvesting cycles can all seriously degrade the InSAR data by perturbing the positions of individual radar scatterers. In contrast, the studies outlined below have been conducted in: a) urban areas or b) arid to semi-arid climate regions. In both urban areas and arid regions vegetation does not greatly interfere with the InSAR measurements.

A group of papers, beginning with the work done by *Galloway et al.* (1998), used InSAR data to identify where deformation due to groundwater extraction was occurring [*Galloway et al.*, 1998; *Amelung et al.*, 1999; *Hoffmann et al.*, 2001; *Bawden,* 2002*; Bell,* 2002*; Watson et al.*, 2002; *Hoffmann et al.*, 2003; *Schmidt and Burgmann*, 2003; *Canuti et al.*, 2006; *Chatterjee,* 2006*; Sneed et al.,* 2007*; Anderssohn et al.,* 2008*; Hung et al.,* 2010*; Wisely and Schmidt*, 2010; *Calderhead et al.,* 2011]. In many of these papers the authors attempted to understand the hydrogeologic structure of the subsurface from the InSAR deformation data. In most cases, in order to validate the data, the authors compared the InSAR deformation measurements to those made with Global Positioning Systems (GPS), leveling line surveys or extensometers.

However, in the SLV we do not have another surface deformation measurement to validate the InSAR data. This was also the case for two other studies, in the Arno River Basin, Italy by *Canuti et al.* (2006) and in the San Bernadino Basin, California by *Wisely and Schmidt* (2010). In both of these studies the authors compared the InSAR deformation measurements to seasonal trends in hydraulic head measurements for validation. We will validate the InSAR deformation data collected from the SLV by: evaluating the raw interferograms, quantifying the mean coherence of the deformation data and comparing InSAR derived hydraulic head estimates to hydraulic head measurements made in wells. We will use Small Baseline Subset (SBAS) analysis, as described in section 2.1.2, to process the InSAR data. First, the individual interferograms will be inspected for evidence of subsidence bowls due to seasonal grounwater pumping. Then, the mean coherence (a proxy for the quality of the data) will be calculated for all of

the pixels in the SLV. The final line of sight (LOS) deformation time-series will be compared to hydraulic head data at specific well locations. This comparison aims to identify similar seasonal trends in the two datasets. Finally, the work presented here will go a step farther than previous research, and attempt to predict hydraulic head from the InSAR deformation data at specific well locations using compressibility parameters derived from aquifer tests. In the short background section to follow we outline how deformation measurements and aquifer tests measurements can be used to predict hydraulic head.

5.2 Relating deformation to hydraulic head

The deformation of the ground surface, which is derived here from InSAR data, is directly related to changes in the thickness of the confined aquifer due to recharge and withdrawal of groundwater. We rearrange Equation 2.26 to show that the change in aquifer thickness Δb is governed by the change in hydraulic head Δh and the elastic skeletal storage coefficient S_{ke}, a parameter that characterizes the skeletal compressibility of the aquifer system [*Riley*, 1969]:

$$\Delta b = S_{ke} \Delta h \,. \tag{5.1}$$

This relationship is valid when the aquifer system is deforming elastically/recoverably. In order for an aquifer system to be deforming elastically the effective stress must be less than the preconsolidation stress, or equivalently the hydraulic head must be above the minimum historical hydraulic head. We assume that Δb is equal to the deformation of the

ground surface as measured by InSAR, that Δh is the change in head measured in monitoring wells, and that S_{ke} is obtained from an aquifer test (as described in Section 3.2.2).

The storage coefficient, S, that is obtained from an aquifer test has two components:

$$S = S_{ke} + S_w, \tag{5.2}$$

the elastic skeletal storage (S_{ke}) and the component of storage due to the compaction of water (S_w). In general S_w is small compared to S_{ke}, so we are able to assume that $S_{ke} = S$, an assumption made throughout this study.

5.3 The Small Baseline Subset and interferograms

Given the challenges of working in an agricultural area discussed in section 2.1.3, we implemented a version of Small Baseline Subset (SBAS) analysis that is specific to groundwater applications. In some agricultural areas stable patches have been found around farmed fields yielding InSAR data with high coherence [*Meyer et al.*, 1996; *Massonnet and Feigl*, 1998]. However, previous to this work no one has used SBAS analysis to investigate a time-series of deformation from an agricultural area. In this study the initial processing of the SAR data, up to and including phase unwrapping, was computed using the Generic SAR (GSAR) software package developed by NORUT [*Larsen et al.*, 2005]. We used GSAR to create the spatial versus temporal baseline plot by iteratively selecting the optimal thresholds. The thresholds were initially set low in

order to maximize the coherence and slowly increased. Our overall aim was to keep as many interferograms as possible, as the most accurate solutions are produced when the subsets are well connected, i.e. many interferograms are connecting scenes. The final spatial and temporal baseline thresholds were set at 400 m and 4 years respectively, which produced a single small baseline subset of 96 interferograms (see Figure 5.1).

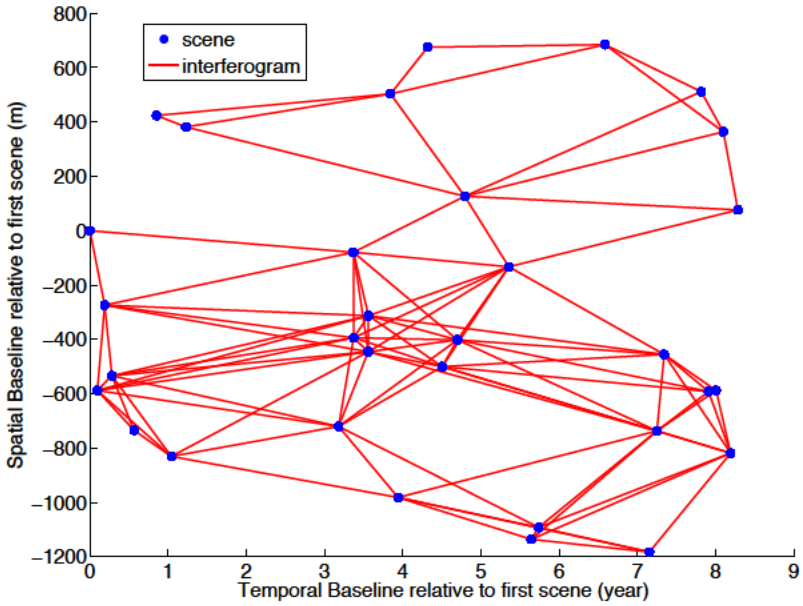

Figure 5.1: Spatial baseline vs. temporal baseline plot for the SLV data, track 98 frame 2853.

We inspected all interferograms as a preliminary review of the data. Our objective was to identify the regions in the SLV where the interferograms alone contained evidence of deformation potentially induced by groundwater pumping. An interferogram from November 1999 to July 2000 is shown in Figure 5.2, with a large phase signature in the southwest region of the SLV (enclosed by the red box). This pattern of concentric rings

of constant phase is indicative of a subsidence bowl. The pattern of change in phase is consistent with the shape of a cone of depression, the drawdown of the hydraulic head around a well during pumping. Upon further investigation we found that groundwater pumping from the confined aquifer system is relatively high in this area and the seasonal hydraulic head change is often more than 7 m. The same pattern of concentric rings was found in a number of the interferograms, and was most prominent in interferograms that spanned a pumping season.

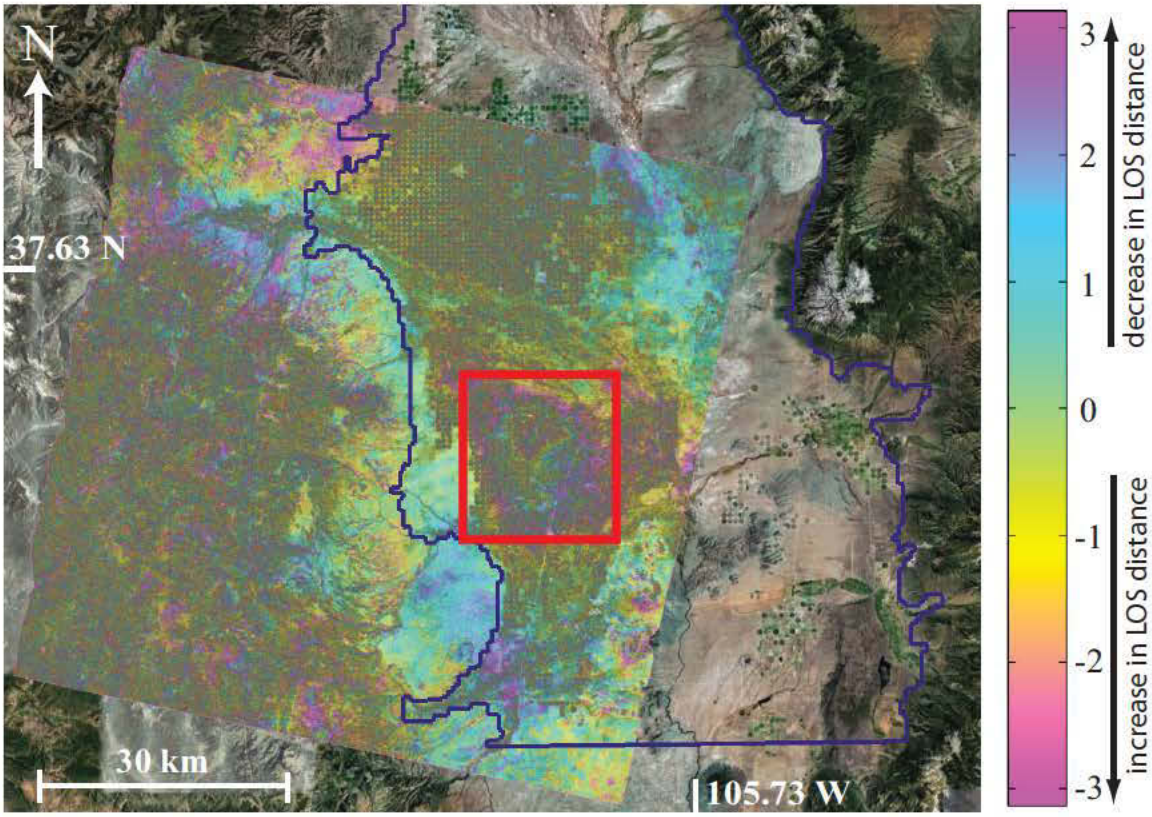

Figure 5.2: An interferogram from November 1999 to July 2000. The scale is in radians, where from magenta to magenta is 2π radians of phase change (source of background image: Google Earth map with Rio Grand Decision Support System (RGDSS) model boundary).

The investigation of this single interferogram provided some idea of the spatial extent of the seasonal deformation. However, an estimate of the quality of the data throughout time was still needed, i.e. the mean coherence from SBAS analysis. The mean coherence for all interferograms from 1992-2000 is discussed in the following section.

5.4 The mean coherence and SBAS thresholds

The mean coherence (γ_{mean}) for all pixels is shown in Figure 5.3. The average mean coherence value is 0.20, the maximum value is 0.92 and the minimum value is 0.10. The least coherent pixels ($\gamma_{mean} < 0.2$) fall outside the RGDSS model area in the mountainous region to the west of the SLV. The topography of this mountainous region affects the coherence if the spatial baseline is too large (i.e. the viewing angle of the two orbits is very disparate). The mountainous region also has vegetation and a seasonal snow pack that would cause significant amounts of temporal decorrelation. The maximum mean coherence values ($\gamma_{mean} \geq 0.7$) correspond to areas of ground that have large structures on them. These structures produce coherent signals because they do not change over time.

What is most striking about the image shown in Figure 5.3 is the very regular pattern of the coherent pixels. This regular pattern can be easily seen in Figure 5.4 a), an enlargement of the area inside the red box in Figure 5.3. The coherent pixels fall on a square grid, with spacing on the order of 800 m. The regions with coherent InSAR data are the interstices between the areas irrigated with the center pivot irrigation systems.

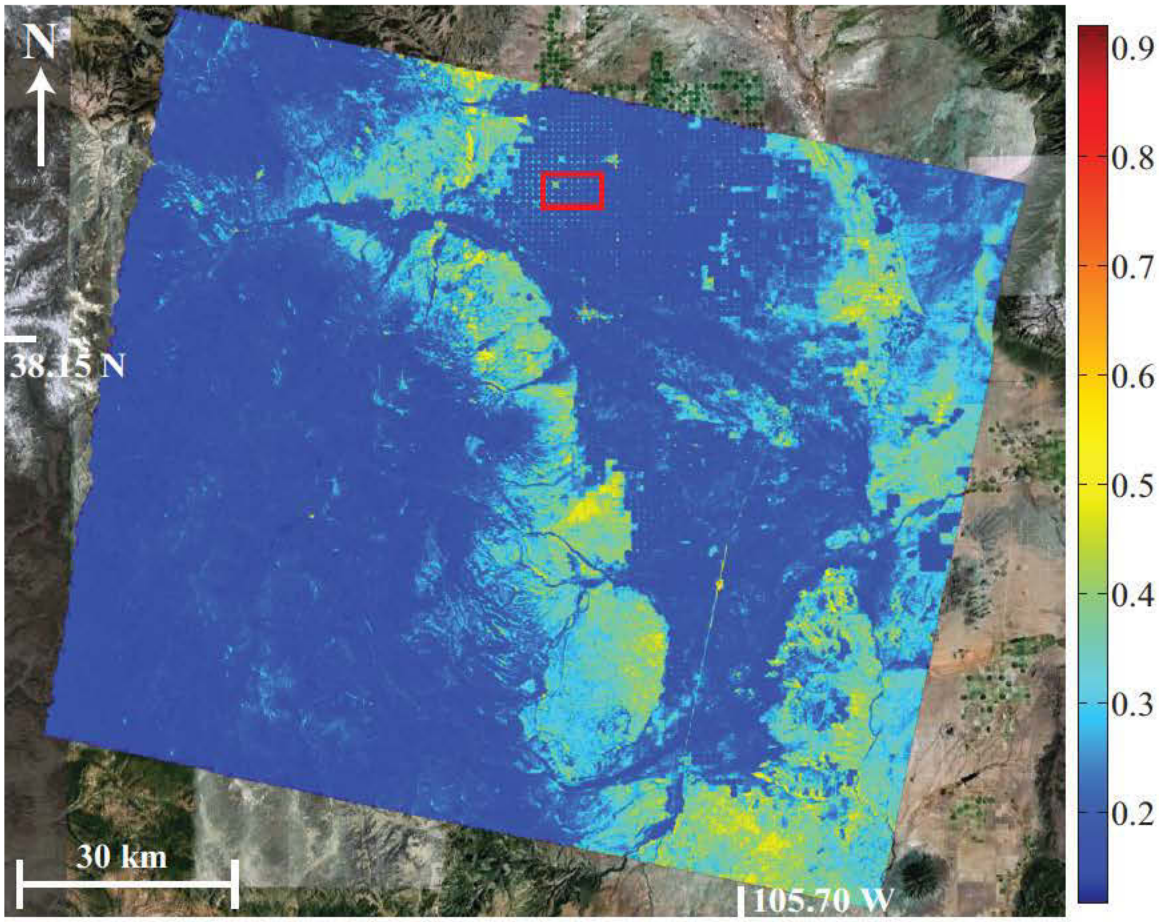

Figure 5.3: An image of the mean coherence (γ_{mean}), where each pixel corresponds to a 50 m by 50 m area on the ground. The area inside of the red box is enlarged in Figure 5.4 a) and 5.4 b) (source of background image: Google Earth map with Rio Grand Decision Support System (RGDSS) model boundary).

Figure 5.4 b) is a dimmed overlay of the mean coherence image on a map of the area. Figure 5.4 c) shows the center pivot irrigation system and the circular patterns with interstices. The presence of these areas between the center-pivot fields provides the spatial coverage needed to characterize deformation in the SLV. Without these interstices between the center-pivot fields, decorrelation throughout the

region would prevent any useful deformation measurements. *Massonnet and Feigl* (1998) saw a similar pattern in a single interferogram. The final step before the inversion, pixel selection, was implemented as described in section 2.1.3. After pixel selection we computed the Singular Value Decomposition (SVD) least squares (LS) solution. This provided a time series of the line-of-sight (LOS) deformation for each selected pixel in the SLV.

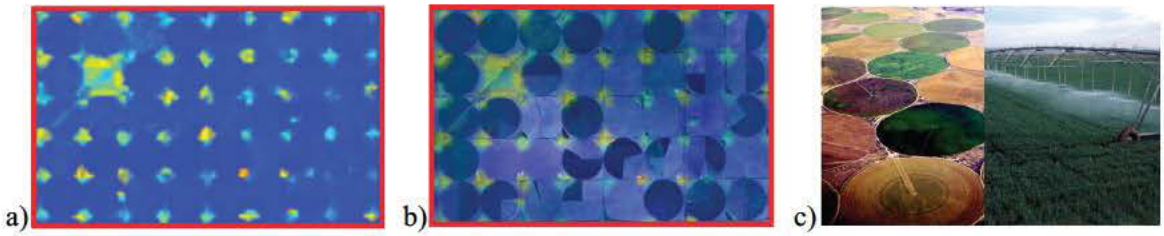

Figure 5.4: a) A close-up view of the mean coherence. b) The mean coherence overlaid on a Google Earth map. The higher coherence areas show up within the interstices between the center-pivot-irrigated areas. c) Photos of the SLV center-pivot-irrigation fields and watering system (source: thefullwiki.org and agmachine.ning.com).

After the mean coherence was calculated we applied a threshold that only allowed highly coherent pixels to be used in the remainder of the analysis. A pixel was selected if $\gamma > 0.26$ in at least 50% of the interferograms. The values for the threshold discussed in section 2.1.3 were found to be too admissive for the SLV. Initially the threshold was set as done previously by *Berardino et al.* (2002), i.e. $\gamma > 0.25$ in at least 30% of the interferograms. Then γ and the percentage of the interferograms required were iteratively increased and fewer pixels were selected. The goal of this procedure was to reach a

threshold that would require high coherence while still selecting pixels across the entire SLV. The next section we describe how we modified conventional SBAS analysis for groundwater applications in the SLV.

5.5 SBAS analysis modified for groundwater applications

Conventional SBAS analysis was discussed in section 2.1.3. As described in *Berardino et al.* (2002) conventional SBAS analysis requires some prior information about the deformation (low-pass deformation model), and that this deformation can be expressed as a simple linear, quadratic or sinusoidal function. Some previous work applying InSAR data to groundwater studies has used a sinusoidal function to capture the seasonal deformation signal [*Schmidt and Burgmann*, 2003; *Bell et al.*, 2008; *Wisely and Schmidt*, 2010]. This prior information can be provided by GPS measurements, leveling line surveys or extensometer measurements. These measurements are not available in the SLV during the time of InSAR data acquisition, so a reliable low-pass model does not exist. As is the case in many agricultural areas, the only data that exist in the SLV are hydraulic head measurements made in wells screened in the confined aquifer system.

Figure 5.5 shows the hydraulic head as measured in well CON2 in the SLV. The seasonal changes in head are due to variability groundwater pumping by agricultural water users from one year to the next. Farmers in agricultural areas initially rely on surface water resources to fulfill their irrigation needs. However, as precipitation levels vary from year to year in some instances farmers need to extract more groundwater to sustain their crops. If elastic deformation is assumed, the hydraulic head measurements in Figure 5.5 imply

that there would be too many seasonal changes in the amplitude and period of the deformation signal to be accurately represented by a sinusoidal function. The measurements in Figure 5.5 suggest that SBAS analysis should be modified so that it does not impose a low-pass deformation model on the raw interferometric data.

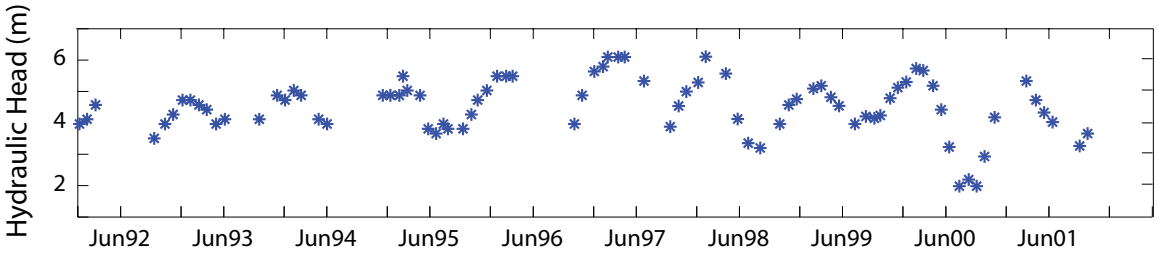

Figure 5.5: Hydraulic head measured in well CON2 in the San Luis Valley, Colorado.

Figure 5.6 shows the modified SBAS analysis processing steps. In this version of SBAS analysis 'Inversion 1' estimates the topographic correction and then removes this component of the phase from the unwrapped interferometric phases. In the upper half of Figure 5.6 the phase associated with deformation, with uncertainty due to atmospheric phase effects and uncertainty due to decorrelation remains. A temporal filter cannot be applied to these data to diminish the uncertainty due to atmospheric phase effects because the phase associated with the deformation would be removed in the process. For that reason the phase estimates from 'Inversion 2' will include information about the deformation along with uncertainty due to atmospheric phase effects and decorrelation.

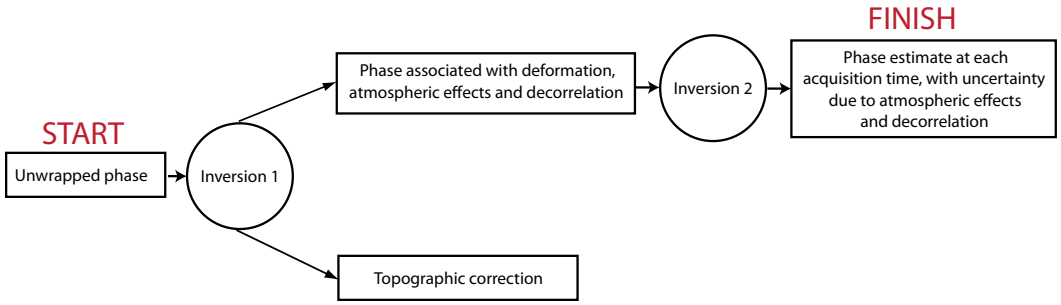

Figure 5.6: Small Baseline Subset (SBAS) analysis processing algorithm modified for groundwater applications.

5.6 Comparison of LOS time series and hydraulic head time series

The main objective of this section is to determine whether the deformation measurement obtained from the InSAR data in the SLV is of high enough quality to yield useful information about the variation in hydraulic head in the confined aquifer system. Because no GPS campaigns, leveling line surveys or extensometers measurements were performed and no extensometers were recording deformation in the SLV we are dependent on hydraulic head measurements and aquifer test data to validate the InSAR measurements in this agricultural area. We first compare the InSAR deformation measurements to the hydraulic head measurements in monitoring wells; the question being whether or not the deformation is capturing the expected seasonal variation in head. Then we predict hydraulic head from the InSAR deformation data, using an estimate of S_{ke} from an aquifer test (see equation 4.1). This predicted hydraulic head was compared to the hydraulic head measured in nearby monitoring wells. Locations that have high coherence InSAR data, hydraulic head measurements, and estimates of S_{ke} from aquifer

tests, are needed to perform this analysis.

In the following paragraph we describe how we determined appropriate locations at which to make the comparison between predicted and measured hydraulic head. As discussed in section 4.2, there are only 11 wells where we predict that the deformation will be large enough to be accurately measured by InSAR. There have been 151 aquifer tests in the confined aquifer system, however, only 17 of them provide estimates of *S*. There were six monitoring well/aquifer test well pairs that were collocated within 2 km of each other. However, upon further inspection we found that three of the monitoring wells either: a) did not exhibit seasonal pumping and recharge, or b) were not sampling the same portion of the aquifer system as the aquifer test wells. Therefore, the final dataset for comparison is: hydraulic head measurements from three monitoring wells and three aquifer test wells with estimates of *S*. The highest coherence pixel within 1 km of the monitoring well was selected to be the location of the LOS deformation measurements. At each of the three monitoring well locations the background phase gradient was low enough to justify a separation of 1 km. For these specific well locations this is a reasonable assumption, however in Chapter 6 we will revisit this issue for all wells in the SLV.

Figure 5.7, plots A), C) and E) show the LOS deformation time series for the three high coherence pixels (red markers). The location of each of the deformation time series is labeled as a cyan marker on Figure 5.8. The error in the InSAR measurement was estimated to be ~ 6 mm (shown as error bars in Figure 5.7). In general little attention is

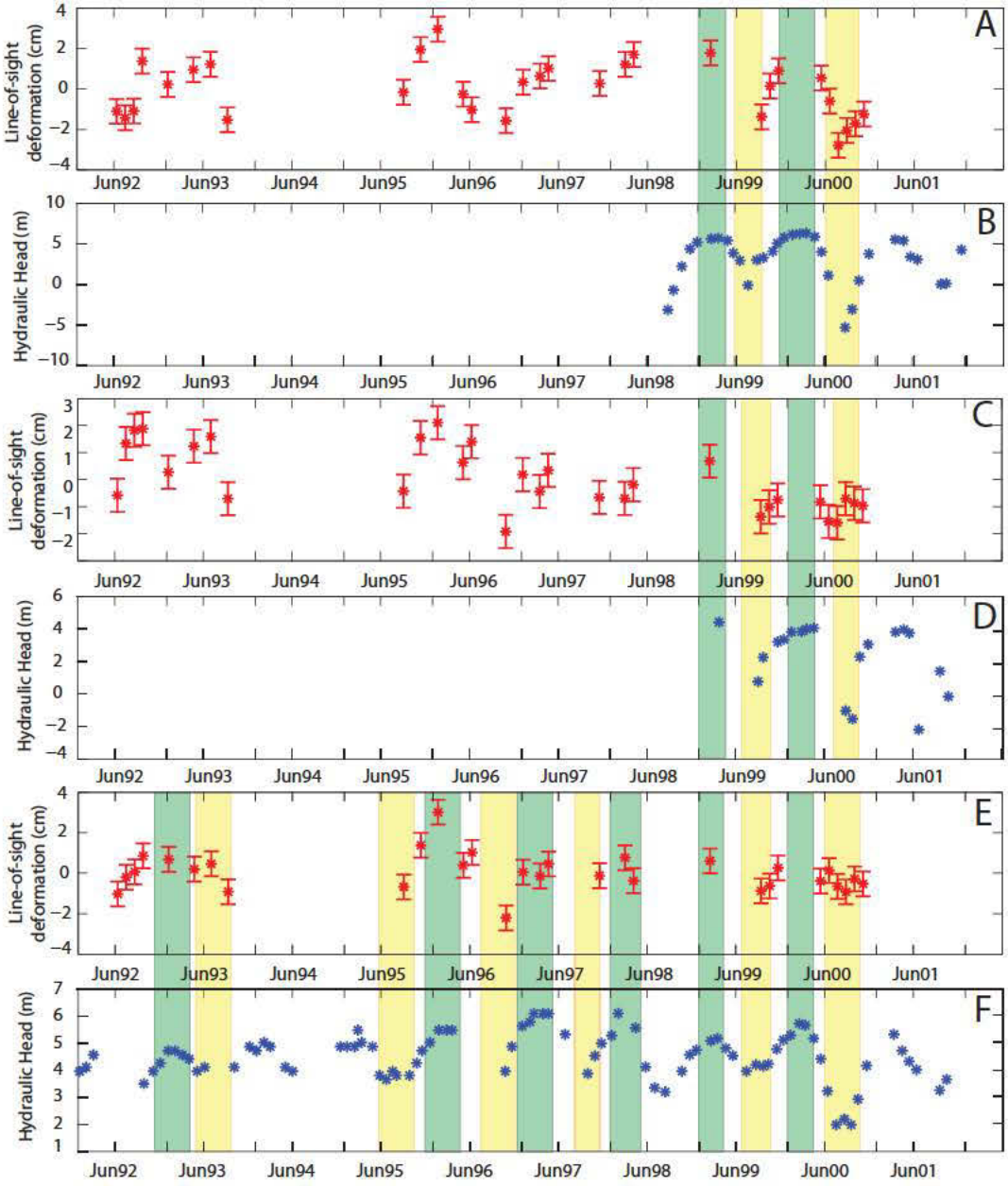

Figure 5.7: A), C) and E) LOS deformation time series for a high coherence pixel 1 km from ALA6, ALA13 and CON2 respectively. The position of these pixels are shown as cyan markers in Figure 5.8. B), D) and F) Hydrographs for well ALA6, ALA13 and CON2 respectively. The position of these wells are shown as blue markers in Figure 5.8. Green highlighted sections show when hydraulic head measurements were high, and yellow show when they were low.

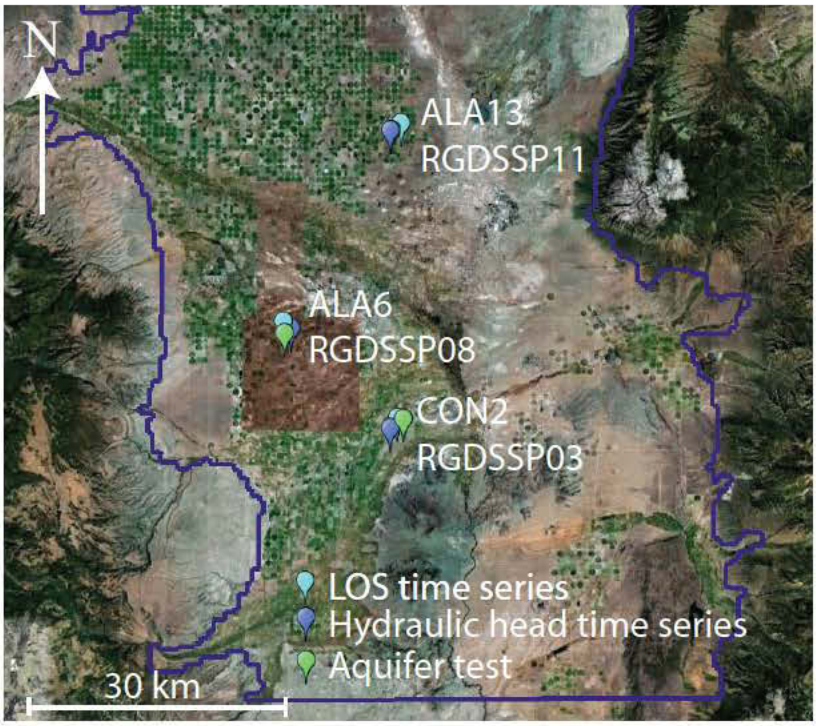

Figure 5.8: Map of the SLV showing the position of: LOS deformation time series (cyan marker), hydraulic head time series (blue marker) and the aquifer test locations (green marker).

paid to properly quantifying the error in InSAR measurements. The error in the interferometric phase was estimated by fitting a local plane to the unwrapped phases. This plane accounted for long-period errors. The standard deviation of the misfit to the plane gave the estimate of 6 mm. This estimate is similar to the error of ~ 5 mm given by *Hoffman et al.* (2002).

In Figure 5.7, plots B), D) and F) show the hydraulic head time series for the three monitoring wells ALA6, ALA13 and CON2 respectively (locations shown as blue markers Figure 5.8). In each case the corresponding LOS time series, shown in Figure

5.7 plots A), C), and E), are from the pixels with the highest coherence, within 1 km of the monitoring wells. The deformation and hydraulic head should be linearly related via the skeletal elastic storage coefficient S_{ke} (Equation 5.1). Figure 5.7 shows that the two time series appear to be linearly related.

We highlighted in green the times of the year when the hydraulic head in the monitoring well is high, and in yellow the times when the hydraulic head is low, see Figure 5.7. We compared hydraulic head and deformation only during time periods when both data were acquired. For all but a few occasions we can see that when the hydraulic head is high, the deformation indicates an upward movement of the ground surface, and when the hydraulic head is low the deformation indicates a downward movement. In general, the agreement of the two time-series is better at well ALA6 than at wells ALA13 and CON2. This may be a result of both the hydraulic head change and the deformation exhibiting a larger changes at this well location. Overall the periodicities of the measurements are in good agreement, suggesting that the deformation we are measuring with InSAR in the SLV is recording the seasonal changes in the hydraulic head in the confined aquifer system. This in itself is very useful information that could be used in a qualitative way to indicate when and where significant changes in head occur. In addition, as can be seen in Figure 5.7, InSAR provides us with data at times before head measurements were being made in many of the wells in the SLV. This longer period of monitoring is valuable for assessing long-term changes in the aquifer. For example, one important observation that can be made is the absence of a significant negative linear trend in the deformation in

Figure 5.7 A), C), and E). This supports the assumption that only elastic deformation is occurring in these regions of the SLV.

For each of the 11 wells described in section 4.2 (ALA6, ALA13 and CON2 inclusive) we estimated the linear trend in the deformation time-series. We found that all of the linear trends were negative, with a mean of approximately -0.07 cm/year. The linear trend at well RG88 was the largest (-0.15 cm/year). However, both the mean and the maximum value are both small enough to conclude that the deformation occurring at these well locations is elastic. This is a particularly important result, as it is at these well locations that we expected the deformation to be the largest, according to our initial calculations in Chapter 4.

5.7 Head estimates from InSAR deformation and aquifer test data

As a final validation of the deformation data, we estimated hydraulic head, derived from InSAR deformation data, and compared it to the measured Δh at the three monitoring wells (ALA6, ALA13, CON2). However, in order to make this comparison Δb (InSAR data) and S_{ke} (aquifer test well data) are required at the monitoring well locations (see Equation 5.1). As previously stated in section 5.6, we assumed that the deformation measured at the high coherence pixel is approximately the same as the deformation at the monitoring well (~1 km away). The aquifer test wells are: RGDSSP08, RGDSSP11 and RGDSSP03 (locations shown as green markers in Figure 5.8). The distance between aquifer test wells and monitoring wells is as follows: RGDSSP08 is 300 m from ALA6, RGDSSP11 is 100 m from ALA13 and RGDSSP03 is 2 km from CON2.

In order to use the estimates of S from the aquifer tests at the monitoring well locations the thickness of the producing zone, i.e. the thickness of the aquifer from which water is being withdrawn, for each well needs to be known.

During an aquifer test the obtained value of S depends upon the producing zone thicknesses (b^*) at the aquifer test well:

$$S = S_s b^*, \tag{5.2}$$

where S_s is the specific storage. The monitoring well and aquifer test well pairs were all producing from similar hydrogeologic units, and hence should exhibit similar values of S_s. However, the thickness of the producing zone varied because the wells were screened over different intervals. In order to use the value of S from the aquifer test well at the monitoring well location this disparity needed to be corrected for. The screened interval was used as the producing zone thickness at the aquifer test wells based on the assumption that flow into the well is horizontal: 23.8 m at RGDSSP08, 75.3 m at RGDSSP11 and 150.9 m at RGDSSP03. This producing zone thickness was used to calculate the specific storage, $S_s = S / b^*$. Using S_s and the producing zone thickness at the monitoring wells: 25.3 m at ALA6, 111.3 m at ALA13 and 110.0 m at CON2, S was calculated at the monitoring wells: $S = 1.4 \times 10^{-3}$ for ALA6, $S = 7.8 \times 10^{-4}$ for ALA13 and $S = 1.7 \times 10^{-3}$ for CON2. As discussed in section 5.2 the storage from the expansion and contraction of water (S_w) was assumed to be small, such that S can act as a proxy for S_{ke}.

The estimate of S_{ke} at the monitoring well location contains error from two main sources: performing the analytical fit to the recovering hydraulic head measurements and estimating the producing zone thicknesses. While quantification of the error in the analytical fit is normally not calculated, the measurements of S_{ke} from the aquifer tests should, in general, be accurate within 10% - 20% of the actual value [*Eric Harmon personal communication,* 2010]. We have no way of quantifying the error from estimating the producing zone thickness, therefore we neglected to account for it in this study. We used the average of the 10 – 20 % range, so assumed an error of $0.15S_{ke}$.

Figure 5.9 shows a comparison of the hydraulic head derived from InSAR measurements and the hydraulic head measurements. In general the hydraulic head is overestimated when compared to the measured hydraulic head. This suggests that the values for S_{ke} derived from the aquifer test are too low. This may be due to the uncertainty involved in identifying correct thickness for the producing zone. The error bars on the InSAR-derived head estimates contain both the 15% relative error in S_{ke} the 0.6 cm error in the deformation measurement and were calculated as follows:

$$\delta h = \Delta h \sqrt{\left(\frac{\delta b}{\Delta b}\right)^2 + \left(\frac{\delta S_{ke}}{S_{ke}}\right)^2}, \tag{4.4}$$

where δb is the error in Δb, δS_{ke} is the error in S_{ke} and δh is the error in Δh. The error bars were found to be quite large: approximately +/- 4.5 m, , +/- 8 m and +/- 3.5 m at ALA6, ALA13 and CON2 respectively.

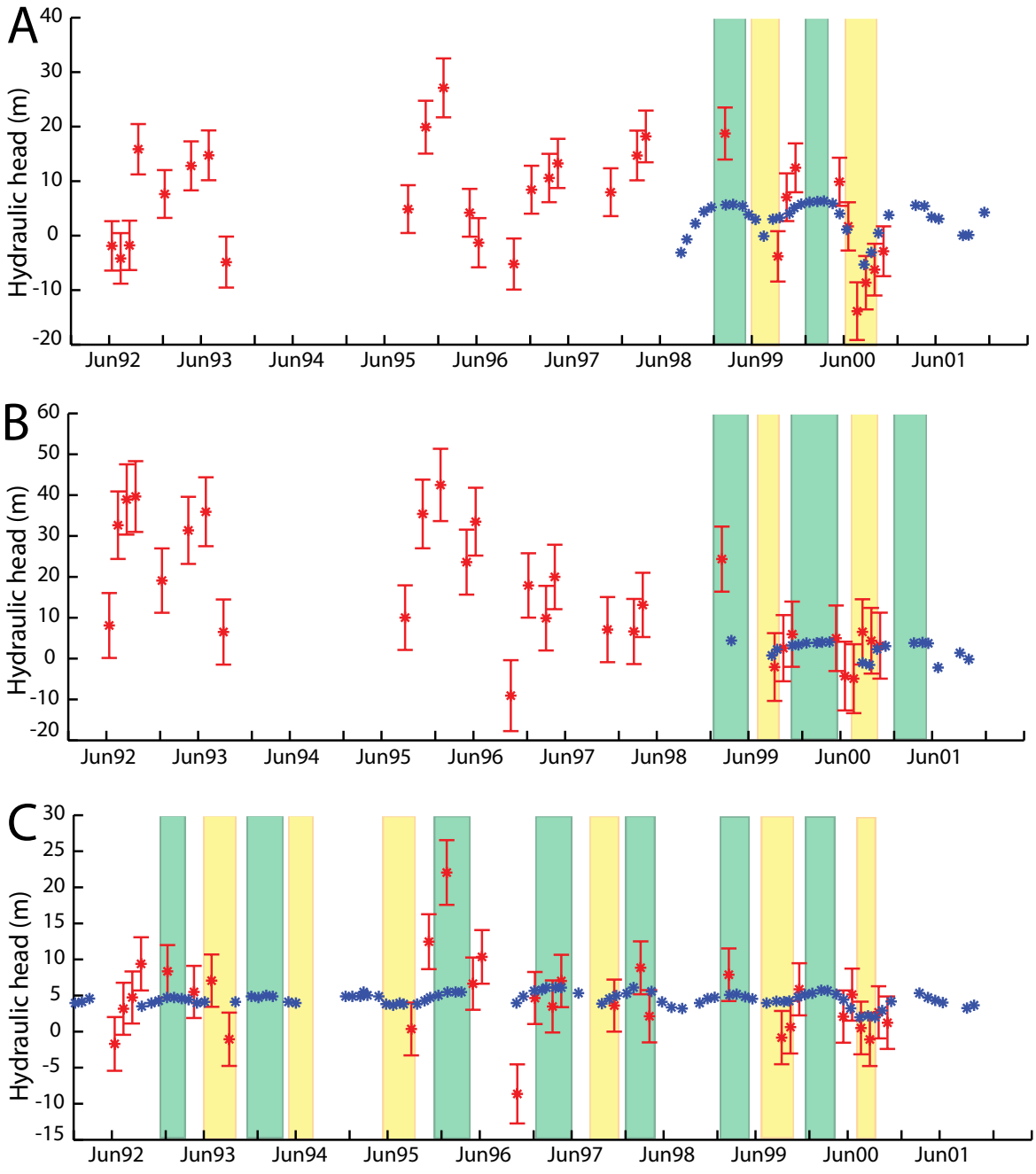

Figure 5.9: Estimated (red markers) and measured hydraulic head (blue markers). A) ALA6, B) ALA13 and C) CON2. Green highlighted sections show when hydraulic head measurements were high, and yellow show when they were low.

In many instances, as shown in Figure 5.9, the measured hydraulic head falls within the error bars of the estimated hydraulic head values. At well ALA6, five of the ten InSAR-derived head estimates fall within the error bars of the measured values; at ALA13, 9 of 10 agree; and at well CON 2, 20 of 31 agree. However, as discussed earlier, the error bars calculated were very large compared to the hydraulic head changes measured in the monitoring wells. Future research should focus on improving our ability to accurately determine the uncertainty in both S from aquifer tests as well as δb from the InSAR measurements. Only then will the method described above become a viable tool for predicting hydraulic head.

A number of spurious points occur in the InSAR-derived hydraulic head estimates: in February 1996 a large amount of upward deformation occurred and in November 1996 a large amount of downward deformation occurred. These outliers could have been caused by atmospheric phase effects. As described in section 5.5 the LOS deformation time-series was not filtered temporally to remove atmospheric phase effects.

5.8 Conclusions

Our first finding of significance in this thesis was the discovery that many of the small areas, left unwatered by the center-pivot irrigation systems, yielded high quality InSAR data when processed using SBAS methods. The InSAR deformation measurements showed the same seasonal periodicity as the hydraulic head data from monitoring wells. We also found that only elastic deformation was occurring from 1992 – 2000 at the 11 well locations identified in Chapter 4. This is a significant result in itself,

as it speaks towards the sustainability of groundwater extraction from the confined aquifer system.

When hydraulic head was estimated from the InSAR data, we found good agreement between the estimated hydraulic head and the measured head values (within the error bars). However, we acknowledge that the errors are so large that these hydraulic head estimates would not provide the level of accuracy required for the RGDSS. The uncertainty in the hydraulic head estimates is dependent on the uncertainty in S_{ke} and the uncertainty in the InSAR deformation measurements. It is clear that more research is required to understand how best to predict head from InSAR data. Can this be done using the field measurements of S_{ke} if we can improve the accuracy of the measurement? Or should we assume that the use of InSAR data to obtain head estimates will always require calibration, with wells in selected regions instrumented specifically for this purpose? In either case an improved understanding of the uncertainty in the InSAR deformation measurement is necessary before these data can be used for groundwater applications. Therefore, Chapter 6 will focus on quantifying the spatially variable uncertainty in the InSAR deformation measurement. In Chapter 7 of this thesis we will revisit the issue of calibration by investigating the relationship between deformation and hydraulic head at the 11 confined aquifer wells from Chapter 4.

Despite the fact that we cannot yet accurately obtain hydraulic head estimates from the InSAR data, we conclude that we can obtain high quality InSAR data from the SLV, and that these data capture useful information about the seasonal variability in head. Once we

determine how to accurately obtain hydraulic head from InSAR data, it is easy to see from Figure 5.9 that a host of new data will become available to water managers. For example, at ALA6 and ALA13, where hydraulic head data have only been collected since 1999 the InSAR data will be able to provide estimates of hydraulic head back to 1992. The hope is that InSAR data from this region can also be used going forward as an integral part of hydrogeologic modeling and monitoring in the valley.

Chapter 6
Quantifying uncertainty in the InSAR measurement

6.1 Introduction

In the previous chapter we showed that Interferometric Synthetic Aperture Radar (InSAR) deformation measurements exhibit seasonal trends similar to hydraulic head levels in the confined aquifer system of an agricultural area. However, when we attempted to obtain hydraulic head from the InSAR deformation measurements we found that our estimate of the uncertainty of these measurements was not sufficiently accurate. Moreover, for our initial analysis of InSAR data quality in Chapter 5 we used the closest high quality pixel to the well location to make the comparison with hydraulic head. Figure 6.1a) shows high quality InSAR data from an urban/arid area and Figure 6.1b) shows the sparse high quality data from vegetated areas like the San Luis Valley (SLV). Because we know that the quality of the data, i.e. the coherence, is changing from pixel to pixel in vegetated areas of the SLV it would be ideal to determine the exact uncertainty at each pixel before we revisit the relationship between deformation and hydraulic head

again in Chapter 7. One of the main goals of this chapter is to determine the spatial variability in the uncertainty in the InSAR measured deformation (sections 6.2 and 6.3). Further, we show that we can process the InSAR data to ensure some pre-selected acceptable level of uncertainty in the final deformation estimates (section 6.4). The work completed in this chapter of the thesis is currently in revision for publication in the journal Institute for Electrical and Electronic Engineers (IEEE) Transactions on Geoscience and Remote Sensing [*Reeves et al.,* in revision].

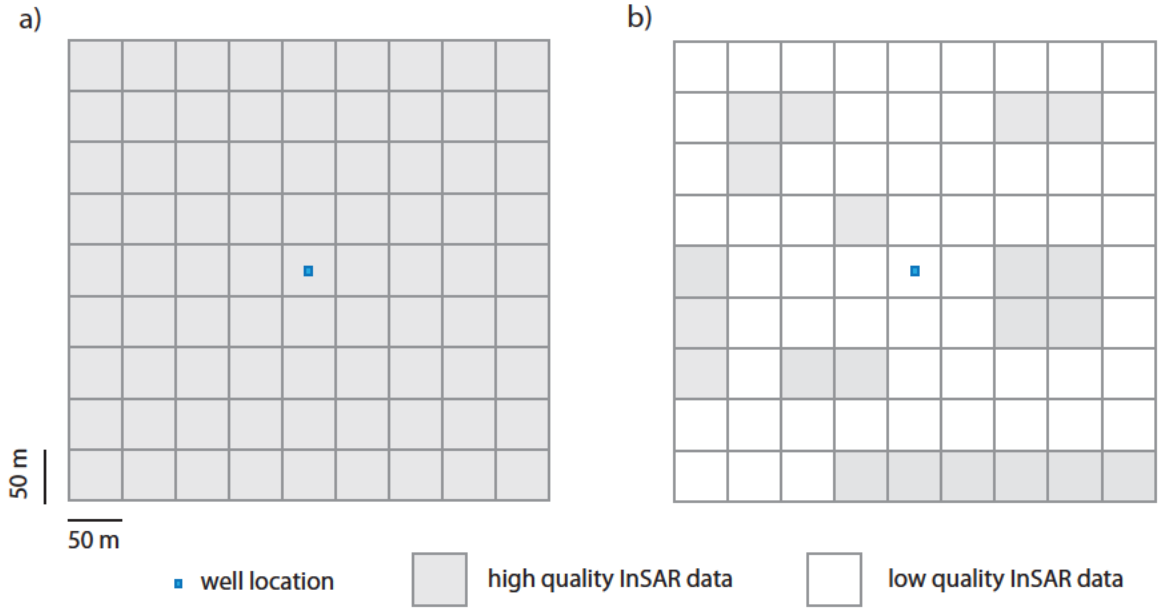

Figure 6.1: A schematic showing a) high quality InSAR deformation data at all pixels in arid/urban environments, and b) high and low quality InSAR deformation data in vegetated areas like the SLV.

As discussed in sections 2.1.1 and 2.1.2, there are four major components that contribute to uncertainty in the measurement of interferometric phase (σ_ϕ): integer phase ambiguities, incorrect orbital parameters, atmospheric phase effects and decorrelation of

radar signals. These components were discussed at length in *Hanssen* (2001). In this chapter we address two of these components: atmospheric phase effects and decorrelation of radar signals, as we have found that these two components have the largest effect on the uncertainty of the InSAR deformation measurement in the SLV. The other two components, integer phase ambiguities and incorrect orbital parameters, do not have a large effect on the uncertainty in the SLV and were previously discussed in section 2.1.1 and 2.1.2.

As discussed in section 2.1.2 a number of studies have attempted to quantify the uncertainty due to atmospheric phase effects (*Onn and Zebker*, 2006; *Knospe and Jonsson*, 2010). Instead of directly modeling the uncertainty due to this component, as done in the two studies mentioned above, we propose using supplementary hydrologic data from the SLV in order to identify which scenes may contain large amounts of atmospheric phase effects and then eliminating them from our analysis. In section 6.2 of this chapter we demonstrate our proposed methodology, first on a synthetic data set and then on data from the SLV.

Once we reduce the uncertainty due to atmospheric phase effects by eliminating the noisiest scenes, the dominant remaining component of uncertainty is associated with the decorrelation of radar signals. Two seminal studies, *Zebker and Villasenor* (1992) and *Hanssen* (2001) have quantified the uncertainty in the interferometric phase due to decorrelation. However, in studies where the data are being used to better understand a physical process (e.g., an earthquake, a volcanic eruption, or groundwater extraction)

most authors avoid propagating this component of uncertainty through the InSAR processing chain. Propagating these uncertainties is computationally intensive and often Global Positioning System (GPS) measurements are instead used to validate the data. Also, in general, most studies have looked at large magnitude deformation that was well understood and easily modeled. In the SLV we are measuring smaller seasonal signals that take place over short timescales. In our case the uncertainty due to decorrelation may have a large impact on our results. A few studies applying multi-temporal techniques (small baseline subset (SBAS) analysis or persistent scatterer (PS) analysis) have considered propagating uncertainty due to decorrelation through the processing chain [*Hooper et al.*, 2004; *Kwoun et al.*, 2006; *Guarnieri and Tebaldini*, 2007; *Rocca*, 2007; *Anderssohn et al.*, 2009; *Gonzalez and Fernandez*, 2011].

In this chapter we use SBAS analysis to process our InSAR data. In non-urban terrains, like the SLV, the scattering mechanism for the EM waves is described as distributed. For distributed scattering all scattering elements in a resolution cell reflect the EM wave with the same strength. SBAS analysis is an appropriate technique for processing data in areas where a distributed scattering mechanism dominates [*Agram*, 2010]. In section 6.3 we take a similar approach and propagate the uncertainty due to decorrelation through the SBAS analysis processing chain for all 1.5 million pixels in the SLV. In order to do so we use the modified SBAS analysis presented in section 5.5 to accommodate signal characteristics specific to groundwater applications and we describe mathematically how uncertainty propagates through this processing chain. This methodology provides a measure of uncertainty for each deformation estimate at each acquisition time.

There are two decision points during SBAS analysis processing where we answer the following questions: a) what should the spatial and temporal baseline thresholds be, and b) what is an acceptable threshold for the decorrelation of a pixel? Setting the thresholds for the spatial and temporal baselines limits the number of interferograms used in SBAS analysis, and setting the threshold for the decorrelation limits the number of pixels selected for further processing. These thresholds have previously been set in a fairly ad hoc manner [*Berardino et al.*, 2002; *Lauknes*, 2004]. In section 6.4 we determine appropriate threshold parameters in order to meet some predetermined level of uncertainty in the final deformation time-series.

The ultimate goal of our research is to find a way to use InSAR deformation measurements to obtain hydraulic head in confined aquifer systems. Quantifying the spatial variability of the uncertainty in the deformation measurement is an important step in this process. We begin our study by outlining an algorithm that uses additional hydrologic data to diminish the amount of uncertainty due to atmospheric phase effects.

6.2 Atmospheric Uncertainty in the SLV

Quantifying the uncertainty in the InSAR deformation estimate due to atmospheric phase effects can be very complicated. The structure of the atmosphere used to model these effects is often oversimplified and model results do not accurately represent the atmospheric phase signal seen in real data. Because this component of the uncertainty is difficult to quantify, we have decided to use supplementary hydrologic data

to identify and remove the parts of our scenes corrupted by atmospheric phase effects for pixels in close proximity to the well measurements. The remaining measurements of phase will contain minimal amounts of error due to atmospheric phase effects.

Figure 6.2 shows surface deformation estimated from InSAR data in the SLV from October to November 1995 [*Reeves et al., 2011*]. We spatially smoothed and interpolated the deformation estimates to highlight certain spatial features. In the SLV we know that during autumn the ground surface should be moving upwards due to precipitation recharging the confined aquifer system. In Figure 6.2 we can see that in general the motion is positive towards the satellite (hot colors). The blue box labeled A in Figure 6.2 shows a seasonal deformation signal. We have identified a similar signal in a number of other interferograms, which we attributed to deformation due to groundwater recharge and withdrawal (see section 5.4). The blue box labeled B shows a number of light green bands of phase change, which are commonly associated with atmospheric phase effects. In section 5.6 we established that we cannot identify a low-pass deformation model that is appropriate for the SLV data, and hence cannot remove atmospheric phase effects by applying a temporal filter. At this point we do not wish to simply remove the entire scene with the associated atmospheric signal. To remove this entire scene would mean discarding the data in box A that we believe are not significantly corrupted with atmospheric phase effects. Here we describe a method that uses auxiliary hydraulic data to differentiate between atmospheric phase effects and deformation that could be due to seasonal groundwater change.

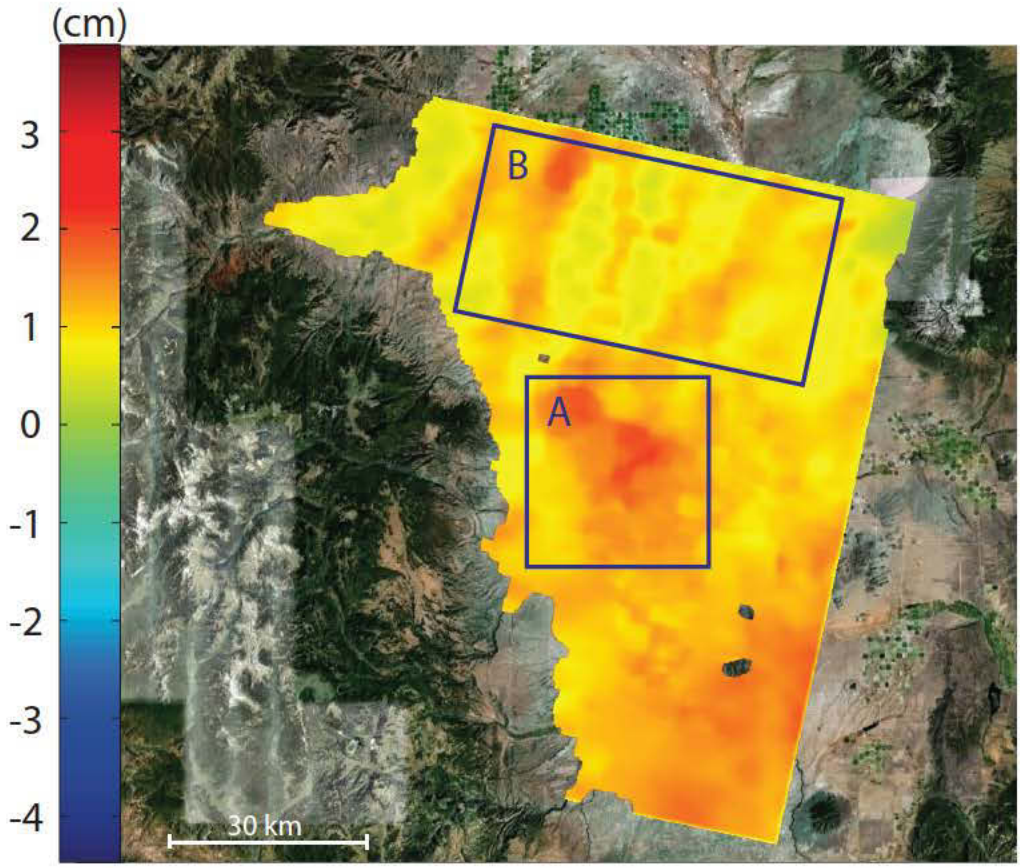

Figure 6.2: The estimated deformation (interpolated) from September to November 1995 in the San Luis Valley. Positive deformation is towards the satellite (hot colors), negative deformation is away from the satellite (cool colors). Box A shows the deformation that can be attributed to seasonal hydraulic head change and box B shows remnant atmospheric phase effects (see section 5.4).

6.2.1 Method

In the SLV we have access to hydrologic data that allows us to identify the times of year when the deformation should be moving towards or away from the satellite. Figure 6.3 shows the hydraulic head data from well CON2 during 1995 and 1996. The red line in the figure shows the time span of an interferogram from October 1995 to

February 1996. Based on the hydraulic head data during this time period, we know that the change in phase should be positive for nearby pixels. We rank the scenes according to the number of times they have been used to create an interferogram that shows a trend in the deformation that is in contrast to the trend in the hydraulic head. Those scenes with a high rank are not used during SBAS analysis for all pixels close to the well. We first apply this analysis on a synthetic data set, and then investigate a high coherence pixel close to well CON2 in the SLV.

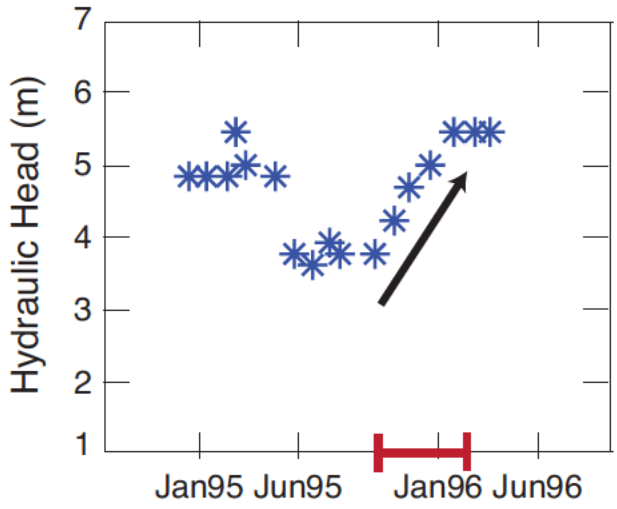

Figure 6.3: Hydraulic head data from well CON2 during 1995 and 1996. The red line shows the time span of an interferogram from October 1995 to February 1996. Given the well data we expect the change in phase to be positive in pixels close to well CON2.

6.2.2 Results and Discussion

The synthetic dataset we used was based on the deformation we would expect to see at pixels near well CON2. We converted the hydraulic head data from well CON2

into deformation by assuming elastic deformation (equation 5.1). We assumed that Δb is equal to the deformation of the ground surface as measured by InSAR and that $S_{ke} \approx 0.003$, a reasonable value for this area of the SLV [*RGDSS*, 2005]. We added Gaussian white noise such that the signal to noise ratio (SNR) of the synthetic dataset was ~ 20 dB. We converted the deformation measurements into phase measurements based on ERS-1 and ERS-2 system parameters. In Figure 6.4 the solid blue line shows the synthetic data, phase as a function of time.

To generate the synthetic data,we randomly selected 30 acquisition times, and added a phase delay simulating atmospheric phase effects to three random scenes (December 1999, December 2000, and September 2001). We assigned random spatial baselines to the scenes and created interferograms for scene pairs with a perpendicular baseline of less than 400 m and a temporal baseline of less than 4 years. We then applied the algorithm as described in section 6.2.1, the result of which is a list of ranked scenes. We removed the scene with the highest rank, and repeated the algorithm iteratively. The algorithm was finished when the scenes remaining were those which had been used in only one interferogram showing deformation opposite to the trend predicted from the head measurements.

We then removed the scenes that the algorithm identified as containing significant atmospheric phase effects and solved for the phase at each acquisition time. Figure 6.4 shows the phase estimates in red, when we used all the scenes, including the ones containing atmospheric phase effects, and phase estimates in blue when we removed

them. We can see that the three phase estimates circled in green were properly removed as they contained atmospheric phase effects. The three phase estimates circled in purple are scenes that did not have atmospheric phase added to them, but were also removed. We can see that when comparing those scenes to the true solution the estimated phase trends do not agree with the true phase trends. This is due to the level of Gaussian white noise added to the dataset. We find that our algorithm is able to identify scenes with atmospheric signal, but also selects other scenes that do not display the correct trend due to the presence of noise in the data.

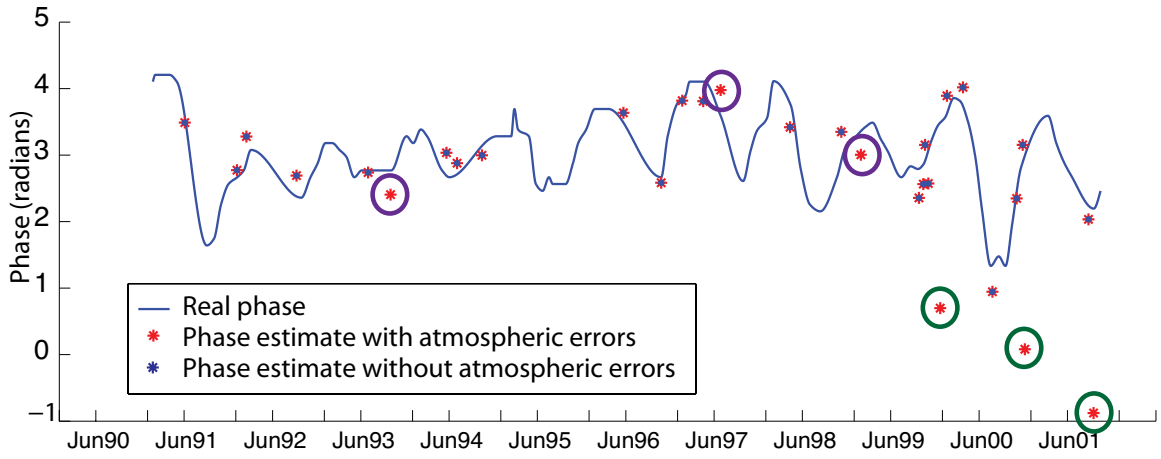

Figure 6.4: The blue line is the true solution of the phase, the red markers show the phase estimate when atmospheric scenes are included in the inversion, and the blue markers show the phase estimate when atmospheric scenes are removed. The green circles identify the three scenes that had an atmospheric delay added and were removed. The purple circles identify three other scenes that were removed because of the Gaussian white noise added to the dataset.

Next we applied the same algorithm to data from the SLV. We used the hydraulic head data from well CON2 and the deformation measurements from a nearby high coherence pixel. In Figure 6.5 the red markers show the results from using all 31 scenes, which created 96 interferograms. The blue markers show that our analysis removed 11 scenes, limiting our interferogram count to 32. We can see that in the case of these data the phase estimates at each acquisition time changed, because more than 1/3 of the input data were removed.

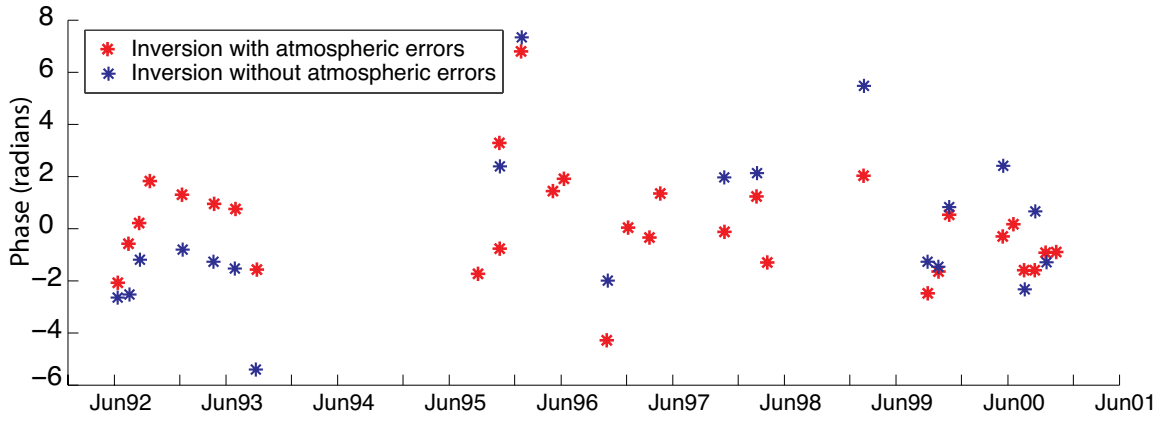

Figure 6.5: The estimated phase for a high coherence pixel near well CON2. The red markers show the phase estimate when atmospheric scenes are included in the inversion, and the blue markers show the phase estimate when atmospheric scenes are removed.

Because we do not have any other deformation data to assess our results, it is difficult to say whether or not the algorithm is working well when applied to data acquired from the SLV. However, we can validate our results by examining maps of the final deformation estimates for the scenes that were removed to see if they exhibit visible atmospheric artifacts around the high coherence pixel in question. All of the scenes we removed had a

pattern structure that resembled atmospheric phase effects near well CON2. However, it is also important to note that patterns that show atmospheric phase effects can take many different forms [*Knospe and Johnsson, 2010*]. Both scenes that were used to create the deformation in Figure 6.2 were removed, September 1995 and November 1995. This technique shows an inherent trade off between the amount of atmospheric signal that remains in the final time series and adequate sampling of the final time series. Although we are not able to quantify the uncertainty due to atmospheric phase effects we are at least able to remove the scenes, on a pixel-by-pixel basis, that may contain large amounts of uncertainty in measured deformation due to atmospheric phase effects.

6.3 Propagation of uncertainty due to decorrelation

Now that we have proposed a method to reduce the uncertainty due to atmospheric phase effects we can continue our investigation by propagating the uncertainty in the interferometric phase through the SBAS analysis processing chain. In section 6.1 we stated that we could only quantify the uncertainty due to decorrelation, which is quantified by the coherence. The sections to follow will focus solely on this component of the uncertainty.

6.3.1 Uncertainty in the interferometric phase

We define the uncertainty in the interferometric phase measurement as its standard deviation (σ):

$$\sigma = \sqrt{\int_{-\pi}^{\pi} \left(\phi - E\{\phi\}\right)^2 pdf(\phi) d\phi}, \tag{6.1}$$

where $E\{\phi\}$ is the expected value of the interferometric phase, and $pdf(\phi)$ is the probability density function of the interferometric phase. The $pdf(\phi)$ is given as [*Goodman*, 1963; *Barber*, 1993; *Lee et al.*, 1994; *Tough et al.*, 1995]:

$$pdf(\phi;\gamma,L,\phi_0) = \frac{\left(1-|\gamma|^2\right)^L}{2\pi}\left\{\frac{\Gamma(2L-1)}{\left[\Gamma(L)\right]^2 2^{2(L-1)}} \times \left[\frac{(2L-1)\beta}{(1-\beta^2)^{L+1/2}}\left(\frac{\pi}{2}+arcsin\beta\right)+\frac{1}{\left(1-\beta^2\right)^L}\right] + \frac{1}{2(L-1)}\sum_{r=0}^{L-2}\frac{\Gamma(L-1/2)}{\Gamma(L-1/2-r)}\frac{\Gamma(L-1-r)}{\Gamma(L-1)}\frac{1+(2r+1)\beta^2}{(1-\beta^2)^{r+2}}\right\}$$

$$\begin{aligned} &\gamma = \text{ coherence} \\ &L = \text{ number of independent looks} \\ &\text{with } \phi_0 = \text{ the measured difference in phase.} \\ &\beta = |\gamma| cos(\phi - \phi_0) \\ &\Gamma(L) = \int_0^\infty t^{L-1} e^{-t} dt \end{aligned} \tag{6.2}$$

Since $pdf(\phi)$ is symmetric about ϕ_0 we know that $E\{\phi\} = \phi_0$. We can now calculate the standard deviation of the interferometric phase as a function of the coherence and the number of independent looks.

6.3.2 Propagating uncertainty through SBAS analysis

We propagate the uncertainty in the interferometric phase through the two SBAS inversions discussed in section 4.6. Both inversions use a Singular Value Decomposition

(SVD) to calculate the generalized inverse (G_{gen}) of the design matrix (G). Using G_{gen} and the data covariance matrix (Σ_d) we can calculate the model covariance as follows:

$$\Sigma_m = G_{gen}\Sigma_d\left(G_{gen}\right)^T. \tag{6.3}$$

Below we will outline how to create the Σ_d for both 'Inversion 1' and 'Inversion 2' from Figure 5.6.

In 'Inversion 1' we estimate the topographic correction (Δz). We will need the data covariance matrix (Σ_d) for the interferometric phases in order to propagate the uncertainty through this inversion. Along the diagonal of Σ_d are interferometric phase variances, σ^2. However, interferograms that are made using a common scene have an associated data covariance; these appear as off diagonal values in Σ_d. In the calculations to follow we will show how we arrived at the data covariance for two interferograms that are formed with a common scene.

The measured phase for a single scene is denoted by ψ. This phase has a deterministic component (d) and a stochastic component (r), such that $\psi = d + r$. The interferometric phase (ϕ) for an interferogram formed between two scenes at time 1 and time 2 is as follows:

$$\phi_{12} = \psi_1 - \psi_2. \tag{6.4}$$

If we also have an interferogram formed between a scene at time 2 and a scene at time 3, then the interferometric phase would be given by:

$$\phi_{23} = \psi_2 - \psi_3 . \tag{6.5}$$

Because the measurement ψ_2 is a component of both ϕ_{12} and ϕ_{23} we suggest that the two interferometric phases are correlated. More formally, we need to find the covariance of two interferometric phase measurements, in this example ϕ_{12} and ϕ_{23}:

$$\begin{aligned} Cov(\phi_{12},\phi_{23}) &= E(\phi_{12}\phi_{23}) - E(\phi_{12})E(\phi_{23}) \\ &= E((\psi_1 - \psi_2)(\psi_2 - \psi_3)) - (d_1 - d_2)(d_2 - d_3) \\ &= E(\psi_1\psi_2) - E(\psi_1\psi_3) - E(\psi_2\psi_2) + E(\psi_2\psi_3) - d_1d_2 + d_1d_3 + d_2d_2 - d_2d_3 \end{aligned} . \tag{6.6}$$

We can then substitute $\psi_1 = d_1 + r_1$, $\psi_2 = d_2 + r_2$, and $\psi_3 = d_3 + r_3$ into the first four terms of the above equation:

$$\begin{aligned} Cov(\phi_{12},\phi_{23}) = {} & E((d_1 + r_1)(d_2 + r_2)) - E((d_1 + r_1)(d_3 + r_3)) - E((d_2 + r_2)(d_2 + r_2)) + E((d_2 + r_2)(d_3 + r_3))... \\ & ... - d_1d_2 + d_1d_3 + d_2d_2 - d_2d_3 \end{aligned} . \tag{6.7}$$

If we expand the first four terms we can remove the terms involving $E(d_m r_n)$ or $E(r_m r_n)$ because they are not correlated and their expected value will be zero. This leaves the following:

$$Cov(\phi_{12},\phi_{23}) = E(d_1d_2) - E(d_1d_3) - E(d_2d_2) - E(r_2r_2) + E(d_2d_3) - d_1d_2 + d_1d_3 + d_2d_2 - d_2d_3$$
$$= -E(r_2^{\,2})$$

. (6.8)

If we know the variance of ϕ_{12} then we can show that:

$$\begin{aligned} Var(\phi_{12}) &= E(\phi_{12}^{\,2}) - E(\phi_{12})^2 \\ &= E((\psi_1 - \psi_2)(\psi_1 - \psi_2)) - (d_1 - d_2)^2 \\ &= E(\psi_1\psi_1) - 2E(\psi_1\psi_2) + E(\psi_2\psi_2) - d_1^{\,2} + 2d_1d_2 - d_2^{\,2} \\ &= E(d_1^{\,2}) + E(r_1^{\,2}) - 2E(d_1d_2) + E(d_2^{\,2}) + E(r_2^{\,2}) - d_1^{\,2} + 2d_1d_2 - d_2^{\,2} \\ &= E(r_1^{\,2}) + E(r_2^{\,2}) \end{aligned}$$

. (6.9)

If we assume that $Var(r_1) = Var(r_2)$, then $Var(\phi_{12}) = 2E(r_2^{\,2})$, and we can calculate the covariance given above. A similar calculation yields $Var(\phi_{23}) = 2E(r_2^{\,2})$. However, because we know that the coherence changes for each interferogram we infer that $Var(\phi_{12})$ is not equal to $Var(\phi_{23})$. In order to reconcile this difference we use the average of $Var(\phi_{12})$ and $Var(\phi_{23})$ for the expectation. In doing so, we achieve physically plausible results, although we know that there are other unidentified systematic errors that are neglected in our analysis. We find that this is the best way to honor the data covariance between interferograms without knowing the joint probability density functions for the measured phases. Therefore the final estimate of the covariance is as follows:

$$Cov(\phi_{12},\phi_{23}) = -E(r_2^{\,2}) = -\left(\frac{Var(\phi_{12}) + Var(\phi_{23})}{2}\right). \qquad (6.10)$$

Σ_d has the interferometric phase variances along the diagonal and covariances for interferograms derived from a common scene for all non-zero off diagonal elements. Using equation 6.3 we calculate Σ_m, which gives us the variance of the topographic correction *Var(*Δz*)*.

Once we estimate Δz from 'Inversion 1' we need to remove this component of the phase from the measured interferometric phase:

$$\Delta\phi_D = \Delta\phi - c\Delta z \tag{6.11}$$

where $\Delta\phi_d$ are the components of the phase measurement due to deformation and $\Delta\phi$ are the measured interferometric phases. The matrix c describes how Δz, estimated in meters, can be converted into phase

$$c = \frac{4\pi B_{perp}}{\lambda r \sin\theta}, \tag{6.12}$$

where λ is the wavelength, B_{perp} is the perpendicular component of the baseline between satellite locations at acquisition, r is the range distance and θ is the incidence angle with respect to Earth's surface [*Berardino et al., 2002*]. Although recent research suggests that using the difference between B_{perp}*(scene1,reference)* and B_{perp}*(scene2,reference)* is more accurate, during initial synthetic studies we found that using B_{perp} for the interferogram was sufficient for our analysis [*Fattahi and Amelung, 2013*]. $\Delta\phi_d$ are the data for 'Inversion 2' in Figure 5.6. We now need to construct the data covariance matrix for $\Delta\phi_d$.

We can calculate the variance of the phase measurement due to deformation for interferogram 1 ($\Delta\phi_{D1}$) as follows:

$$\begin{aligned} Var(\Delta\phi_{D1}) &= E(\Delta\phi_{D1}{}^2) - E(\Delta\phi_{D1})^2 \\ &= E((\Delta\phi_1 - c(1,1)\Delta z)^2) - E(\Delta\phi_1 - c(1,1)\Delta z)^2 \\ &= E(\Delta\phi_1{}^2) - 2c(1,1)E(\Delta\phi_1\Delta z) + c(1,1)^2 E(\Delta z^2) - (E(\Delta\phi_1) - c(1,1)E(\Delta z))^2 \end{aligned} . \quad (6.13)$$

We know that $\Delta\hat{z} = c^{-1}\Delta\phi$ from 'Inversion 1', where c^{-1} is the generalized inverse of c and $\Delta\phi$ is the vector containing the interferometric phases. If we substitute that into the second term in equation 6.11 and simplify we get:

$$\begin{aligned} Var(\Delta\phi_{D1}) &= E(\Delta\phi_1{}^2) - 2c(1,1)\cdot\bar{c}^{-1}E(\Delta\phi_1\Delta\bar{\phi}) + c(1,1)^2 E(\Delta z^2) - (E(\Delta\phi_1) - c(1,1)E(\Delta z))^2 \\ &= Var(\Delta\phi_1) - 2c(1,1)\cdot\bar{c}^{-1}Cov(\Delta\phi_1,\Delta\bar{\phi}) + c(1,1)^2 Var(\Delta z) \end{aligned} . \quad (6.14)$$

The covariance is calculated in a similar way. We can use the example of $\Delta\phi_{D1} = \Delta\phi_1 - c(1,1)\,\Delta z$ and $\Delta\phi_{D2} = \Delta\phi_2 - c(2,1)\,\Delta z$:

$$\begin{aligned} Cov(\Delta\phi_{D1},\Delta\phi_{D2}) &= E(\Delta\phi_{D1}\Delta\phi_{D2}) - E(\Delta\phi_{D1})E(\Delta\phi_{D2}) \\ &= E((\Delta\phi_1 - c(1,1)\Delta z)(\Delta\phi_2 - c(2,1)\Delta z)) - E(\Delta\phi_1 - c(1,1)\Delta z)E(\Delta\phi_2 - c(2,1)\Delta z) \\ &= Cov(\Delta\phi_1,\Delta\phi_2) - c(1,1)\cdot\bar{c}^{-1}Cov(\Delta\phi_2,\Delta\bar{\phi}) - c(2,1)\cdot\bar{c}^{-1}Cov(\Delta\phi_1,\Delta\bar{\phi}) + c(1,1)c(2,1)Var(\Delta z) \end{aligned} . \quad (6.15)$$

Σ_d has the variances of $\Delta\phi_D$ along the diagonal and the covariances of $\Delta\phi_D$ for interferograms that were made using a common scene for all non-zero off diagonal elements. Once again, using equation 6.3 we can calculate Σ_m, which gives us the

variance of the estimated phase at each acquisition time *Var(ϕ)*. We have now shown how to propagate the uncertainty from the data covariance matrix for the interferometric phases to the variance of the phase estimated at each acquisition time. In the section to follow we implement this routine using data acquired from the SLV.

6.3.3 Propagating the uncertainty of the SLV InSAR data

We propagated the uncertainty in the interferometric phase for the same data as described in section 3.5 (31 scenes from the ERS-1 and ERS-2 satellites). In order use equations 6.1 and 6.2 to relate the standard deviation of the interferometric phase to the coherence we first need to quantify the number of independent looks for the ERS satellites. The number of independent looks L is given by the following formula:

$$L = \frac{\text{pixel area}}{\text{resolution cell area}} \times \text{N} \tag{6.16}$$

where N is the number of averaged pixels. In this study we averaged 2 pixels in range and 8 in azimuth, making N = 16. The pixel area is calculated by multiplying the pixel size in the azimuth direction (Δ_{a-p}) by the pixel size in the range direction (Δ_{r-p}):

$$\begin{aligned} \Delta_{a-p} &= v / PRF = 4 \text{ m} \\ \Delta_{r-p} &= c / 2 f_s = 20 \text{ m} \\ \text{pixel area } &= \Delta_{a-p} \cdot \Delta_{r-p} = 80 \text{ m}^2 \end{aligned} \tag{6.17}$$

where v is the velocity of the satellite (7550 m/s), PRF is the pulse repetition frequency (1680 Hz), c is the speed of light (2.99E8 m/s) and f_s is the sampling frequency (18.96 MHz) [*Hoen*, 2001]. The resolution cell area is given by the following formula:

$$\begin{gathered} \Delta_{a-rc} = l/2 = 5 \text{ m} \\ \Delta_{r-rc} = c/2BW = 25 \text{ m} \\ \text{resolution cell area } = \Delta_{a-rc} \cdot \Delta_{r-rc} = 125 \text{ m}^2 \end{gathered} \tag{6.18}$$

where Δ_{a-rc} and Δ_{a-rc} are for the resolution cell size, l is the length of the antenna (10 m) and BW is the bandwidth of the radar system (15.55 MHz) [*Hoen*, 2001]. From equation 6.16, L = 10. For L = 10 we use equation 6.1 to relate the standard deviation of the interferometric phase to the coherence. Figure 6.6 is a plot of the standard deviation of the interferometric phase as a function of the coherence.

We used the relationship shown in Figure 6.6 for the ERS satellites to create the data covariance matrix for 'Inversion 1' from Figure 5.6. Using the method described in section 6.3.2 we propagated the uncertainty through the SBAS analysis processing chain for each of the 1.5 million selected pixels in the SLV. Figure 6.7 is a plot of the deformation at a high coherence pixel near well ALA6. The error bars show the standard deviation of the final deformation estimates.

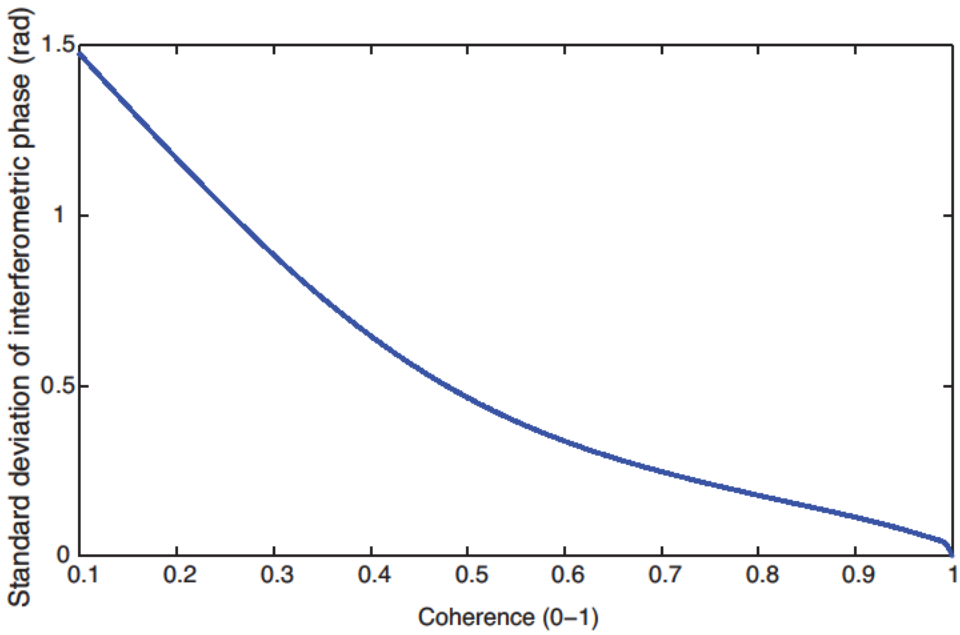

Figure 6.6: The relationship between coherence and the standard deviation of the interferometric phase for L = 10, for the ERS satellite system with the parameters discussed in equations 6.17 and 6.18.

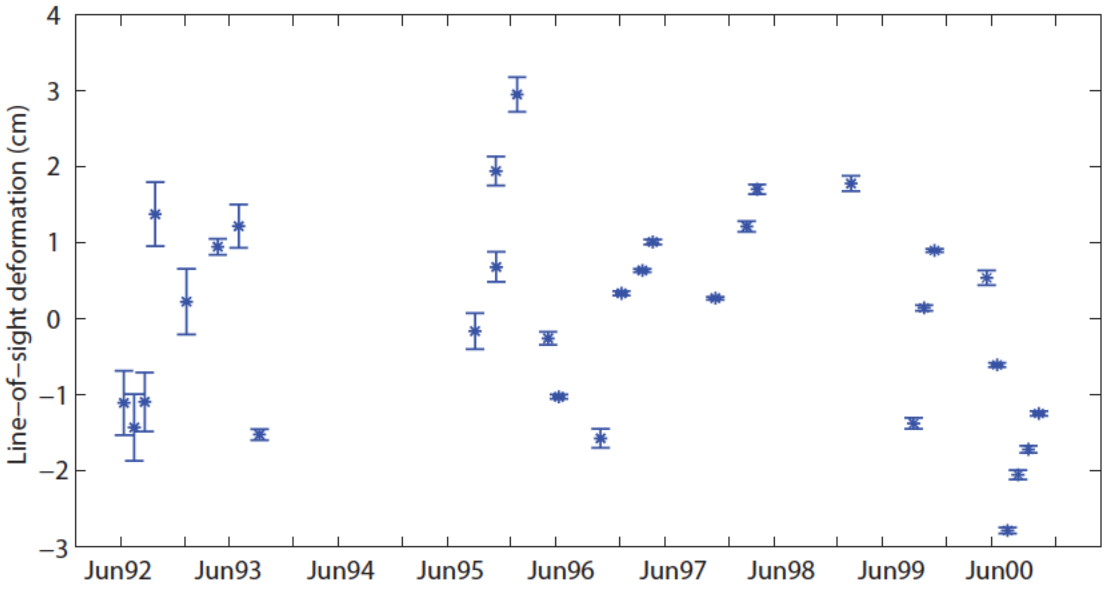

Figure 6.7. Line-of-sight (LOS) deformation relative to June 6, 1992 at a high coherence pixel near well ALA6. The standard deviation of the LOS deformation at each acquisition time is shown as error bars. The uncertainty shown here is due to decorrelation alone.

The standard deviation ranges from 0.04 to 0.5 cm. The mean standard deviation of the deformation estimates is 0.2 cm. The uncertainty in the estimate will change depending on the coherence of the pixel in each interferogram. In section 6.4 we will investigate how to formally quantify this relationship.

Figure 6.8 shows the mean standard deviation of the deformation estimate over the entire SLV. We can see that on a valley-wide scale the uncertainty in the deformation is variable. The white box in Figure 6.8 shows the area around well ALA6; we can see that the uncertainty in the deformation around well ALA6 is also variable. This is particularly important when we consider the ultimate goal of our research, which is to combine the spatially dense InSAR deformation measurements with the much more sparse hydraulic head measurements from wells to estimate hydraulic head over the entire SLV. This requires us to first understand the relationship between the hydraulic head measurements and the InSAR deformation measurements. Ideally we would compare deformation measurements from pixels in close proximity to the well to the hydraulic head at the well. The question remains, which pixels do we use to make this comparison? Based on our results here we conclude that we would need to take the uncertainty in the deformation into consideration during this comparison.

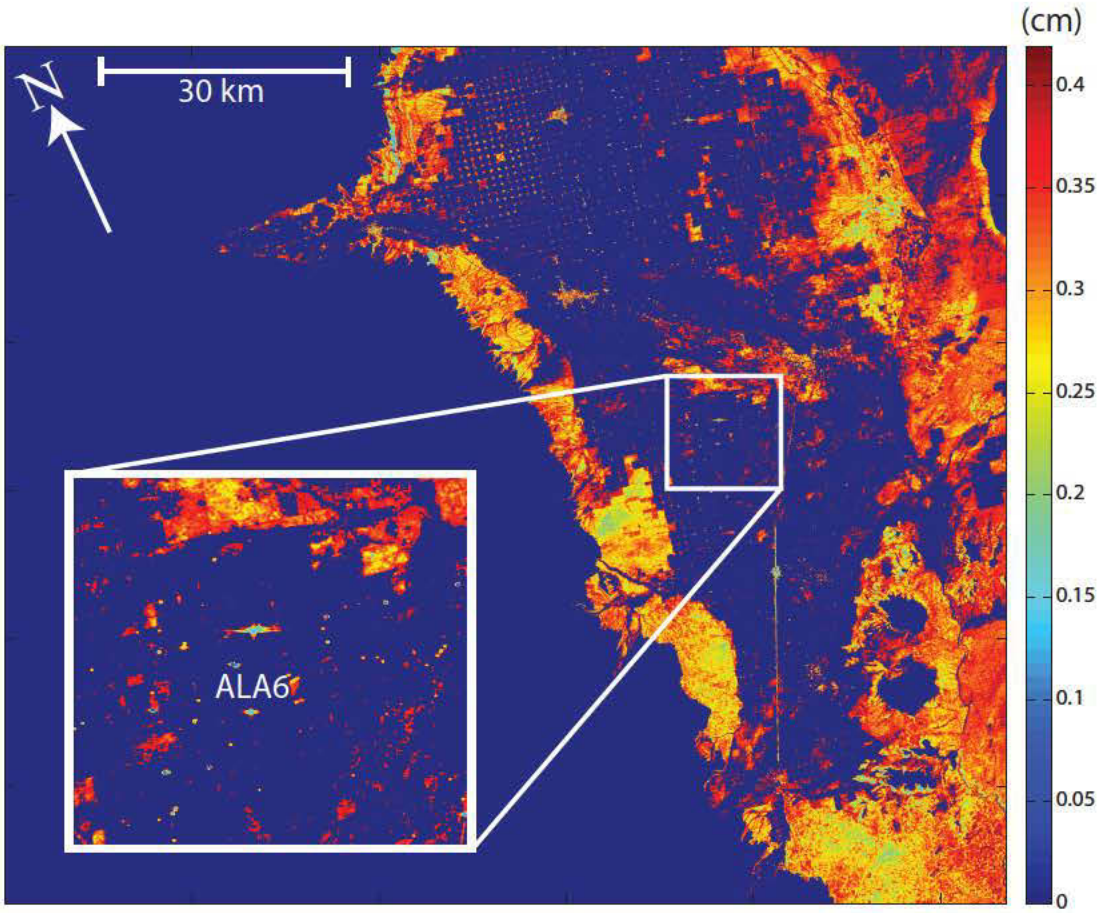

Figure 6.8: The mean standard deviation of the deformation estimate for all selected pixels in the SLV.

The most important point to note about Figure 6.7 and Figure 6.8 is that the uncertainty due to decorrelation is not very large. We know from previous research that the uncertainty due to atmospheric phase effects can often be on the order of centimeters [*Hanssen*, 2001]. The uncertainty we are estimating here is much smaller, typically 0.4 cm or less. Uncertainty due to decorrelation may not be the dominant component of uncertainty in scenes that contain a lot of atmospheric phase effects. However, because

we do not have a way to quantify how the uncertainty due to atmospheric phase effects varies spatially, the analysis presented in this section is still important.

6.4 Uncertainty and SBAS analysis thresholds

In the previous sections we removed scenes whose deformation measurements were interpreted to be corrupted with atmospheric phase effects and propagated the uncertainty due to decorrelation in the InSAR deformation measurement through the SBAS analysis processing chain. In SBAS analysis there are a number of decision points where we determine whether: a) there are enough interferograms, and b) the pixels have adequate coherence. *Berardino et al.* (2002) required that $\gamma > 0.26$ in 50% of the interferograms for a pixel to be selected for the processing. However, the selection of this threshold is ad-hoc. The coherence and the uncertainty of the deformation due to decorrelation are related, as discussed in the previous section. In this section we quantify this relationship for our version of SBAS and the dataset in the SLV.

6.4.1 Method

We study the effects of the decision points in a controlled manner by creating a synthetic data set. We let the time span of investigation be 8 years, the same time span as the hydraulic head measurements at well CON2 (1992-2000), with 30 randomly selected acquisition times. This is similar to the sampling rate for InSAR data from the ERS-1 and ERS-2 satellites in the SLV. Each scene is assigned a randomly selected orbital position. We apply the spatial and temporal baseline threshold to create a set of interferograms. We vary the spatial and temporal baseline thresholds to investigate the effect of number of

interferograms on the uncertainty of the final deformation estimates. We next assign a coherence value to each interferogram. The coherence values are drawn from a Gaussian distribution, the mean and the standard deviation of which also varied. These coherence values are used to quantify the uncertainty in the interferometric phase, which is then propagated through the SBAS analysis processing chain to determine the uncertainty in each deformation estimate.

6.4.2 Results and Discussion

Using the synthetic data described in section 6.4.1 we investigated the effects of number of interferograms, mean coherence and standard deviation of the coherence on the standard deviation of the deformation estimate. In section 6.3.3 we found that the uncertainty in the deformation estimated at each acquisition time is different. For this reason we created an aggregate variable for each pixel, the mean standard deviation of the estimated deformation, which is the mean of the standard deviation for all acquisition times.

We first investigated the relationship between the mean coherence and the mean standard deviation of the estimated deformation while varying the number of interferograms used in the SBAS analysis: 70 - 80, 80 - 100, 100 - 200 and 200 - 300. Figure 6.9 shows that the number of interferograms used in our version of SBAS analysis does not appear to greatly affect the resulting standard deviation of the deformation estimate. This implies that changing the spatial and temporal baseline thresholds to include more interferograms does not significantly decrease the uncertainty due to decorrelation. These results agree

well with our understanding of the SBAS analysis algorithm we proposed in Figure 5.6. In our version of SBAS analysis we solve for the deformation at each acquisition time rather than solving for the low-pass deformation model parameters, as described in Figure 2.6. Therefore, once we have a single small baseline subset, i.e. all the acquisitions are linked via a single interferogram, additional interferograms do not decrease the amount of uncertainty significantly. If we implemented the SBAS analysis as shown in Figure 2.6, we would find that the number of interferograms used would affect the uncertainty in the final deformation estimates.

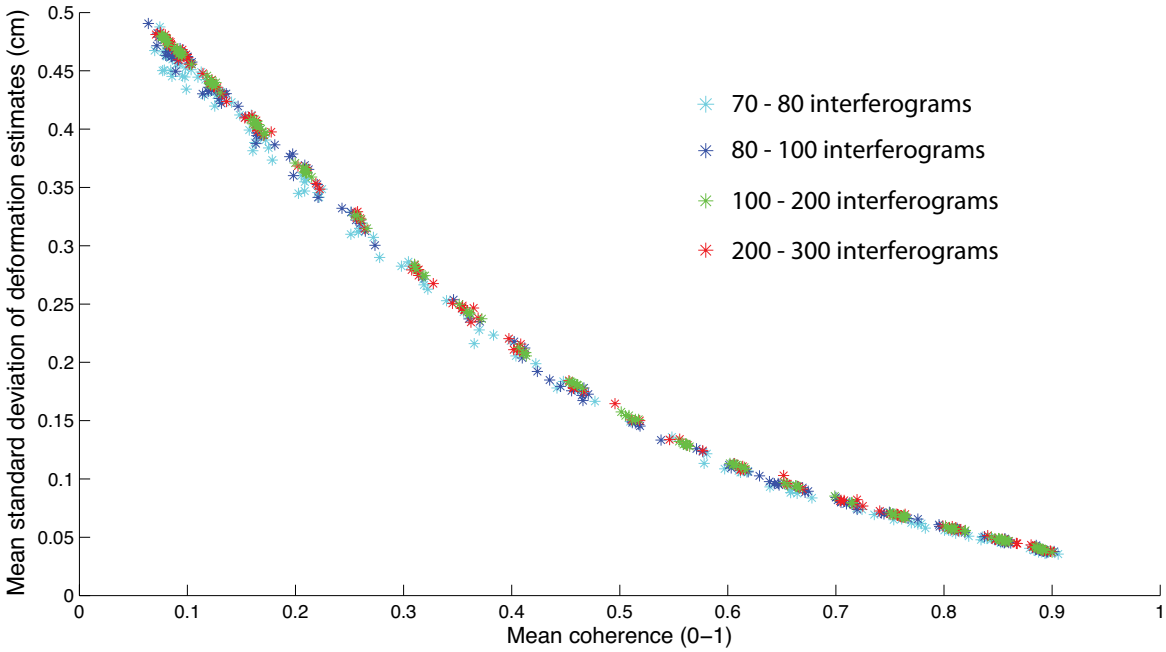

Figure 6.9: The mean standard deviation of the deformation estimates as a function of the mean coherence and the number of interferograms.

We next constrained the number of interferograms to be 100 and varied the mean coherence as well as the standard deviation of the coherence; these results are shown in

Figure 6.10. As the standard deviation of the coherence increases the standard deviation of the deformation estimates also increase. The nonlinear behavior in Figure 6.6 explains the spread in the uncertainty for a single mean coherence value. For small standard deviations of the coherence this spread is not evident. That is because over short coherence intervals the relationship in Figure 6.6 is linear.

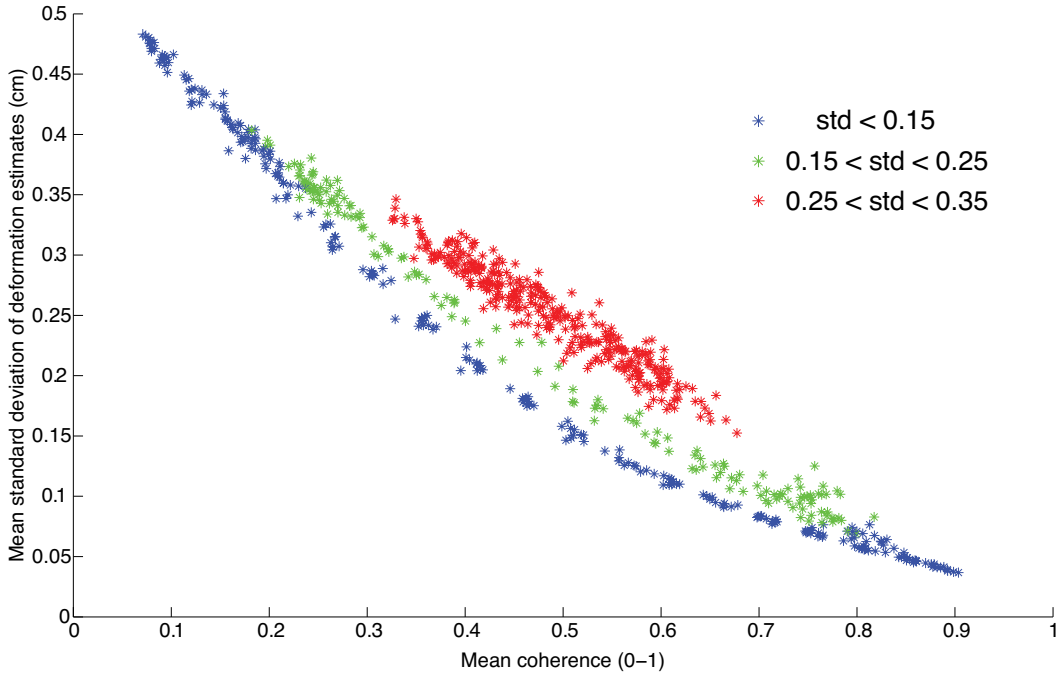

Figure 6.10: The mean standard deviation of the deformation estimates as a function of the mean coherence and the standard deviation of the coherence.

Having explored the relationship between the mean coherence and the mean standard deviation of the deformation estimates using the synthetic data set, we next determined how well the data from the SLV agree with Figure 6.10. Figure 6.11 shows the data from the SLV with the upper and lower envelopes from Figure 6.10 drawn in as solid black lines. A majority of the 1.5 million pixels in the SLV fall within the envelope defined by

our synthetic study. The SLV data that lie outside the synthetic data bounds are primarily those with distributions of coherence that are not Gaussian in nature, e.g. uniform or slightly skewed.

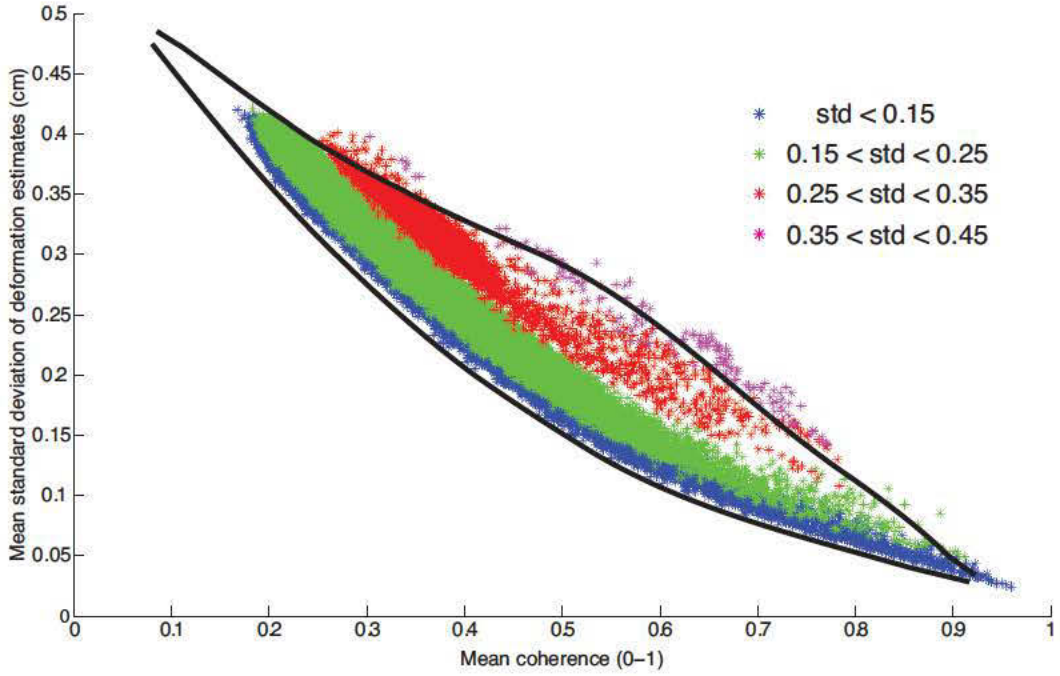

Figure 6.11: The mean standard deviation of the deformation estimates as a function of the mean coherence and the standard deviation of the coherence for the data from the SLV. The solid black lines show the upper and lower bounds defined by the synthetic data example.

Pixels are selected for SBAS processing by considering how often a given pixel is above a set coherence threshold. *Berardino et al.* (2002) required that $\gamma > 0.26$ in 50% of the interferograms. It is evident from the work presented here that both the mean coherence in all interferograms and the standard deviation of the coherence affect the uncertainty in

the deformation estimate, both in the synthetic dataset and in the data from the SLV. If there is some acceptable uncertainty in the final deformation estimates understanding this relationship will allow us to set the appropriate thresholds for SBAS analysis.

6.5 Conclusions

Addressing the uncertainty of InSAR-measured deformation is critical if these data are to be used for groundwater applications as a basis for management decisions. In the work presented in Chapter 6 we investigated the efficacy of a novel algorithm that uses supplementary hydrologic data to identify scenes whose phase measurements may have been corrupted with atmospheric phase effects. We also quantified the uncertainty in the InSAR deformation measurement due to decorrelation of radar signals.

When InSAR deformation measurements are being used for a specific application, we have shown how to set SBAS analysis thresholds in order to achieve an acceptable level of uncertainty (section 6.4). More specifically, we determined that the number of interferograms does not have a large effect on the uncertainty of the InSAR deformation measurements for our version of SBAS analysis used on the data from the SLV. This means that if researchers are evaluating possible study areas to apply our version of SBAS analysis they should consider that the number of interferograms available would not greatly affect the uncertainty in their final results. We also quantified the relationship between the mean coherence, the standard deviation of the coherence and the standard deviation of the estimated deformation. For example, if the mean coherence of a pixel is 0.5 and the standard deviation of the mean coherence is 0.25 then the uncertainty in the

deformation estimate will be somewhere between 0.21 cm – 0.27 cm. These results will allow researchers to estimate the uncertainty of a dataset before performing all of the SBAS analysis processing steps.

In section 6.3 we showed how to propagate the uncertainty due to decorrelation through the InSAR processing chain. We now have an estimate of the uncertainty in the deformation on a pixel-by-pixel basis. In future work, when we are comparing the deformation and hydraulic head datasets, we will be able to compare the two based on a) the distance from the deformation measurement to the well and b) the uncertainty in the deformation measurement. Although it was important that we investigate how the uncertainty due to decorrelation varies spatially, we determined that this component is small compared to the possible uncertainty due to atmospheric phase effects.

Given the possible magnitude of the uncertainty due to atmospheric phase effects we needed a practical solution for our specific application. In section 6.2 we showed that the algorithm developed to identify pixels affected by atmospheric phase effects works well with synthetic data. However, a tradeoff exists between data quality and data sampling when being applied to real datasets. We were not able to directly evaluate the performance of our algorithm because no other deformation measurements have been made in the SLV during this time period.

We note that our algorithm for reducing atmospheric effects can be modified and applied to aquifer systems that contain producing clay sediments. In our analysis we considered

only a linear relationship between the hydraulic head and the deformation. However, if the hydraulic head change in the aquifer system caused changes in hydraulic head in underlying or overlying units that contain clay, there would be some delay between the change in hydraulic head and the deformation. In order to overcome this issue one would first identify the periodicity of the two datasets, to determine if there is a delay. If so, one would need to correct for it before applying our algorithm.

The algorithm as presented here is limited by the fact that we can only apply it to the deformation time-series at pixels around the well where we have hydraulic head measurements. However, because our algorithm only requires trends in the hydrologic data we can use pumping data instead of, or in addition to, the hydraulic head measurements. Pumping rates can indicate times of year that the ground surface should be moving downward. This is especially important, as hydraulic head measurements are often not reported to groundwater management agencies, while the reporting of well pumping rates is becoming more common.

In Chapter 6 we showed the value of quantifying the spatially variable uncertainty in the InSAR deformation measurements if these data are to be applied to groundwater problems. In the chapter to follow we will use these uncertainty estimates to better understand the relationship between deformation and hydraulic head across the entire SLV.

Chapter 7
Improved estimates of hydraulic head

7.1 Introduction

In this chapter we explore ways in which the relationship between InSAR measured deformation and measurements of hydraulic head can be utilized to increase the spatial and temporal density of hydraulic head measurements in the confined aquifer system of the San Luis Valley (SLV), Colorado. In Chapter 5 the relationship between the InSAR measured deformation and hydraulic head was investigated at three well locations. We found that the two datasets showed similar seasonality. The hydraulic head values, derived from InSAR measured deformation and skeletal elastic storage estimates from nearby aquifer tests, agreed with measured hydraulic head values 67% of the time. However, the uncertainty in the InSAR derived values was on the order of meters, which is too large for these values to be useful for groundwater applications. The uncertainty is caused by uncertainty in the InSAR deformation measurements and the skeletal elastic storage estimates. This led to the work in Chapter 6 where the uncertainty in the

deformation measurement was better quantified. It is beyond the scope of this thesis to quantify the uncertainty in the skeletal elastic storage coefficients as measured during aquifer tests. Thus, in this chapter we will focus on the relationship between the InSAR measured deformation data and hydraulic head data and investigate ways that the deformation data can be used to interpolate and extrapolate hydraulic head measurements in time and space.

As discussed in Chapter 4 we are limited to investigating the relationship between deformation and hydraulic head at 11 well locations. In previous work in arid/urban areas the deformation measurements were collocated with hydraulic head measurements at wells [*Hoffman et al., 2001; Schmidt and Burgmann, 2003; Wisely and Schmidt, 2010*]. However, no such studies have been conducted in an agricultural area like the SLV, where high quality InSAR measurements are not made at all pixels and the uncertainty in the measurement changes from pixel to pixel around the well (see Figure 7.1). Therefore, it might not be the case that hydraulic head measurements are collocated with high quality InSAR deformation measurements. One solution to this mismatch in position is to use the deformation measurement closest to the well location, and another solution is to use a nearby deformation measurement with the smallest uncertainty. In section 7.2 of this chapter we investigate how the distance from the well to the deformation pixel and the uncertainty in the deformation affect the relationship between the deformation and the hydraulic head.

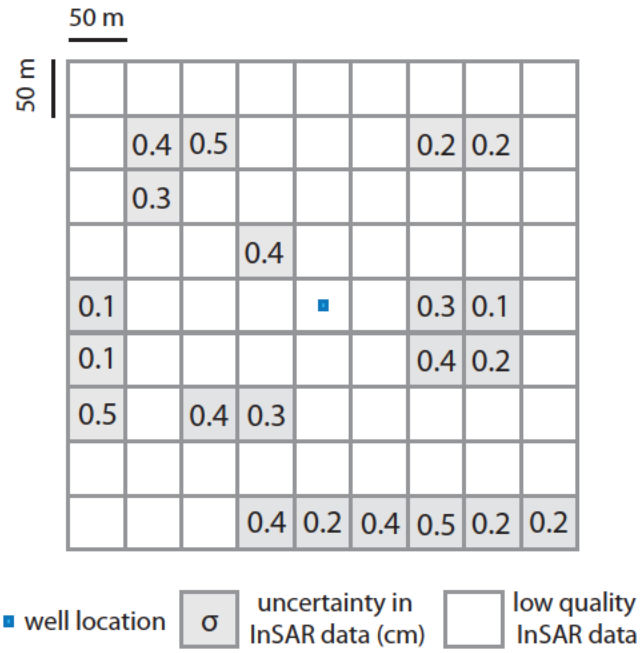

Figure 7.1: A schematic showing how the uncertainty in the InSAR deformation data varies spatially in vegetated areas of the SLV (where σ is the standard deviation of the deformation measurement).

The results of section 7.2 showed that the spatial structure of the deformation is relevant when investigating the relationship between the deformation and hydraulic head measurements. The next major question of interest is: how is the spatial structure of the deformation dataset related to the spatial structure of the hydraulic head data set? If the two datasets are indeed linearly related via elastic deformation theory (equation 2.26) then similar spatial structures should be evident in both datasets. In section 7.3 we quantify the spatial structure of the two datasets using semi-variograms. Based on the spatial structure of the deformation dataset we use another type of geostatistical analysis, simple kriging, to estimate the deformation at all confined aquifer well locations in the SLV (section 7.4). A schematic of the kriged deformation dataset is shown in Figure 7.2.

The blue pixels show where deformation has been estimated using simple kriging. With an estimate of the deformation collocated with the hydraulic head measurements, we can proceed to investigate the relationship between the deformation and hydraulic head at all 11 confined aquifer well locations.

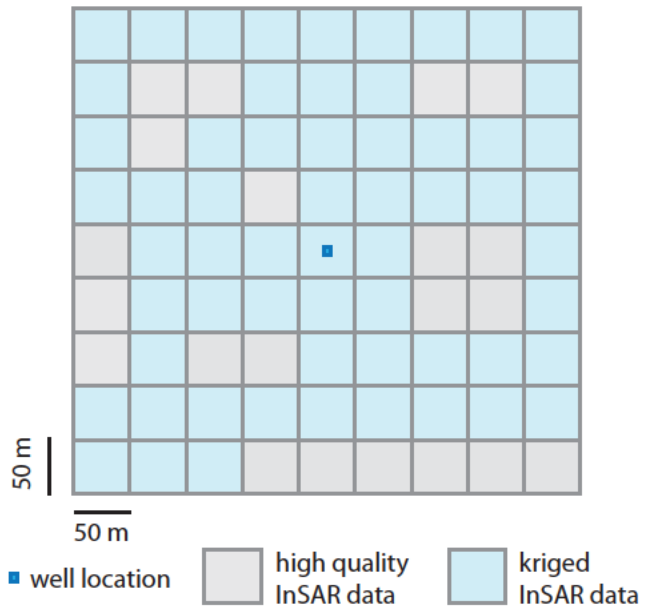

Figure 7.2: A schematic of the InSAR deformation dataset showing the high quality data as well as the kriged deformation estimates.

In section 7.4 we investigate the relationship between hydraulic head and deformation at all 11 well locations by performing a regression analysis. We discuss the quality of the linear relationship found based on the predicted amount of deformation from section 4.2. We then use the skeletal elastic storage coefficient (S_{ke}), the parameter that relates the deformation and hydraulic head, to predict hydraulic head values during times when no hydraulic head measurements were made. The work presented in this section is especially

relevant for agricultural areas where temporal gaps in hydraulic head time series can be estimated using InSAR deformation data.

We begin this chapter by investigating the relationship between the hydraulic head and the deformation for a number of pixels around specific well locations (Section 7.2). This works leads to the comparison of the spatial structures of the deformation dataset and the hydraulic head dataset (Section 7.3). Once we understand how the deformation dataset varies spatially we use simple kriging to estimate the deformation directly at confined aquifer well locations. This allows us to determine the relationship between the hydraulic head measurements and deformation measurements at the well locations and predict hydraulic head back in time using the estimates of S_{ke} (section 7.4).

7.2 The relationship between head and deformation around three wells

The first step towards understanding the relationship between InSAR deformation measurements and hydraulic head measurements is to investigate how this relationship varies from pixel to pixel around a single well (see Figure 7.1). In this section we compare the deformation and head datasets at three well locations: ALA6, ALA7 and ALA8. These wells were selected for this initial analysis because they are all located within the large subsidence bowl observed in a number of the raw interferograms. This large visible deformation signal is indicative of an area with a large signal to noise ratio. The deformation data used in this chapter is the same high quality dataset (see section 3.4) used in Chapters 5 and 6, with 31 SAR acquisitions from 1992 – 2000.

The work in this section assumes, a) all the deformation measured at the surface (Δd) is indeed caused by aquifer compaction (Δb), i.e. $\Delta b = \Delta d$ in equation 2.26, b) only elastic deformation is occurring, i.e. no clay drainage is occurring within the confined aquifer system or from the overlying confining unit. Given these assumptions the two datasets are linearly related through the skeletal elastic storage coefficient (S_{ke}). The main question of this section is, how does this linear relationship change for deformation measurements made around a well? The section to follow describes the linear regression analysis used to quantitatively assess this relationship.

7.2.1 Linear regression analysis

The linear regression analysis of the deformation and hydraulic head data takes into account the changing uncertainty in the deformation measurements as determined in Chapter 6 [*York et al., 2004*]. The uncertainty in the hydraulic head measurements is estimated to be +/- 10 cm [*Eric Harmon personal communication,* 2012]. The slope of the linear best fit, between the Δh and Δd, provides an estimate of the elastic skeletal storage coefficient (S_{ke}) at each pixel location within 1 km of the well. The goodness of fit is evaluated at each pixel location by calculating the coefficient of determination (R^2) using the following set of equations:

$$\begin{aligned} SS_{tot} &= \sum_i \left(y_i - \bar{y}\right)^2 \\ SS_{err} &= \sum_i \left(y_i - \hat{y}\right)^2 \quad , \\ R^2 &\equiv 1 - \frac{SS_{err}}{SS_{tot}} \end{aligned} \tag{7.1}$$

where y is the dependent variable (the deformation as measured by InSAR), $\bar{y}$ is the mean value of the dependent variable and $\hat{y}$ is the estimated value of the dependent variable given the regression parameters. SS_{tot} is the total sum of squares and SS_{err} is the residual sum of squares. In the sections to follow we will investigate first how the estimate of S_{ke} varies spatially around the wells, and then how the average uncertainty in the InSAR deformation measurement affects the goodness of fit between deformation and hydraulic head.

7.2.2 Variability of S_{ke} around wells: ALA6, ALA7 and ALA8

Figure 7.3 shows the spatial distribution of S_{ke} estimates around the wells at the locations of the high quality deformation measurements. The spatial patterns seen Figure 7.3 are solely a product of the location of the high quality deformation measurements as determined in section 5.4. The axes of latitude and longitude in each plot have slightly different scales, and it should be noted that neighboring pixels are approximately 50 m apart. S_{ke} varies from 0.0034 – 0.0086, which are reasonable values for the sediments found in the aquifer system in the SLV. We can see that S_{ke} is more variable around well ALA7 (0.0057 – 0.0085), than around ALA6 (0.0031 – 0.0047) and ALA8 (0.0055 – 0.0068).

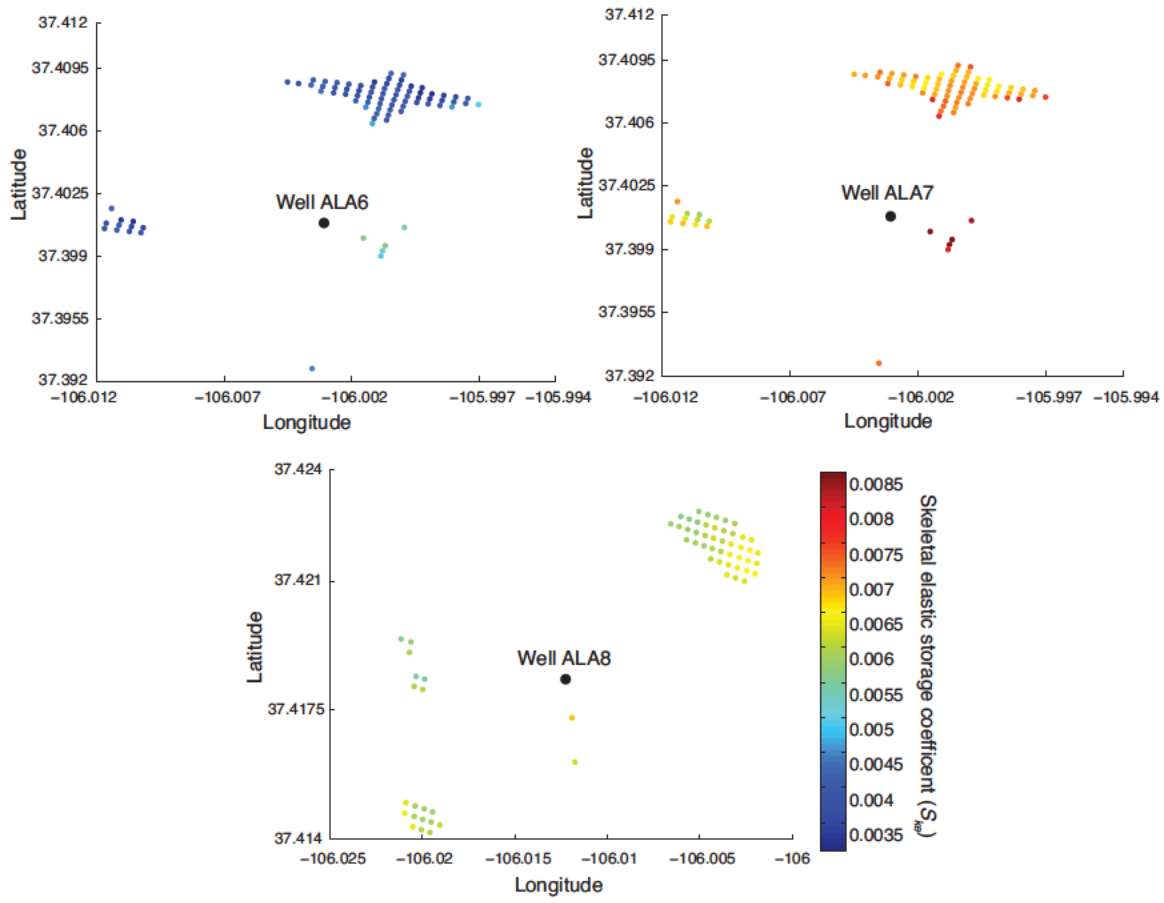

Figure 7.3: The spatial distribution of S_{ke} estimates around wells ALA6, ALA7 and ALA8.

If any combination of the following properties change around the well locations then the deformation will vary: 1) S_{ske} for the producing portion of the aquifer, 2) the thickness of the producing portion of the aquifer (b^*), 3) the uncertainty in the deformation data, or 4) the hydraulic head. No additional information is available for S_{ske}, b^*, and Δh around the wells, hence it is difficult to determine which of these parameters is truly causing the changes in the deformation measurements. We investigated the relationship between the average uncertainty of the deformation estimates (as determined in Chapter 6) and the estimated S_{ke} values, but no meaningful trend could be seen in these data alone.

7.2.3 Average uncertainty in the InSAR deformation measurements and R^2

In this section we investigate how the average uncertainty of the deformation estimates (as estimated in Chapter 6) affect the linear relationship between the InSAR measured deformation and hydraulic head. The goodness of fit parameter (R^2) was used to quantify the linearity of the relationship. The left plot in Figure 7.4 shows R^2 as a function of distance from the pixel to well ALA6, and the right hand plot shows a plan view of the pixels around well ALA6. The colors define the average uncertainty of the deformation estimates at a given pixel, where red is low uncertainty and blue is high uncertainty. It is clear that at this well location the pixels closest to the well provide the best fit between the deformation data and the hydraulic head data, regardless of the uncertainty in the deformation measurements. However, no simple relationship can be drawn from the plots in Figures 7.4 to link R^2 with the average uncertainty of the deformation measurements.

Figure 7.5 shows the same plots for well ALA7. However, at this well location the regression of Δh and Δd at the pixels closest to the well do not produce the highest R^2 values. In fact, 90% of the regressions around well ALA7 produce R^2 values between 0.8 and 0.86. At this well location the pixels proximity to the well does not appear to systematically affect the linear relationship between Δh and Δd, contrary to what was observed at well ALA6. Similarly to ALA6, no simple relationship can be drawn between the distance from the pixel to the well, the uncertainty and R^2 (see Figure 7.5).

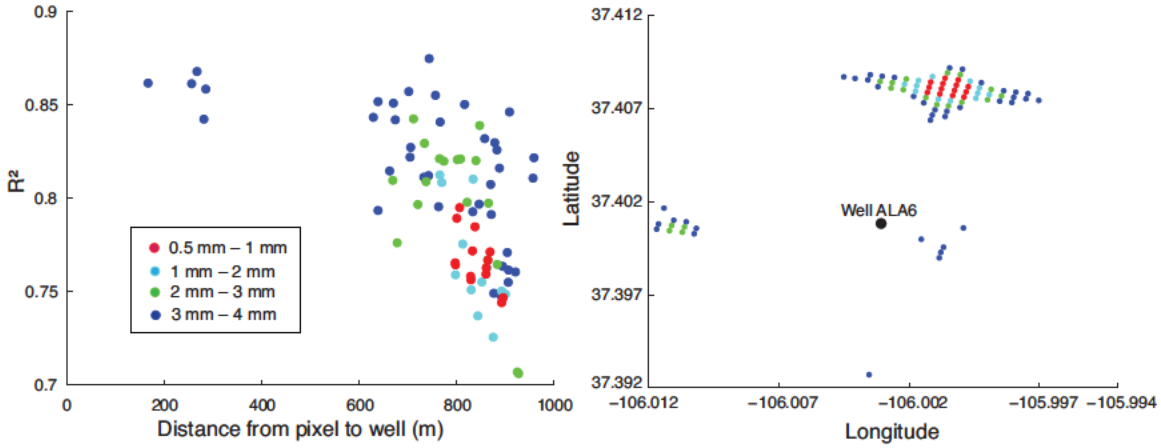

Figure 7.4: Left plot: R^2 as a function of the distance from the pixel to the well ALA6. Colors based on the average uncertainty in the deformation: Red = 0.5 mm – 1 mm, Light blue = 1 mm – 2 mm, Green = 2 mm – 3 mm, Blue = 3 mm – 4 mm. Right plot: a plan view of the pixels and the associated average uncertainty of the deformation measurements.

The left hand plots of Figures 7.4 and 7.5 show a group of observations with low average uncertainty in the deformation measurements (red markers) that exhibit similar R^2 values. The right hand plots of Figures 7.4 and 7.5 shows that these pixels are all located close to each other (~ 37.409 N 106.001 E). The similar R^2 values for these pixel locations may be caused by a combination of two things: a) the uncertainty values are similar, as shown the left hand plots in Figures 7.4 and 7.5, or b) the pixels are close to each other spatially, as shown in the right hand plots in Figure 7.4 and 7.5, and hence are in an area with homogeneous hydrogeologic properties.

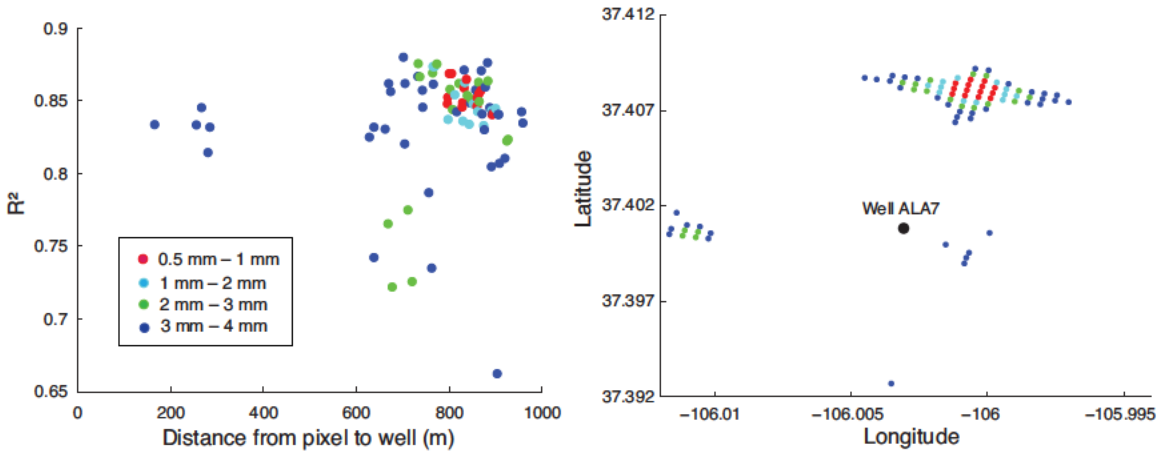

Figure 7.5: Left plot: R^2 as a function of the distance from the pixel to the well ALA7. Colors based on the average uncertainty in the deformation: Red = 0.5 mm – 1 mm, Light blue = 1 mm – 2 mm, Green = 2 mm – 3 mm, Blue = 3 mm – 4 mm. Right plot: a plan view of the pixels and the associated average uncertainty of the deformation measurements.

Figure 7.6 shows slightly different results for well ALA8. At this well location the pixels with the lowest average uncertainty in the deformation measurements produced the highest R^2 values. Similar to ALA6 there is a larger spread in the R^2 values. And, once again no simple relationship can be drawn between the distance from the pixel to the well, the uncertainty and R^2 (see Figure 7.6).

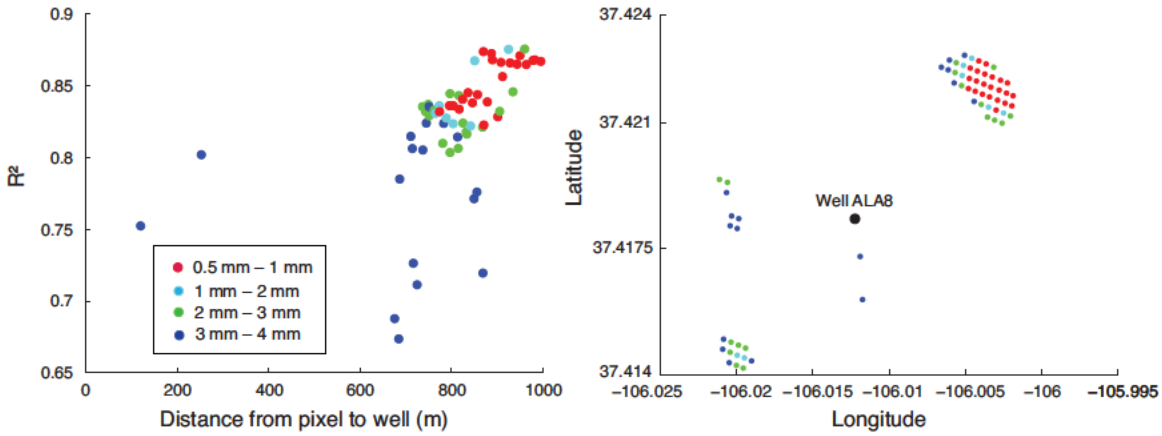

Figure 7.6: R^2 plotted as a function of the distance from the pixel to the well ALA8. Colors based on the average uncertainty in the deformation: Red = 0.5 mm – 1 mm, Light blue = 1 mm – 2 mm, Green = 2 mm – 3 mm, Blue = 3 mm – 4 mm.

Based on the results from this section and section 7.2.2 we can see that the relationship between the hydraulic head measurements made at these three wells and the deformation measurements made at the pixels around the wells is highly variable, even within 1 km of the well location. In the section to follow we investigate the spatial variability of the deformation and hydraulic head datasets.

7.3 Spatial analysis of deformation data and hydraulic head data

In this section we use a geostatistical function called the semi-variogram in order to quantify the spatial structure of the two datasets. The section begins by providing the theoretical background for variogram analysis from a geostatistical perspective. We then use the Stanford Geostatistical Modeling Software (SGeMS) to calculate the semi-variograms for the deformation data at each time step. We then compare a single

deformation semi-variogram to the hydraulic head semi-variogram from the same time period in order to investigate the spatial similarities of the two datasets.

7.3.1 Geostatistical definition of the variogram

The main geostatistical calculation that we use in this section is known as the semi-variogram (γ). For some random variable *z* at some spatial location *u*, the semi-variogram is an average of the squared differences of the variable at location *u* to location *u* plus some lag vector *h*. If we calculate the semi-variogram for all lag distances then we have the following formula:

$$\gamma(h) = \frac{1}{2N}\sum_{i=1}^{N}\left[z(u_i + h) - z(u_i)\right]^2, \tag{7.2}$$

where N is the number of measurement pairs with a given lag distance h. The semi-variogram is a measure of the average dissimilarity of a random variable at specific lag distances. It is important to note that this definition is appropriate when the data are equally spaced. However, when the data are irregularly spaced or sparse, it becomes important to include what is known as a lag tolerance. This means that lag distances plus or minus the tolerance are averaged together. If the direction of the lag vector is not considered in the calculation then the semi-variogram is called omni-directional.

If some anisotropy is expected in the spatial data then directional semi-variograms should be calculated. For practical purposes directional variograms are usually calculated with

some angular tolerance for the lag vector. If the directional variogram is calculated for all angles from 0 – 180 degrees then we can create what is known as a 2D variogram map. The directional variograms are plotted on a color scale along the angle of the lag vector. The variability in the color for a set lag distance across all angles can highlight important anisotropic spatial structures.

When analyzing semi-variograms it is often useful to fit the different structures in the semi-variogram with different models. In doing so, semi-variograms can be compared quantitatively. In the work completed in the following section we either use an exponential model or a linear model to characterize the different structures observed. The exponential model has the following form:

$$\gamma(h) = (c \times (1 - \exp\left(\frac{-h}{a}\right))) + n \quad , \tag{7.3}$$

and is characterized by the sill (c), the range (a), and the nugget (n). Figure 7.7 shows a schematic of an exponential semi-variogram model. For longer lag distances the exponential semi-variogram model levels out, the semi-variogram value where this occurs is called the sill. The lag distance where the semi-variogram model reaches 95% of the sill value is known as the range. The range describes the scale at which the two measurements of the variable become practically uncorrelated and provides an intrinsic correlation length. Theoretically the semi-variogram value at the origin should be zero. But, because of random observation error and variability below the sampling scale of the

measurement (microvariability) it is often found that the semi-variogram value closest to the origin is non-zero; this is known as the nugget.

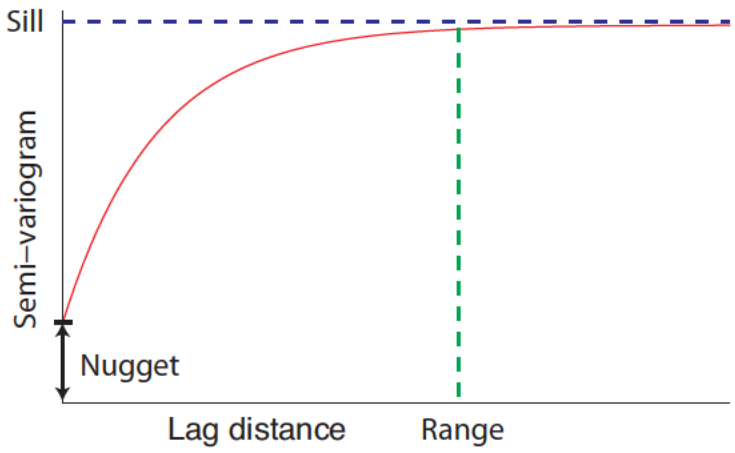

Figure 7.7: A schematic of a semi-variogram model.

If the semi-variogram does not stabilize around a sill value, but continues to increase with lag distance a linear model is used to fit the spatial structure. The linear model only requires two parameters for characterization: a nugget and a slope. Because the semi-variogram value continues to increase with lag distance the random variable in question is considered to be non-stationary, i.e. the random variable does not have some intrinsic correlation length.

For the discussion in the section to follow it is important to note that there are two important structural components of the semi-variogram:

1) The presence of variability at the scale of the sampling length, i.e. the behavior of the semi-variogram near the origin.

2) The presence of variability at a scale comparable to the sampling domain, i.e. the behavior of the semi-variogram at farther distances.

The behavior of the semi-variogram at shorter lag distances is of most interest to us in our application, as we are interested in how the deformation is changing directly around the well locations. However, in the section to follow we will also comment on the structure of the variogram for longer lag distances. It is also important to note that these structures can be nested within one another making it extremely difficult to differentiate. In the section to follow the omni-directional semi-variograms and the 2D variogram maps are calculated for each InSAR acquisition time step in order to investigate the spatial structure of the deformation dataset.

7.3.2 Semi-variogram analysis of Δd

We investigated the spatial variability of the InSAR deformation data (*Δd*) by calculating the semi-variogram using the Stanford Geostatistical Modeling Software (SGeMS) package. However, this software cannot compute the semi-variogram for more than 50,000 deformation measurements, which is only 3% of all the pixels in an SLV SAR scene. To overcome this issue we used 50,000 randomly selected deformation measurements to compute the semi-variogram for ten different subsets of the data. We found that the overall shape of the semi-variogram was the same for each subset.

The omni-directional semi-variogram for the deformation from June 19, 2000 – July 24, 2000 is shown in Figure 7.8. The lag separation selected was 50 m, as that is the

approximate distance between pixel centers. To accommodate variability in the distance between pixel centers a tolerance of 5 m was included in the calculation. The semi-variogram value at the first lag calculation is not at the origin; this indicates that the data either contain some microvariability or significant uncertainty. The semi-variogram shows a nested structure: for lag distances up to 1850 m the data appear to fit an exponential model (shown as a red line), and for lag distances greater than 1850 m the semi-variogram shows a linear structure. The short length scale structure is particularly important as it helps us understand how the deformation is varying around specific well locations. If we assume that the deformation and the change in hydraulic head are linearly related then on average the changes in hydraulic head that are more than ~ 2 km apart are also not spatially related to one another.

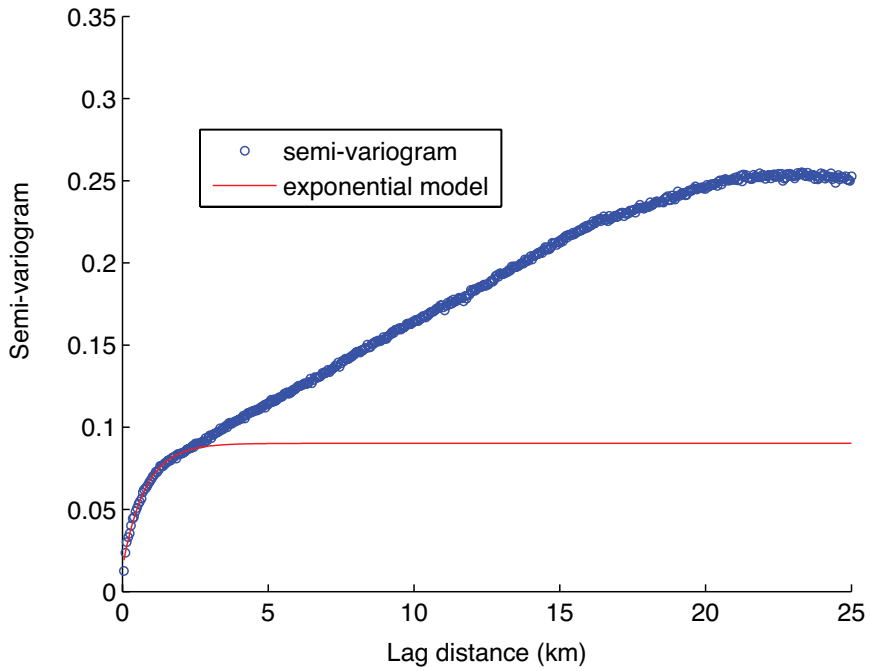

Figure 7.8: Experimental variogram for lag spacing 50 m, and tolerance 5 m. The red line shows a schematic of an exponential variogram model.

This result in itself has large implications for the way that the hydraulic head data are being used in the SLV. As discussed in Chapter 1 the Rio Grande Decision Support System (RGDSS) uses a MODFLOW groundwater flow model to predict hydraulic head change given certain pumping and recharge conditions for the confined aquifer system. However there are not sufficient observations of hydraulic head for the model to properly calibrate. In the model the confined aquifer system is made up of three hydrogeologic layers that are designed as continuous layers with specific boundary conditions set by estimated recharge rates around the rim of the SLV. Given the continuous layer model one expects the changes in hydraulic head to be related over large distances, whereas here the deformation data infer that the changes in hydraulic head are not related over large distances.

Another important note to make about the semi-variogram of the deformation data in Figure 7.8, is that the deformation data may still contain a large amount of uncertainty due to atmospheric phase effects. We are not able to ameliorate this uncertainty, as in many other studies implementing SBAS analysis, because of the nature of the hydraulic head time-series in the SLV (see Figure 5.5 in Section 5.5). Because we observe a nested structure in the semi-variogram in Figure 7.8, it may be possible that one of those structures is caused by the deformation and the other is caused by the uncertainty due to atmospheric phase effects. Note that the variogram is often referred to as a structure function in this field of study. Theoretical studies have estimated the shape of the structure function based on specific atmospheric parameters for sites in the mid-latitudes

[*Treuhaft and Lanyi*, 1987]. However the shape of these structure functions is not similar to the short length scale structure, i.e. the structure fit with the exponential model, observed in the semi-variogram in Figure 7.8.

Others have calculated the structure functions for interferograms that were made from scenes acquired only one day apart, also called tandem acquisitions [*Hanssen*, 2001; *Knospe and Jonsson*, 2010]. By looking at tandem acquisitions where no deformation was occurring the authors were able to isolate the signal due to atmospheric phase effects. The structure functions calculated by *Hanssen* (2001) were for longer length scales (> 7 km) and do not exhibit the same structure as that observed in Figure 7.8. Two semi-variograms were calculated by *Knospe and Jonsson* (2010) for tandem interferograms acquired over Marseille, France. Both show a similar structure to the exponential model fit from Figure 7.8 with some oscillations for lag distances beyond the sill. Because we have no way of determining how much of the short length scale variogram structure is due to atmospheric phase effects, and how much is due to the deformation we will not attempt to separate the two components at present.

Figure 7.9 shows the 2D variogram map for the same time step: June 19, 2000 – July 24, 2000. Lag distances up to approximately 8 km show isotropic conditions. This means that for the distances we are interested in, i.e. close to the well locations, the omni-directional semi-variogram will suffice for further analysis. However, we can see that when the lag distance increases beyond 12 km more substantial anisotropy is observed. The most

evident area is in the northwest sector where the data appear to have significantly longer correlation lengths.

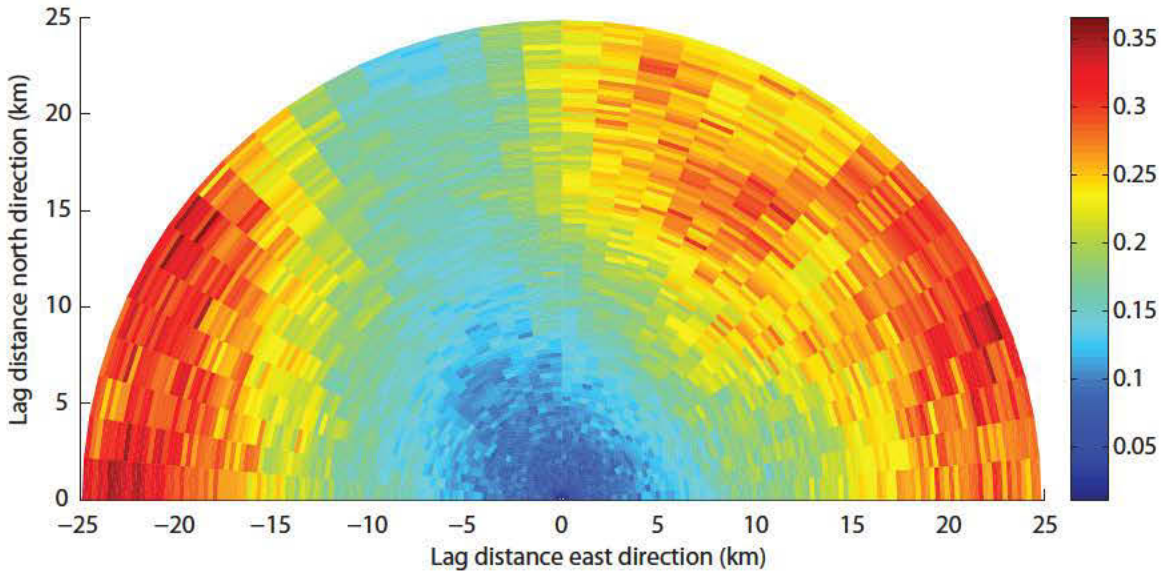

Figure 7.9: 2D variogram map of the deformation data from the time step June 19, 2000 – July 24, 2000.

Next we investigated how the spatial structure of the omni-directional semi-variogram changes through time. Because we were most interested in the deformation that occurred at shorter length scales we applied a least squares fit to the semi-variogram data for the short length scale portion of data (lags up to approximately 2 km). We used both exponential and linear models in this analysis. Initially we attempted to fit all of the variograms with exponential models for short lag distances (approximately 2 km) but found a number of the variograms showed a linear structure at that scale. The number of observations per lag distance was used to weight the least squares fit, so that a lag distance with more observations affected the fit more than lag distances with less

observations. The semi-variograms for all the acquisition times are shown in Figures 7.10 – 7.13.

The structure of these variograms changes significantly from one acquisition time to the next. We fit four of the variograms with linear models, and 26 with exponential models. The exponential models show a lot of variability in the best-fit parameters. The mean range for the variograms fit with an exponential model was 3.9 km, with a standard deviation of 2.5 km. This implies that the deformation estimates vary spatially on a number of different length scales, which is dependent on the surface deformation and the atmospheric conditions at that acquisition time. The mean nugget equals 0.0253, with a standard deviation of 0.0221. This indicates that a lot of variability exists in either: a) the microvariability of the data, or b) the uncertainty from one acquisition time to the next. Since we have already observed that the uncertainty in the deformation data changes from one acquisition time to the next due to changes in coherence (see Chapter 5), this is the most likely source for the variability in the size of the nugget. In the next section we proceed with an analysis of the spatial variability of the hydraulic head data.

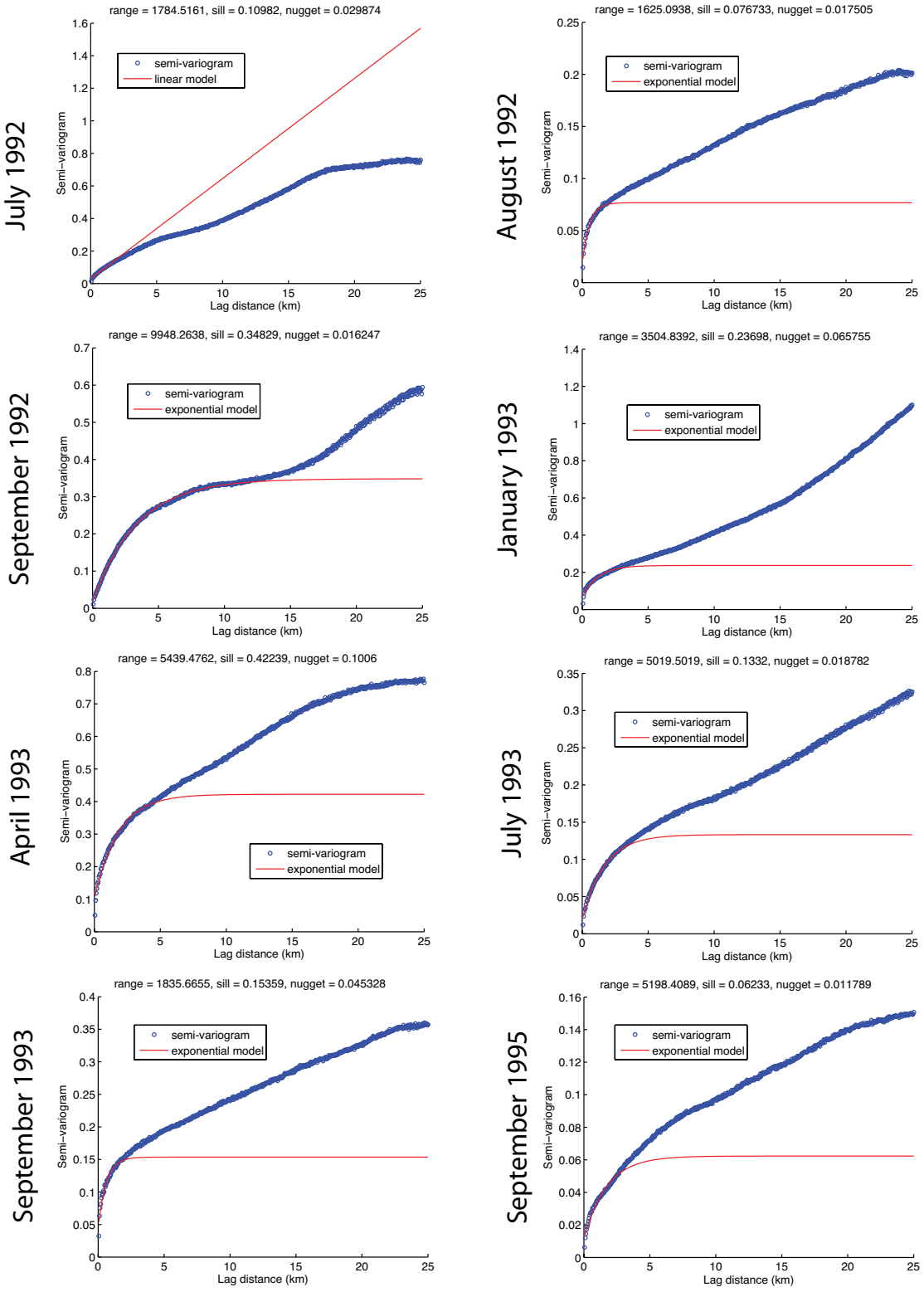

Figure 7.10: Semi-variograms and models for deformation acquisition times July 1992 – September 1995.

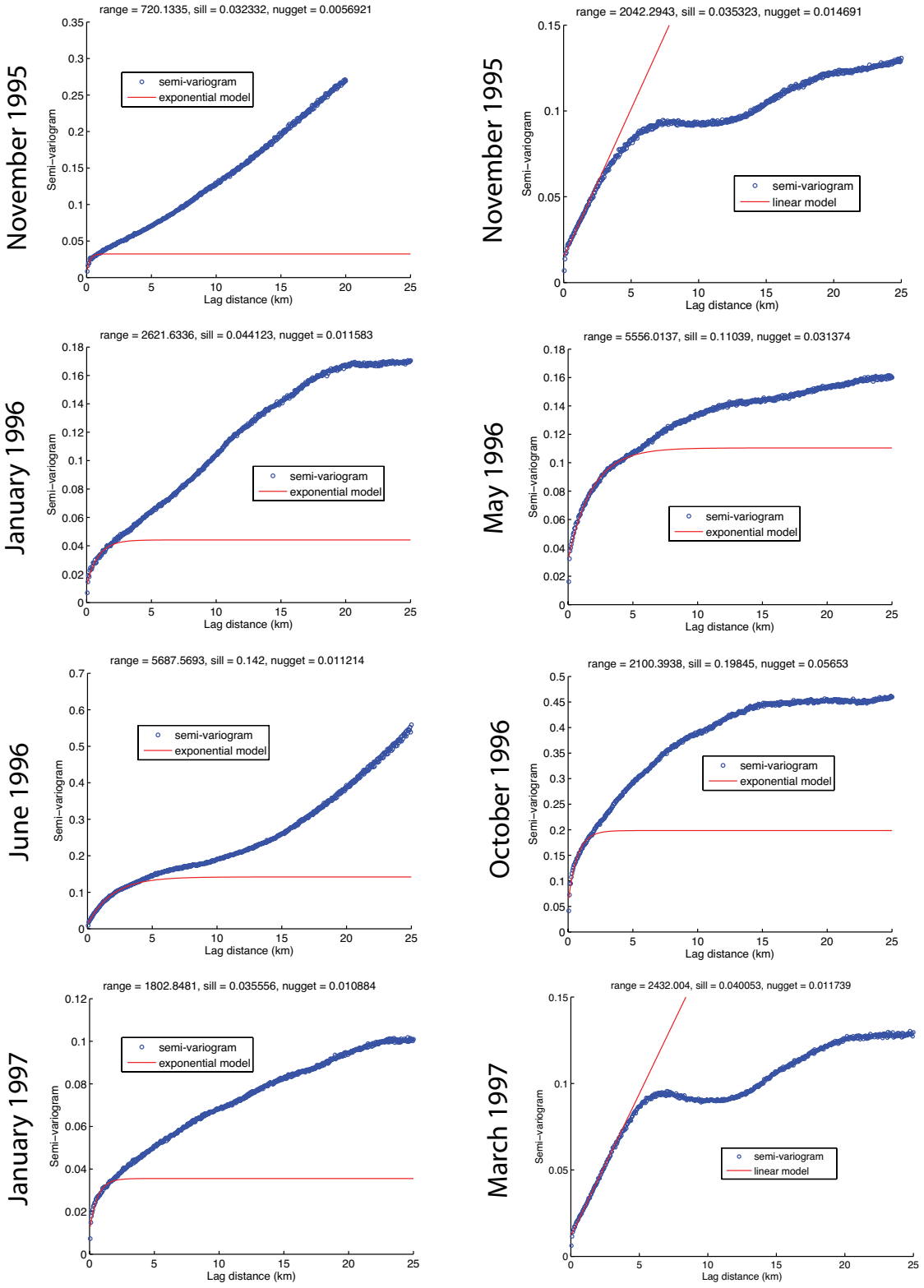

Figure 7.11: Semi-variograms and models for deformation acquisition times November 1995 – March 1997

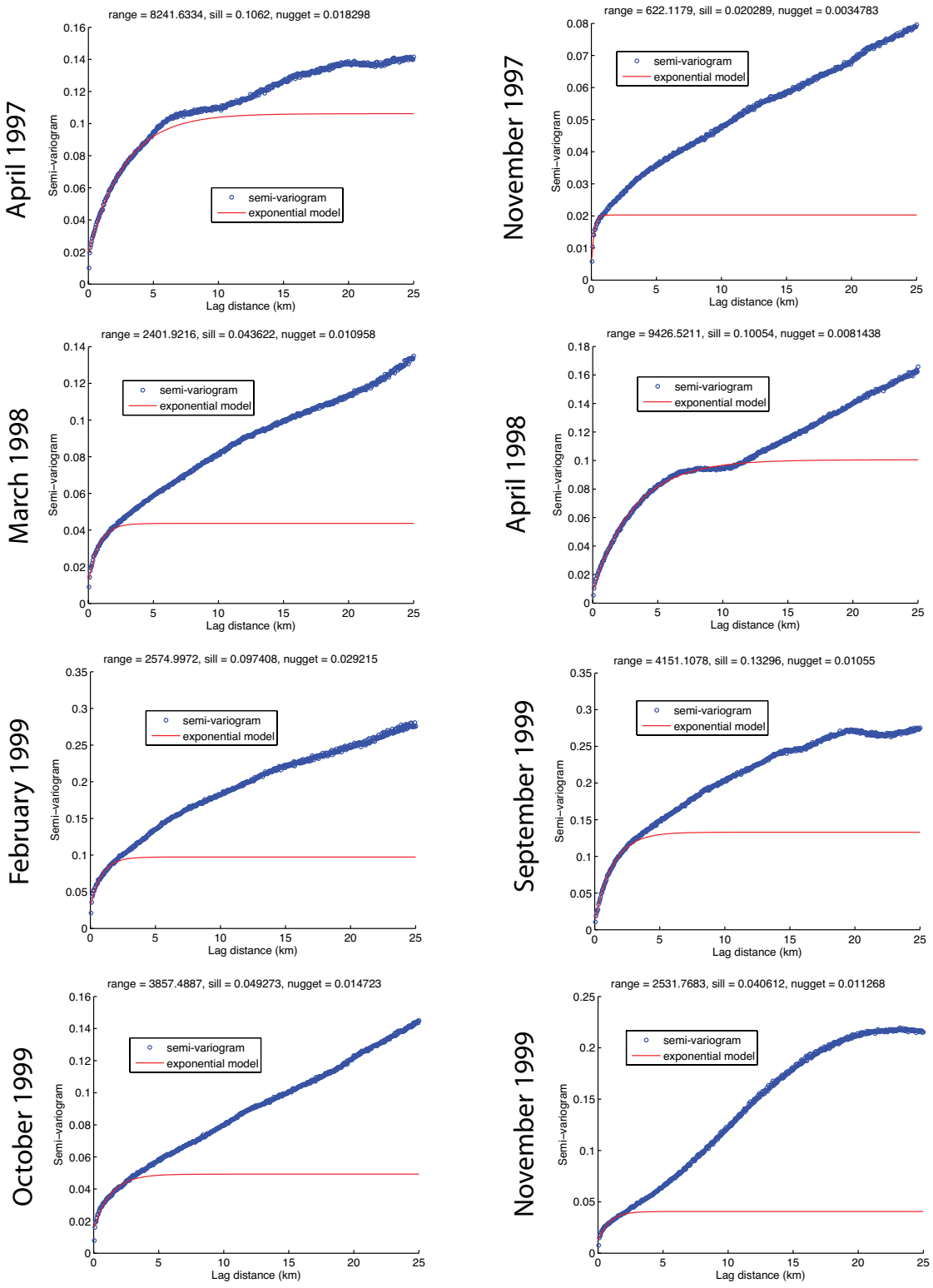

Figure 7.12: Semi-variograms and models for deformation acquisition times April 1997 – November 1999.

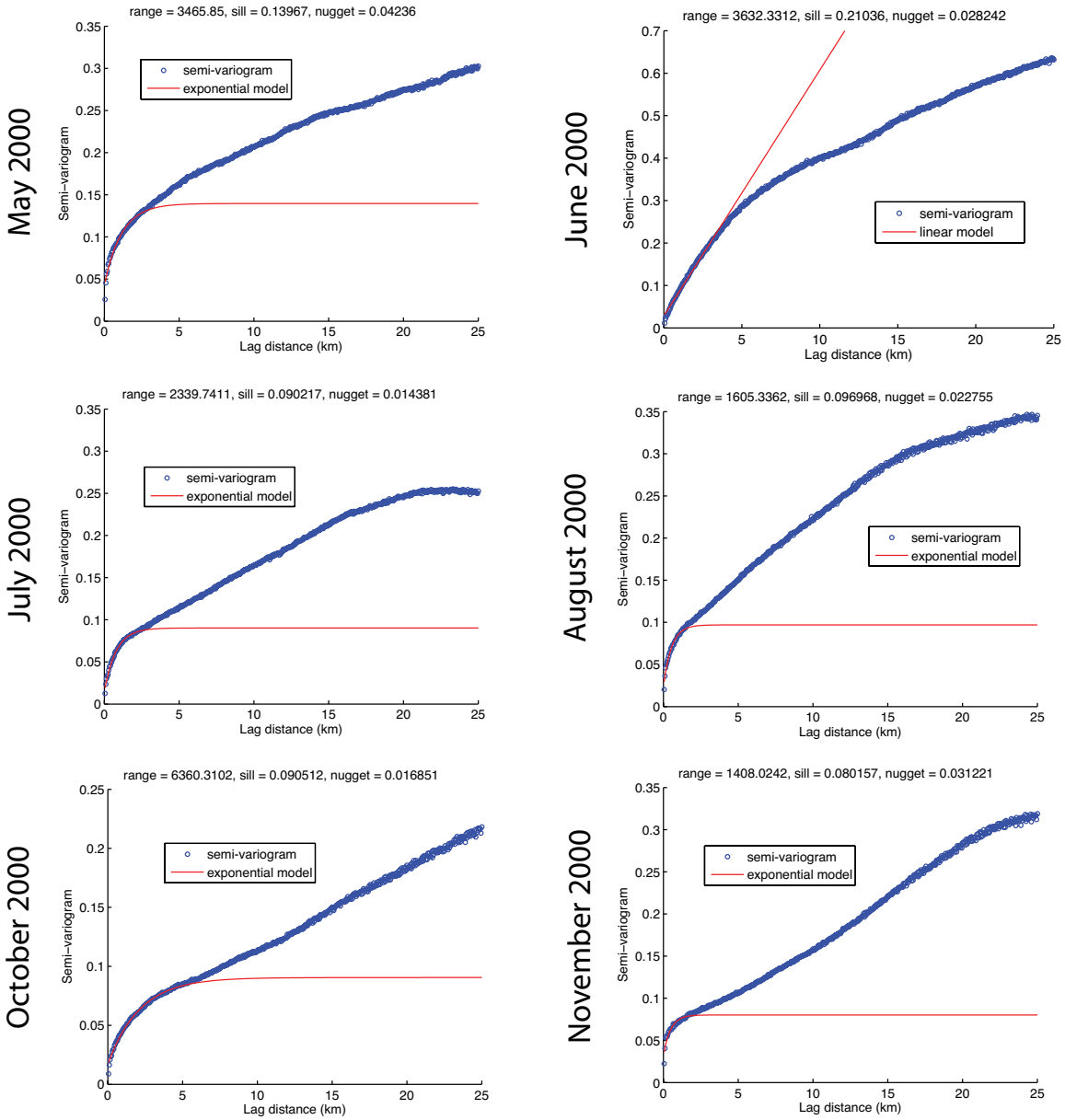

Figure 7.13: Semi-variograms and models for deformation acquisition times May 2000 – November 2000.

7.3.3 Semi-variogram analysis of Δh

We investigated the spatial variability of the change in hydraulic head (*Δh*) by calculating the semi-variogram using codes developed in MATLAB. The sample size for this analysis was much smaller than that of the deformation data analysis, as only 11 wells were used (as described in Section 4.2). We began this analysis by investigating the time period June 19, 2000 – July 24, 2000, as there were *Δh* measurements at all 11 well locations. It is also the same time period as was investigated for the deformation semi-variogram in Figure 7.8. Figure 7.14 shows the semi-variogram (red markers) and the semi-variogram values for each individual lag distance (blue markers). Because the hydraulic head data are so spatially sparse there is only one sample for each lag distance.

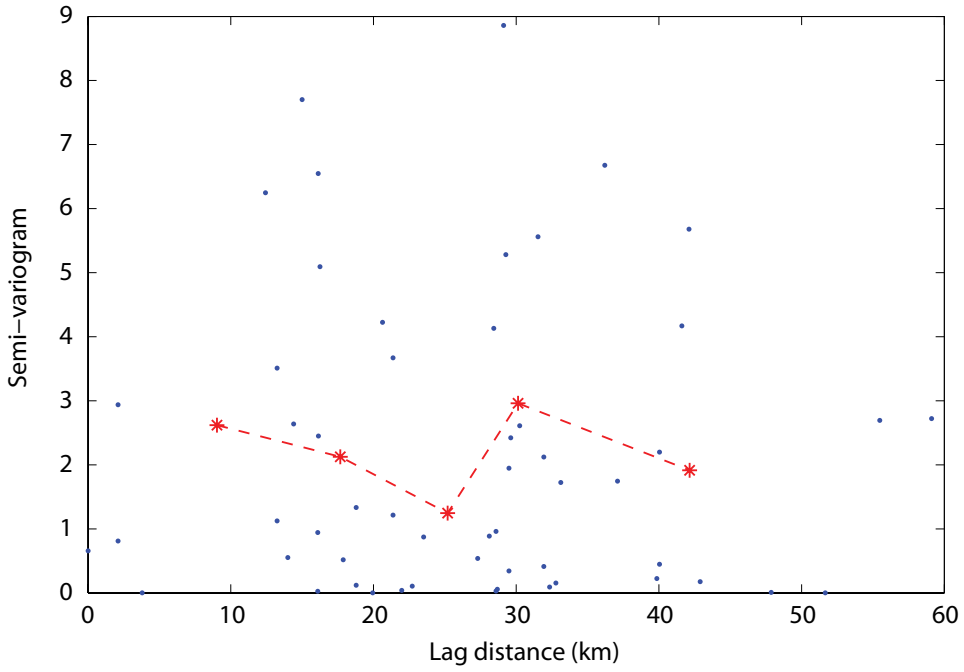

Figure 7.14: Semi-variogram for hydraulic head data from June 19, 2000 – July 24, 2000.

The semi-variogram in Figure 7.14 shows no distinct trend to suggest any specific spatial structure. Often variograms of hydraulic head data fit a quadratic model, such that wells close together show very similar hydraulic head values over some distinct distance [*Kitanidis,* 1997]. There is no evidence of this typical quadratic structure in this dataset. It is important to note that variograms are aimed at capturing the average spatial structure of a set of measurements. In this instance, only 11 measurements were available over large spatial scales (10's of kilometers), and hence the semi-variogram did not show any structure that is comparable to the structures observed in the deformation data. This highlights an inherent benefit of using InSAR deformation data for groundwater problems; the deformation data show finer spatial structures that are often not captured by hydraulic head data. These finer scale spatial structures contain important information about how the hydraulic head or subsurface geology is changing spatially. However, it also shows an inherent drawback to the analysis in the SLV; the deformation data need to be validated by the hydraulic head data that has a much lower spatial resolution. Because of this low spatial resolution, as seen in the semi-variogram in Figure 7.14, it is impossible to make a comparison of the spatial structure of these two datasets.

7.4 Comparison of hydraulic head data and deformation data at wells

The spatial variability of the deformation dataset allowed us to understand why the relationship between the hydraulic head measured at the well and the deformation measurements around wells ALA6, ALA7 and ALA8 was so variable. The short scale spatial structure in the deformation dataset showed that on average the deformation changes significantly within a 1 km radius of the wells. If we refer back to equation 2.26

this implies that either the hydraulic head is changing, the producing thickness is changing, S_{ske} is changing, or that the data contain atmospheric phase effects. In this section we will estimate the deformation directly at the well locations using the semi-variograms calculated in the previous section and a geostatistical technique called simple kriging.

7.4.1 Simple kriging of deformation data

SGeMS was used to perform the kriging of the deformation data. Kriging is a form of generalized linear regression that provides an optimal spatial estimator by minimizing the mean-squared-error between measured data and the estimated data at a given location [*Deutsch and Journel,* 1992]. Semi-variogram models, which characterize the spatial structure of the system, provide the optimal spatial estimator, which can then be used to estimate the variable in question at locations where it is unknown. i.e. at the well locations. In the Earth sciences many variants of kriging have been implemented, however the most basic form is known as simple kriging. We have chosen to use simple kriging over other more complicated forms because the technique implies that a valid mean for the dataset can be calculated, and because the deformation dataset is spatially dense this is a valid assumption.

Simple kriging, as implemented in SGeMS, does not incorporate the uncertainty of the data into the kriging algorithm. However, the kriged estimate of the deformation at the well location should be influenced by the uncertainty of the deformation at surrounding pixels. Therefore, a stochastic technique was implemented in order to incorporate this

uncertainty. For a single acquisition of deformation data, at a single selected pixel location, we randomly assigned a deformation from a Gaussian distribution. The Gaussian distribution was created with a mean equal to deformation measurement and a standard deviation equal to the uncertainty in the deformation measurement (as calculated in Chapter 6). We repeated this procedure 30 times, i.e. 30 realizations of the deformation datum. We found that the mean value of the 30 realizations was within 10% of the measured deformation. This process was repeated for all selected pixels within 2 km of the well location and all acquisition times. By using this method the kriged deformation will have an associated uncertainty that is influenced by both the uncertainty in the deformation data itself as well as the uncertainty associated with the kriging algorithm. We applied this process to the deformation data surrounding all 11 wells.

7.4.2 Linear regression of kriged deformation data and head data

In this section we apply the same linear regression, as described in section 7.2.1, on the hydraulic head data and the kriged deformation data at the 11 well locations. We begin by discussing the linear regression results at the three well investigated in section 7.2: ALA6, ALA7 and ALA8. We then discuss the results of the linear regression analysis for the remaining 8 wells .

The results of the linear regression of Δh and Δd at well ALA6 are shown in the left plot of Figure 7.15A. The deformation and the hydraulic head appear to be linearly related at this location ($R^2 = 0.875$). The grey circles signify the uncertainty in the InSAR measurement as calculated from the stochastic analysis previously described. The slope

of the regression line (S_{ke} = 4.44 ×10^{-3} +/- 2.64 ×10^{-4}) was then used to estimate the hydraulic head from the deformation measurements, shown in the plot on the right. We can see that the interpolated hydraulic head data are within the error bars of the estimated hydraulic head data 40% of the time (right plot Figure 7.15A). The uncertainty in the hydraulic head estimates is approximately +/- 0.5 m, which is much less than the uncertainty in the hydraulic head estimate from Chapter 5 (+/- 5 m at ALA6) when aquifer test parameters were used. As discussed in Chapter 5 an aquifer test was performed 300 m away from well ALA6 which resulted in an estimate of S = 1.4 ×10^{-3} +/- 2.8 ×10^{-4}. If we assume that S is a proxy for S_{ke}, i.e. the storage change due to the expansion and contraction of water is small (S_w), then we can compare these two results. We find that S_{ke} from the regression analysis is larger than S from the aquifer test. This could be due to a number of factors, e.g. uncertainty in the depth of the producing zone, spatial variability of S, and uncertainty due to atmospheric phase effects in the deformation data. However, it is encouraging that S and S_{ke} are the same order of magnitude.

The left plot of Figure 7.15B shows a linear relationship between the Δh and Δd data at ALA7 (R^2 = 0.846). The slope of the regression line is S_{ke} = 7.95 ×10^{-3} +/- 5.50 ×10^{-4}. Wells ALA6 and ALA7 are at the same location but are sampling different depths of the aquifer system. We also find that the estimated hydraulic head agrees with the interpolated hydraulic head at ALA7 60% of the time (see right plot of Figure 7.15B). The seasonality of both the estimated hydraulic head and the interpolated hydraulic head is the same.

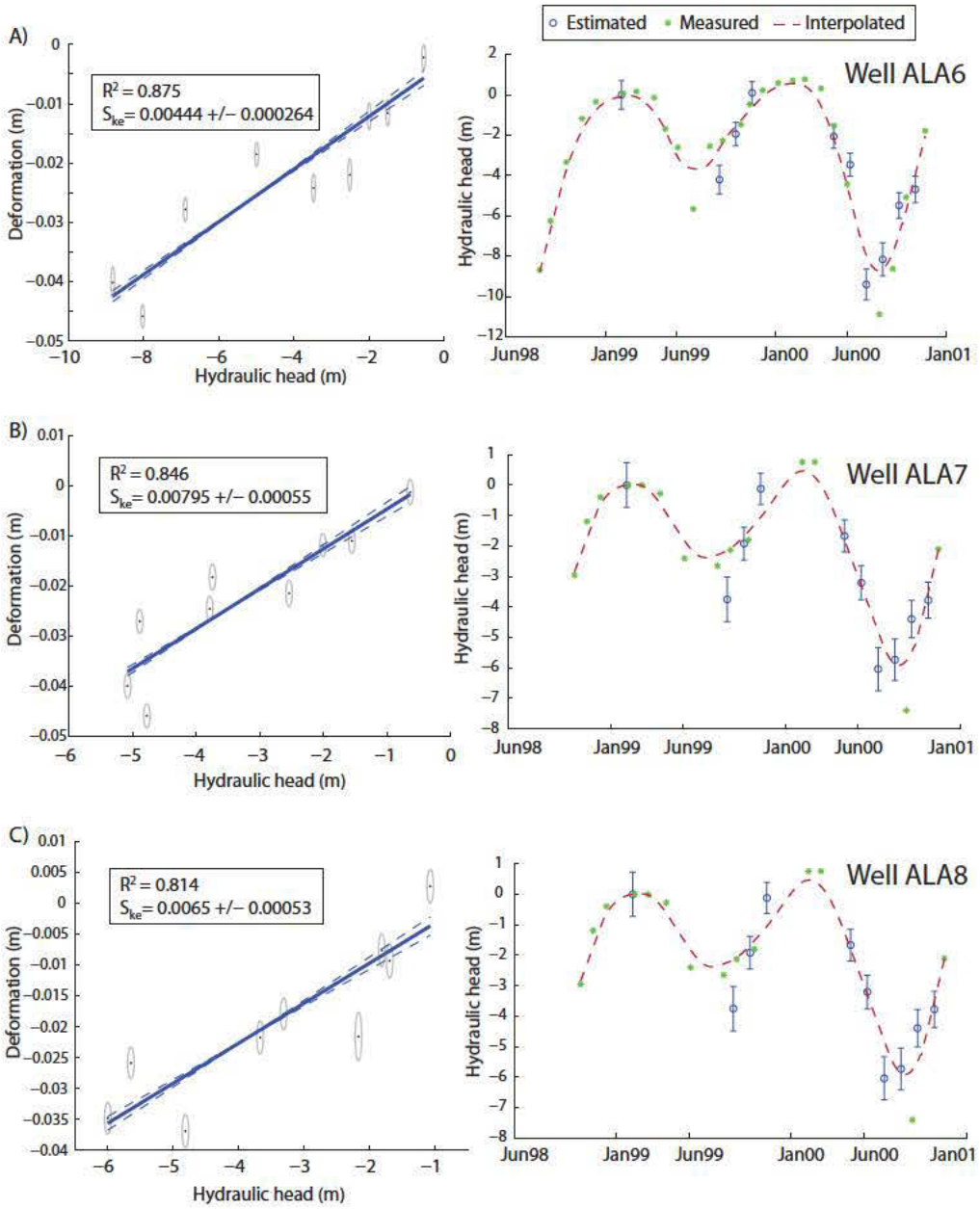

Figure 7.15: (Left plots) Linear regression of Δh and Δd at A) ALA6, B) ALA7, and C) ALA8. The data points show the uncertainty in the InSAR measurement (grey circles). The blue line is the best-fit linear regression, and the dashed lines show the uncertainty in that best fit. (Right plots) Estimated hydraulic head from InSAR deformation data (blue), hydraulic head measurements (green), and interpolated hydraulic head measurements (red dashed line) at A) ALA6, B) ALA7, and C) ALA8.

Well ALA8 is also located in the subsidence bowl area as seen in the raw interferograms, but approximately 2 km northwest of the ALA6/ALA7 wells. The regression of Δh and Δd in Figure 7.15C shows a linear relationship at well ALA8 ($R^2 = 0.814$). The slope of the regression line is $S_{ke} = 6.50 \times 10^{-3}$ +/- 5.3×10^{-4}, and we see that the estimated hydraulic head agrees with the measured hydraulic head 40% of the time (right plot 7.15C). We can see that the agreement between the estimated hydraulic head and the interpolated hydraulic head is worse during time periods with few hydraulic head measurements (see January 2000 – January 2001).

The results of the regression analysis for all 11 wells are shown in Table 7.1. In the work to follow we discuess how the quality of the linear relationship between the hydraulic head and the deformation varies based on magnitude of Δh, S_{ske} and b^* (see equation 2.26). If these variables are small at the well in question we do not expect the deformation to be large enough to be accurately measured by InSAR (see discussion in section 4.2).

Table 7.1 shows the aggregate variable, seasonal hydraulic head change (Δh_s), which is the average seasonal peak-to-trough change in hydraulic head (used previously in section 4.2). The three wells at the top of Table 7.1 (ALA6, ALA7 and ALA8) show large seasonal hydraulic head change and the regression analysis suggested a linear relationship between the deformation and the hydraulic head, as predicted in section 4.2. However, contrary to our predictions in section 4.2 the 8 other pairs of hydraulic head and

deformation data produced low or negative values for R^2 from the linear regression analysis, which indicates that a linear relationship should not be used to relate the two datasets. In the remainder of this section we will investigate why a linear relationship was not found at these 8 well locations.

Table 7.1: Regression analysis results and average seasonal hydraulic head change for each of the 11 well locations.

Well	R^2	S_{ke}	Δh_s
ALA6	0.8754	0.004439	7.6 m
ALA7	0.8459	0.007946	6.1 m
ALA8	0.8137	0.006497	4.3 m
ALA13	0.0865	0.000655	4.3 m
CON1	0.2382	0.003045	3.0 m
ALA4	0.0157	0.000961	3.0 m
CON2	0.0732	0.002299	1.8 m
RIO2	0.0205	0.000381	1.8 m
RG88	Negative	N/A	< 0.5 m
ALA15	Negative	N/A	< 0.5 m
ALA14	Negative	N/A	< 0.5 m

For the three wells at the bottom of Table 7.1, RG88, ALA15 and ALA14, the measured seasonal hydraulic head change was small (< 0.5 m). These were the three wells for which we did not have any information about the lithology of the producing aquifer system so assigned to a lithology of sand in section 4.2. Although our predicted deformation was larger than 1 cm at these well locations, it is possible that given more information about the lithology we would see that the S_{ske} value would be much smaller than that of a typical sand. It is also possible that the producing interval (b^*) for these wells was improperly estimated. If S_{ske} or b^* are smaller than we originally anticipated

then it is possible that the amount of deformation occurring at these well locations is too small to be accurately measured by InSAR.

There remain five wells, ALA13, CON1, ALA4, CON2 and RIO2, where Δh_s is large enough to result in accurate measurements of Δd, but a linear relationship is not observed between the deformation and the hydraulic head. At these five well locations S_{ske} and b^* may be smaller than we estimated in section 4.2. This result would affect the amount of deformation that occurred at the surface and the quality of the linear relationship between Δh and Δd.

Driller's logs and geophysical logs from wells CON2, ALA4 and CON1 show that these wells may be producing water from hard rock sediments, which have very low values for S_{ske}. The lower bound predictions of the deformation at these three well locations were below the sensitivity of the InSAR measurement (see section 4.2). The driller's log for well CON2 show that it is producing water from a zone of fractured volcanics, which generally have S_{ske} of zero. The driller's log for well ALA4 shows that the main production layers contain mainly hard rock materials, or hard packed sand/gravel at depths of over 1000 ft, also exhibiting low S_{ske} values. The driller's log for well CON1 also shows volcanics with low S_{ske} values. However, the geophysical logs identify the producing zones of the aquifer and do not indicate that the well was actually producing from the volcanic layers. Therefore, it is possible that at these three well locations the deformation is not large enough to be accurately measured by InSAR.

The final two wells for discussion in Table 7.1 are ALA13 and RIO2. Both wells are very deep, 1784 ft and 1396 ft respectively. ALA13 is located in the Closed Basin section of the SLV. In the Closed Basin water is being pumped from the unconfined aquifer into the Rio Grande River to meet the demands of the Rio Grande Compact. It was likely drilled deep in order to avoid the over 900 ft of blue clay sediments recorded in the driller's log. Even at the producing depth there are many thick intervals of what is known as "tan clay" in the SLV. For this reason we hypothesize that the relationship between deformation and hydraulic head at ALA13 is non–linear, i.e. the deformation may be experiencing a time lag in relation to the hydraulic head change (equation 2.18). The hydraulic head data were only recorded from 1999 – 2012, which coincides with only seven SAR acquisition times over the span of the 1999 – 2000 year. Therefore, a rigorous analysis of the time lag associated with the elastic deformation of the clays is not likely to produce useful results, and we did not attempt it.

The driller's log for well RIO2 does not show the same thick sequence of clay units, as it is located in the western part of the SLV near the Rio Grande River. However, it is possible that the estimates of S_{ske} and b^* that we provided in section 4.2 were too large. It is also true that the lower bound of the predicted deformation from section 4.2 was below the accuracy of the InSAR deformation measurement.

It is important to note that we have not discussed atmospheric phase effects as a factor that may affect the relationship between Δh and Δd at some of the well locations. Because our version of SBAS analysis does not include atmospheric temporal filtering (introduced

in Section 2.1.2), there will likely be a significant, unaccounted for, amount of atmospheric phase in each deformation time-series. However, given the results observed at wells ALA6, ALA7 and ALA8, it appears that given large changes in hydraulic head, and favorable hydrogeologic conditions (the magnitude of S_{ske} and b^*) the InSAR data and hydraulic head data can exhibit a reliable linear relationship.

7.4.3 Predicting hydraulic head at wells ALA6, ALA7 and ALA8

We used the linear fit between the hydraulic head data and kriged deformation data to predict hydraulic head at three of the well locations, ALA6, ALA7 and ALA8, for the entire InSAR data time span (1992 – 2000). Once again, we assumed elastic compaction, so that the slope of the regression line is an estimate of the elastic skeletal storage coefficient (S_{ke}) (equation 2.26). Figure 7.16 shows the predicted hydraulic head at the three well locations.

At each of the three well locations we can see that a seasonal trend in the predicted hydraulic head values does exist back to 1992. In the winter of 1996 we can see that the hydraulic head was predicted to be particularly high at all three wells. It is possible that the phase measured at the January 1996 acquisition time contains uncertainty due to atmospheric phase effects. Although no precipitation data were available through the RGDSS, we did investigate three well locations where hydraulic head was collected during 1996. At wells, SAG7, CON1 and ALA2 the measured hydraulic heads exhibited a larger high in 1996 than in 1992 – 1995 and 1997 – 2000.

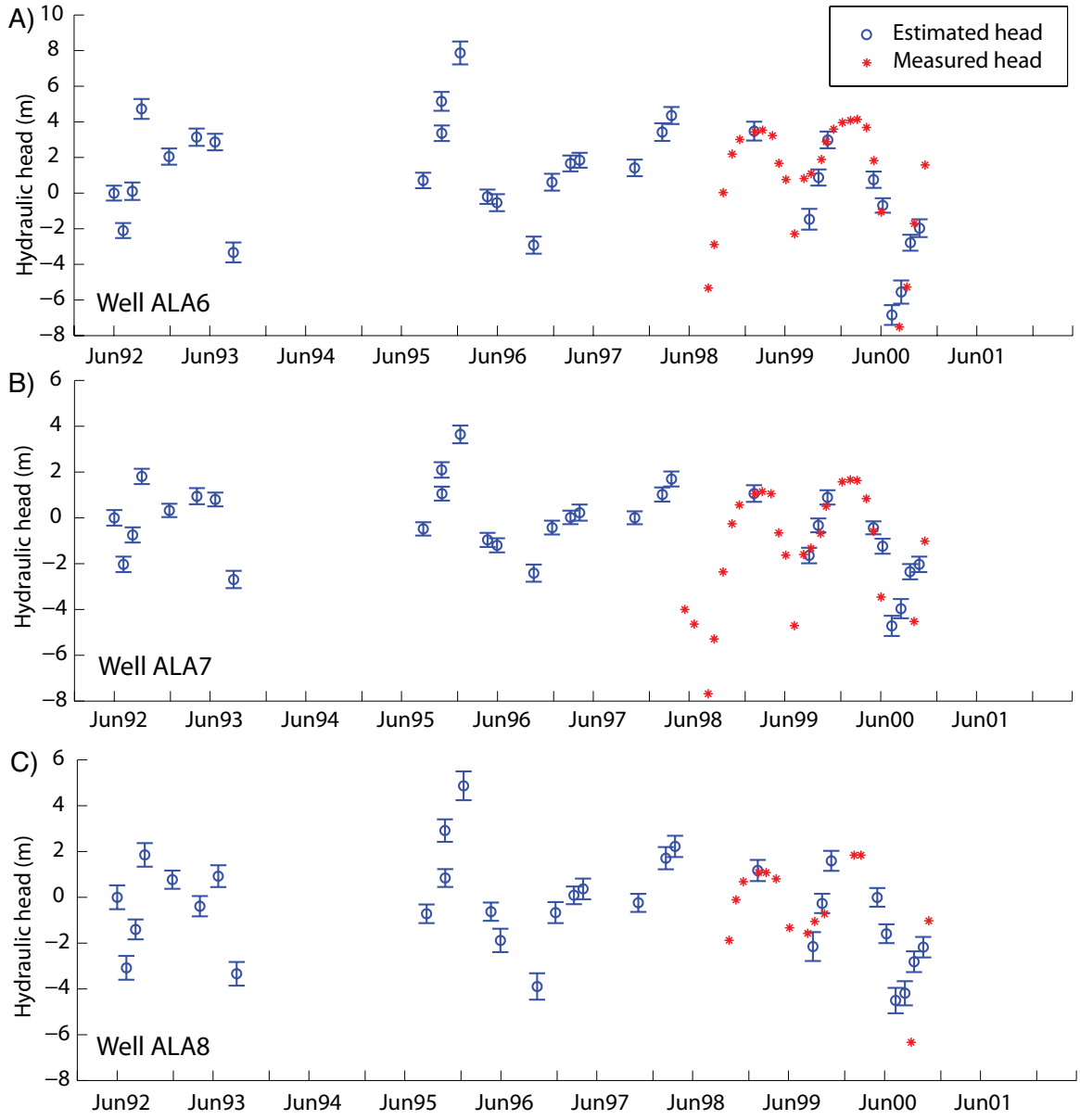

Figure 7.16: The estimated hydraulic head (blue markers) and the measured hydraulic head (red markers) at three well locations.

The approach used here is not valid if a) the aquifer system is undergoing inelastic deformation during the time periods without hydraulic head measurements, or b) the uncertainty due to atmospheric phase effects is large. In the case that the aquifer system is undergoing inelastic deformation, the elastic skeletal storage coefficient would not allow

for the prediction of hydraulic head back in time, and more hydraulic head data would be needed in order to understand the inelastic relationship. Also, if the unused InSAR deformation data in the regression analysis (from 1992 – 1998 in the SLV dataset) contain significant uncertainty due to atmospheric phase effects, the estimates of the hydraulic head would also be incorrect. However, as discussed in the previous paragraph, if nearby hydraulic head data are available it is possible to use those data to differentiate outliers due to atmospheric phase effects from periods with large changes in hydraulic head.

Although a spatially exhaustive valley wide comparison was not possible, the estimated hydraulic head at these three well locations provides information about the hydrologic system through time. The InSAR data have enabled us to look back through the 1990s, an important time for the management of the confined aquifer system in the SLV, and determine that the hydraulic head did not exhibit a negative linear trend at these locations from 1992 - 2000. This has implications for improving the estimation of hydraulic head at wells in other areas, agricultural or otherwise, with incomplete or sparsely sampled hydraulic head time series.

7.5 Conclusions

In this chapter we investigated how the relationship between InSAR deformation measurements and hydraulic head measurements can be used to interpolate and extrapolate the hydraulic head measurements in the San Luis Valley, Colorado through time. Initially we focused on the relationship between the hydraulic head measurements

and the deformation measurements around a given well location. In order to better understand how the relationship varied around a well we also investigated the spatial structure of the two datasets. Based on this analysis we were able to apply simple kriging to the deformation data, investigate the relationship directly at 15 well locations, and predict the hydraulic head change during a time when no hydraulic head data were measured at 3 well locations.

The spatial variability in the hydraulic head dataset was discussed in section 7.3.3. The variogram analysis showed that with only 11 hydraulic head measurements over 10,000 km^2, there was no identifiable spatial structure for the SLV hydraulic head dataset. In order for this type of research to be applied on a valley wide scale, it is critical that the hydraulic head dataset exhibit some spatial structure, i.e. the variogram analysis should show that the hydraulic head measurements made at the wells are spatially related.

We investigated the spatial structure of the InSAR deformation dataset in section 7.3.2. In Chapter 5, for the purposes of a preliminary analysis, we assumed that the deformation did not vary on scales < 1 km around three well locations. However, the variogram analysis in this chapter showed that on average the deformation does vary on scales < 1 km. The spatial structure of the deformation was also found to vary with time. The type of deformation we are trying to measure, i.e. rapid seasonally variable deformation due to groundwater pumping and recharge, makes it difficult to process the data and remove uncertainty due to atmospheric phase effects. Hence, it is difficult to determine which component of the spatial structure is due to deformation and which component is due to

atmospheric phase effects. If the data are sampled more regularly, on the order of two or three times per month, a processing technique could be developed to differentiate the seasonal deformation signal from the signal due to atmospheric phase effects.

The results of the deformation spatial analysis allowed for the kriging of the deformation data at the well locations. The kriged deformation estimates were then compared with hydraulic head measurements at 11 well locations, and showed a linear relationship at the three wells with the highest seasonal hydraulic head change (ALA6, ALA7 and ALA8). Wells with low seasonal changes in hydraulic head, low rock compressibility conditions or high clay content, did not exhibit a linear relationship between the InSAR deformation data and the hydraulic head data (as predicted by equations 2.18 and 2.26). These factors affect the amount of deformation at the surface that can be accurately measured using InSAR. Given that the two datasets do not agree at a majority of the well locations, it would be difficult to conduct a valley wide analysis of the deformation and hydraulic head in the SLV. However, in other aquifer systems that contain more compressible sediments and/or exhibit larger changes in hydraulic head, a regional-scale analysis might be possible.

At specific well locations the deformation data were used to fill in the temporal gaps in the hydraulic head dataset, see section 7.4.3. For wells ALA6, ALA7 and ALA8 this analysis showed that for the period 1992 – 2000 the hydraulic head did not decrease linearly with time. These results are especially important for the management of groundwater in the SLV, where the Confined Aquifer Rules decision requires that

hydraulic head levels remain above those measured from 1970 – 2000. Similarly, in other agricultural areas where irrigation uses groundwater from confined aquifers, the use of InSAR data at specific well locations may be able to provide information needed for better management.

Chapter 8

Conclusions

8.1 Summary of research

The overall goal of this thesis was to determine to what extent InSAR deformation data could be used to improve estimates of hydraulic head in the San Luis Valley, Colorado. The studies in Chapters 5 and 6, where we determined the quality and uncertainty in the InSAR deformation measurements, positioned us to answer this question in Chapter 7. Below is a restatement of the contributions of this thesis:

- Modification of a time-series processing algorithm to properly estimate deformation signals produced by seasonal pumping and recharge of groundwater aquifers in agricultural areas.
- Development of an extensive time-series of InSAR deformation maps for the San Luis Valley, Colorado, visualizing the spatial and temporal characteristics of land

surface deformation in this region.

- Verification that high quality InSAR deformation measurements can be made in agricultural areas like the San Luis Valley.
- Estimatation of the uncertainty in the InSAR deformation measurements and propagated this uncertainty through the data processing chain.
- Adaptation of a time-series processing algorithm such that high quality data are selected based upon the uncertainty of the final deformation time-series.
- Investigation of the spatial structure of the InSAR measured deformation dataset and the hydraulic head dataset in the SLV.
- Prediction of hydraulic head back in time at three well locations in the SLV.

In Chapter 5 we determined that the InSAR deformation data in the SLV was of high quality. We altered the standard SBAS processing algorithm to accommodate short-term seasonal changes in the deformation due to groundwater pumping and recharge. In altering the SBAS analysis algorithm we found that our data were more predisposed to contain atmospheric phase effects, which could add uncertainty into the InSAR deformation measurement. We determined that many of the small areas, left unwatered by the center-pivot irrigation systems, yield high quality InSAR data when processed using SBAS analysis. The InSAR deformation measurements showed the same seasonal periodicity as the hydraulic head data from monitoring wells. When hydraulic head was estimated from the InSAR data (with error bars on the order of meters), we found good agreement with the measured head values. However, we acknowledged that the errors are so large that these hydraulic head estimates would not provide the level of accuracy

required by the RGDSS. Hence, the next component of our research was to focus on the uncertainty in the InSAR deformation measurement.

In Chapter 6 we quantified the uncertainty in the InSAR deformation measurement due to decorrelation of radar signals. We found that the uncertainty due to decorrelation was small when compared to the uncertainty due to atmospheric phase effects. That being the case, we also investigated the efficacy of an algorithm that uses hydrologic data to identify scenes whose phase measurements may have been corrupted with atmospheric phase effects. Although the algorithm worked well with a synthetic dataset, we did not have a supplementary deformation dataset to validate the algorithm in the SLV. Finally, we investigated how we can achieve a set level of uncertainty in our InSAR deformation measurements by predetermining appropriate coherence thresholds for SBAS analysis. We quantified the relationship between the mean coherence, the standard deviation of the coherence and the standard deviation of the estimated deformation. These results will allow researchers to estimate the uncertainty of a dataset before performing all of the SBAS analysis processing steps. Quantifying the uncertainty in the InSAR measured deformation is critical if these data are to be used for groundwater applications as a basis for management decisions.

Groundwater sustainability in the SLV is of utmost importance to groundwater managers, as is the case in many agricultural areas. The managers in the SLV want to know: a) if inelastic deformation was occurring in the confined aquifer system, and b) the extent to which InSAR could be used to satisfy the requirements of the Confined Aquifer Rules

Decision. When evaluating the deformation time-series at the 11 wells where we predicted the highest magnitude of deformation, we concluded that no inelastic deformation was being detected from 1992 – 2000 (section 5.6). Having satisfied the first request of the groundwater managers we turned our focus on the problem of using the InSAR deformation data to improve our understanding of hydraulic head in the confined aquifer system.

In Chapter 7 we used the relationship between InSAR deformation measurements and hydraulic head measurements to temporally interpolate and extrapolate hydraulic head in the confined aquifer system of the San Luis Valley, Colorado. Given that the only validation for the deformation data was hydraulic head measurements made at wells, we began by attempting to understand how the relationship varied around three different wells. We found that the deformation was varying on a scale less than 1 km around the well locations. We proceeded to investigate the spatial structure of both the deformation and hydraulic head datasets. The deformation dataset exhibited spatial structures that could be captured by analytical semi-variogram models. However, the hydraulic head dataset was too sparsely sampled spatially to draw any conclusions about spatial structure. We were then able to apply simple kriging to the deformation data using the semi-variogram models previously calculated. The relationship between hydraulic head and deformation was explored directly at 11 well locations. Based on these results and the known uncertainty of the InSAR deformation measurements we investigated the conditions under which we were able to observe a linear relationship between InSAR measured deformation and hydraulic head. Given that the two datasets did not show a

linear relationship at a majority of the well locations, it was impossible to perform a valley wide analysis of the deformation and hydraulic head in the SLV. However, in other aquifer systems that contain more compressible sediments and/or exhibit larger changes in hydraulic head, a regional-scale analysis would be possible.

At three specific well locations, ALA6, ALA7 and ALA8, we were able to achieve the overall goal for this thesis. The InSAR measured deformation data were used to fill in temporal gaps in the hydraulic head dataset. We see InSAR data as providing a new way to complement expensive and spatially sparse groundwater monitoring wells with a more economical method of collecting field data. The incorporation of InSAR data could be an affordable way to centralize systems for the monitoring of groundwater aquifers.

8.2 Opportunities for future research

Although a number of researchers have investigated groundwater problems using InSAR deformation data, there are still many avenues for future research.

At the most basic level it is important that research continues in agricultural areas. Although the data are of lower quality than in urban/arid areas, groundwater management in these areas is of utmost importance. A number of satellites are now collecting SAR data at longer wavelengths, which is more ideal for vegetated areas. In this thesis we have shown that by altering processing techniques and using subsidiary data we can process even the shorter wavelength data and achieve accurate results.

There still exist many components of the SBAS analysis algorithm that could be improved to facilitate the use of InSAR data for groundwater applications. In agricultural areas where the amplitude of the seasonal signal changes from year to year, differentiating seasonal signals from phase change due to atmospheric phase effects becomes difficult. However, as mentioned briefly in Chapter 6 it may be possible to use pumping data, i.e. extraction rates or volume of water extracted, as prior information when applying the low-pass deformation model. The pumping data could be used to determine when the onset of seasonal subsidence should occur each year. Using pumping data would also be advantageous because it is often more readily available to groundwater managers than hydraulic head data.

Although we were able to predict hydraulic head at a number of locations in the SLV, the overall goal of this research was to be able to do so for the entire SLV. We believe that future research should focus on data driven applications rather than working with large over parameterized groundwater flow models. It is possible that given the right dataset, where the deformation was large enough and you had enough hydraulic head measurements for calibration, that a large-scale analysis could be performed. A number of stochastic techniques employ a data driven approach, e.g. Bayesian Maximum Entropy and Artificial Neural Networks, and could be used to interpolate between the hydraulic head measurements made in wells. These techniques would work well whether elastic or inelastic deformation was taking place.

The spatial analysis of the InSAR deformation data and hydraulic head data was a component of the thesis that could be improved upon given more spatially dense hydraulic head measurements. Alternatively, some simple synthetic studies investigating the semi-variogram models for phase change due to atmospheric phase effects and deformation due to hydraulic head change would be very useful during the implementation of the stochastic methods described above. Characterizing correlation lengths for specific areas of aquifer systems may even be able to differentiate spatial changes in hydrogeologic facies. This too could be investigated through a number of simple synthetic examples.

This thesis focused directly on the link between deformation and hydraulic head in order to satisfy the requirements of the Confined Aquifer Rules Decision. However, as was discovered during the process of evaluating the hydraulic head data, the quantity of data available was quite small. In the SLV and in many other agricultural areas with groundwater management issues, local and state governments have begun to regulate groundwater withdrawals. Because of these regulations monitoring devices have been placed on wells in order to determine the extraction rates. If we know that the main cause for the hydraulic head change seasonally is due to the extraction of water then it might be possible to avoid the middle parameter (hydraulic head change) and calibrate directly to the forcing function (the pumping of the well). If it could be shown that this type of calculation is simpler and legally easier to regulate then it is possible that groundwater management policy could change. Instead of the Confined Aquifer Rules decision

requiring that the hydraulic head remain between levels measured from 1970 – 2000, it could describe some sustainable extraction rate for each well.

As recently done in California with the passage of Senate Bill 6, it is likely that legislation will be put in place in many western states with requirements to monitor and report hydraulic head or extraction rates. With further development, we are optimistic that InSAR could provide the measurements to cost effectively meet the needs of such legislation, thus facilitating the implementation and adoption of the legislation. If we are to use monitoring of groundwater aquifers to effectively meet the global challenge of managing our water resources, we need robust, reliable, cost-effective forms of monitoring. We believe that InSAR and other satellite-based methods of data acquisition have great potential to address this need, thus leading to improved methods of groundwater management.

References

Agram, P. S. (2010), Persistent scatterer interferometry in natural terrain, Stanford University.

Amelung, F., D. L. Galloway, J. W. Bell, H. A. Zebker, and R. J. Laczniak (1999), Sensing the ups and downs of Las Vegas: InSAR reveals structural control of land subsidence and aquifer-system deformation, *Geo*, *27*(6), 483-486.

Anderssohn, J., H. U. Wetzel, T. R. Walter, M. Motagh, Y. Djamour, and H. Kaufmann (2008), Land subsidence pattern controlled by old alpine basement faults in the Kashmar Valley, northeast Iran: results from InSAR and levelling, *GeoJI*, *174*(1), 287-294.

Anderssohn, J., M. Motagh, T. R. Walter, M. Rosenau, H. Kaufmann, and O. Oncken (2009), Surface deformation time series and source modeling for a volcanic complex system based on satellite wide swath and image mode interferometry: The Lazufre system, central Andes, *RSEnv*, *113*, 2062-2075, DOI: 10.1016/j.rse.2009.05.004.

Barber, B. C. (1993), The phase statistics of a multichannel radar interferometer, *Waves in Random Media*, *3*(4), 257-266.

Batu, V. (1998). *Aquifer hydraulics: a comprehensive guide to hydrogeologic data analysis*. Wiley-Interscience.

Bawden, G. W., W. Thatcher, R. S. Stein, K. W. Hudnut, and G. Peltzer (2001), Tectonic contraction across Los Angeles after removal of groundwater pumping effects, *Natur*, *412*(6849), 812-815.

Bell, J. W., F. Amelung, A. Ferretti, M. Bianchi, and F. Novali (2008), Permanent scatterer InSAR reveals seasonal and long-term aquifer-system response to groundwater pumping and artificial recharge, *WRR, 44*(W02407), DOI: 10.1029/2007WR006152.

Berardino, P., G. Fornaro, R. Lanari, and E. Sansosti (2002), A New Algorithm for Surface Deformation Monitoring Based on Small Baseline Differential SAR Interferograms, *ITGRS*, *40*(11), 2375-2383.

Biot, M. A. (1941), General theory of three-dimensional consolidation, *JAP*, *12*, 155-164.

Canuti, P., N. Casagli, P. Farina, A. Ferretti, F. Marks, and G. Menduni (2006), Analysis of subsidence phenomena in the Arno river basin using radar interferometry, *Giornale di Geologia Applicata 4*, 131-136.

Calderhead, A. I., R. Therrien, A. Rivera, R. Martel, J. Garfias (2011), Simulating pumping-induced regional land subsidence with the use of InSAR and field data in the Toluca Valley, Mexico, *Advances in Water Resources*, *34*, 83-97.

Carslaw, H. S., and J. C. Jaeger (1959), Conduction of heat in solids. , edited, Oxford at the Clarendon Press, London.

Chatterjee, R., B. Fruneau, J. Rudant, P. Roy, P. L. Frison, R. Lakhera, V. Dadhwal, and R. Saha (2006), Subsidence of Kolkata (Calcutta) City, India during the 1990s as observed from space by differential synthetic aperture radar interferometry (D-InSAR) technique, *RSEnv*, *102*(1), 176-185.

Chen, C. W., and H. Zebker (2002), Phase Unwrapping for Large SAR Interferograms: Statistical Segmentation and Generalized Network Models, *ITGRS*, *40*(8), 1709-1719.

Deutsch, C. V., & Journel, A. G. (1992). *Geostatistical software library and user&s guide* (Vol. 1996). New York: Oxford university press.

Emery, P. A., R. J. Snipes, J. M. Dumeyer, and J. M. Klein (1973), Water in the San Luis Valley, south-central Colorado, *Colorado Water Resources Circular*, *18*, 27.

Fattahi, H., and F. Amelung (2013), DEM Error Correction in InSAR Time Series, *Geoscience and Remote Sensing, IEEE Transactions on*, *PP*(99), 1-11, DOI: 10.1109/tgrs.2012.2227761.

Ferretti, A., C. Prati, and F. Rocca (2000), Nonlinear subsidence rate estimation using permanent scatterers in differential SAR interferometry, *ITGRS*, *38*(5), 2202-2212.

Ferretti, A., C. Prati, and F. Rocca (2001), Permanent Scatterers in SAR Interferometry, *ITGRS*, *39*(1), 8-20.

Fetter, C. W. (2001), Applied Hydrogeology. , edited, Prentice-Hall Inc., Upper Saddle River, New Jersey.

Galloway, D. L., K. W. Hudnut, S. E. Ingebritsen, S. P. Phillips, and G. Peltzer (1998), Detection of aquifer system compaction and land subsidence using interferometric synthetic aperture radar, Antelope Valley, Mojave Desert, California, *WRR*, *34*(10), 2573-2585.

Gonzalez, P., J., and J. Fernandez (2011), Error estimation in multitemporal InSAR deformation time series, with application to Lanzarote, Canary Islands, *JGR*, *116*(B10404), DOI: 10.1029/2011JB008412.

Goodman, N. R. (1963), Statistical Analysis Based on a Certain Multivariate Complex Gaussian Distribution (An Introduction), *The Annals of Mathematical Statistics*, *34*(1), 152-177.

Guarnieri, A. M., and S. Tebaldini (2007), Hybrid Cramer-Rao Bounds for Crustal Displacement Field Estimators in SAR Interferometry, *Signal Processing Letters, IEEE*, *14*(12), 1012-1015, DOI: 10.1109/lsp.2007.904705.

Hanssen, R. F. (1998), Assessment of the role of atmospheric heterogeneities in ERS tandem SAR interferometry, Delft University, Delft, Netherlands.

Hanssen, R. F. (2001), *Radar Interferometry – Data Interpretation and Error Analysis*, Kluwer Academic Publishers.

Harmon, E. (2001), RGDSS Ground Water, Task 28 – Confined Aquifer Testing Piezometer no. 5, Three S Ranch well 15926R, HRS Water Consultants Inc.

Hearne, G. A., and J. D. Dewey (1988), Hydrologic analysis of the Rio Grande Basin north of Embudo, New Mexico, Colorado and New Mexico, *U.S. Geological Survey Water-Resources Investigations Report*, *86–4113*, 244.

Hoen, W. (2001), A Correlation-based Approach to Modeling Interferometric Radar Observations of the Greenland Ice Sheet, Stanford University, Stanford.

Hoffmann, J., H. Zebker, D. Galloway, and F. Amelung (2001), Seasonal subsidence and rebound in Las Vegas Valley, Nevada, observed by synthetic aperture radar interferometry, *WRR*, *37*(6), 1551-1566.

Hoffmann, J. (2003), The Application of Satellite Radar Interferometry to the Study of Land Subsidence over Developed Aquifer Systems, 229 pp, Stanford University, Stanford.

Hoffmann, J., D. L. Galloway, and H. A. Zebker (2003), Inverse modeling of interbed storage parameters using land subsidence observations, Antelope Valley, California, *WRR, 39*(2), 1031-1043, DOI: 10.1029/2001WR001252.

Hooper, A., H. Zebker, P. Segall, and B. Kampes (2004), A new method for measuring deformation on volcanoes and other natural terrains using InSAR persistent scatterers, *GeoRL*, *31*(L23611), DOI: 10.1029/2004GL021737.

HRS Water Consultants Inc., (2002), Task 32 Hydrogeologic Database Refresh Final Memorandum, Map 35. For Rio Grande Decision Support System, Colorado Water Conservation Board and Colorado Division of Water Resources.

Hung, W. C., C. Hwang, C. P. Chang, J. Y. Yen, C. H. Liu, and W. H. Yang (2010), Monitoring severe aquifer-system compaction and land subsidence in Taiwan using multiple sensors: Yunlin, the southern Choushui River Alluvial Fan, *Environmental Earth Sciences*, *59*(7), 1535-1548.

Ireland, R. L., J. F. Poland, and F. S. Riley (1984), Land subsidence in the San Joaquin Valley, California, as of 1980, *U.S. Geological Survey Professional Paper*, *437-I, 93*, 1984.

Jorgensen, D. G. (1980), Relationships between basic soils – engineering equations and basic ground-water flow equations, *Water-Supply Paper U.S. Geological Survey*, *2064*.

Kitanidis, P. K. (1997). *Introduction to geostatistics: applications in hydrogeology*. Cambridge University Press.

Knospe, S., and S. Jonsson (2010), Covariance Estimation for dInSAR Surface Deformation Measurements in the Presence of Anisotropic Atmospheric Noise, *IEE Transactions on Geoscience and Remote Sensing*, *48*(4), DOI: 10.1109/TGRS.2009.2033937.

Kuenhold, O. J. (2006), Confined Aquifer New Use Rules for Division 3: Findings of Fact, Conclusions of Law, Judgement and Decree, edited, District Court, Water Division No. 3, Colorado.

Kwoun, O.-l., L. Zhong, C. Neal, and C. Wicks (2006), Quiescent deformation of the Aniakchak Caldera, Alaska, mapped by InSAR, *Geo*, *34*(1), 5-8, DOI: 10.1130/G22015.1.

Larsen, Y., G. Engen, T. R. Lauknes, E. Malnes, and K. A. Hogda (2005), A generic differential InSAR processing system, with applications to land subsidence and SWE retrieval, paper presented at Advances in SAR Interferometry from ENVISAT and ERS missions (Fringe 2005), ESA ESRIN, Frascati, Italy, November 28 - December 2, 2005.

Lauknes, T. R. (2004), Long-Term Surface Deformation Mapping using Small-Baseline Differential SAR Interferograms, 100 pp, University of Tromso, Tromso.

Lauknes, T. R., J. Dehls, A. Hogda, Y. Larsen, and D. J. Weydahl (2005), A comparison of SBAS and PS ERS InSAR for subsidence monitoring in Oslo, Norway, *In Proc. FRINGE-2005 Workshop, Frascati, 28 Nov–2 Dec*.

Leake, S. A., and D. E. Prudic (1991), Documentation of a computer program to simulate aquifer-system compaction using the modular finite-difference ground-water flow model, *USGS Techniques of Water-Resources Investigations*, *6*(A2), 68.

Lee, J., A. R. Miller, and K. W. Hoppel (1994), Statistics of phase difference and product magnitude of multi-look processed Gaussian signals, *Waves in Random Media*, *4*(3), 307-319.

Massonnet, D., and K. L. Feigl (1998), Radar interferometry and its application to changes in the Earth's surface, *RvGeo*, *36*(4), 441-500.

Meyer, B., R. Armijo, D. Massonnet, J. B. d. Chabalier, C. Delacourt, J. C. Ruegg, J. Achache, P. Briole, and D. Papanastassiou (1996), The 1995 Grevena (Northern Greece) Earthquake: Fault model constrained with tectonic observations and SAR interferometry, *GeoRL*, *23*(19), 2677-2680.

Onn, F., and H. Zebker (2006), Correction for interferometric synthetic aperture radar atmospheric phase artifacts using time series of zenith wet delay observations from a GPS network, *JGR*, *111*(B09102), 16, DOI: 10.1029/2005JB004012

Poland, J. F., B. E. Lofgren, R. L. Ireland, and R. G. Pugh (1975), Land Subsidence in the San Joaquin Valley, California, as of 1972, *U.S. Geological Survey Professional Paper 437-H, 78*.

Reeves, J. A., R. J. Knight, H. Zebker, W. A. Schreüder, P. S. Agram, and T. R. Lauknes (2011), High quality InSAR data linked to seasonal change in hydraulic head for an agricultural area in the San Luis Valley, Colorado, *WRR*, *47*, DOI: 10.1029/2010WR010312.

Reeves, J.A., R. Knight, H.A. Zebker, (*in revision for IEEE Geoscience and Remote Sensing*), An analysis of the uncertainty in InSAR deformation measurements for groundwater applications.

RGDSS (2005), Rio Grande Decision Support System Groundwater Model as of July 29, 2005, Principia Mathematica, Lakewood, Colorado.

Riley, F. S. (1969), Analysis of borehole extensometer data from central California, *International Association of Scientific Hydrology Publication*, *89*, 423-431.

Riley, F. S. (1998), Mechanics of aquifer systems – The scientific legacy of Dr. Joseph F. Poland, in Borchers, J.W., ed., Land subsidence case studies and surrent research: Proceedings of the Dr. Joseph F. Poland Symposium on Land Subsidence, *Association of Engineering Geologists Special Publication*, *8*(13-27).

Rocca, F. (2007), Modeling Interferogram Stacks, *Geoscience and Remote Sensing, IEEE Transactions on*, *45*(10), 3289-3299, DOI: 10.1109/tgrs.2007.902286.

Schmidt, D. A., and R. Burgmann (2003), Time-dependent land uplift and subsidence in the Santa Clara valley, California, from a large interferometric synthetic aperture radar data set, *JGR, 108*(B9), 2416-2428, DOI: 10.1029/2002JB002267.

Scott, R. F. (1963), Principles of soil mechanics, IV: Settlement and consolidation od clay, *Engineering News-Record*, *95*(22), 874-878.

Simons, M., Y. Fialko, and L. Rivera (2002), Coseismic Deformation from the 1999 Mw 7.1 Hector Mine, California, Earthquake as Inferred from InSAR and GPS Observations, *Bulletin of the Seismological Society of America*, *92*(4), 1390-1402.

Sneed, M., J. T. Brandt, and C. V. W. District (2007), *Detection and Measurement of Land Subsidence Using Global Positioning System Surveying and Interferometric Synthetic Aperture Radar, Coachella Valley, California, 1996-2005*, US Department of the Interior, US Geological Survey.

Terzaghi, K. (1925), *Structure and volume of voids in soils, translated from Erdbaummechanik auf Bodenphysikalischer Grundlage, in From Theory to Practice in Soil Mechanics*, John Wiley and Sons, New York.

Todd, D. K. (1980), *Groundwater Hydrology*, 2nd ed., John Wiley, New York.

Tough, R. J. A., D. Blacknell, and S. Quegan (1995), A Statistical Description of Polarimetric and Interferometric Synthetic Aperture Radar Data, *Mathematical and Physical Sciences*, *449*(1937), 567-589.

Treuhaft, R. N., & Lanyi, G. E. (1987). The effect of the dynamic wet troposphere on radio interferometric measurements. *Radio Science*, *22*(2), 251-265.

Usai, S. (2003), A Least Squares Database Approach for SAR Interferometric Data, *ITGRS*, *41*(4), 753-760, DOI: 10.1109/TGRS.2003.810675.

Watson, K. M., Y. Bock, and D. T. Sandwell (2002), Satellite interferometric observations of displacements associated with seasonal groundwater in the Los Angeles basin, *JGR, 107*(B4), DOI: 10.1029/2001JB000470.

Wiley, B. A., and D. A. Schmidt (2010), Deciphering vertical deformation and poroelastic parameters in a tectonically active fault-bound aquifer using InSAR and well level data, San Bernardino basin, California, *GeoJI*, *181*, 1185 - 1200, DOI: 10.1111/j.1365-246X.2010.04568.x

Wisely, B. A., and D. A. Schmidt (2010), Deciphering vertical deformation and poroelastic parameters in a tectonically active fault-bound aquifer using InSAR and well level data, San Bernardino basin, California, *GeoJI*, *181*, 1185 - 1200, DOI: 10.1111/j.1365-246X.2010.04568.x

Zebker, H., and J. Villasenor (1992), Decorrelation in interferometric radar echoes, *ITGRS*, *30*(5), 950-959.

York, D., Evensen, N. M., Martínez, M. L., & Delgado, J. D. B. (2004). Unified equations for the slope, intercept, and standard errors of the best straight line.*American Journal of Physics*, *72*, 367.

Zebker, H., C. L. Werner, P. A. Rosen, and P. Hensley (1994), Accuracy of topographic maps derived from ERS-1 interferometric radar, *ITGRS*, *32*(4), 823-836.

Zebker, H., P. A. Rosen, and P. Hensley (1997), Atmospheric effects in interferometric synthetic aperture radar surface deformation and topographic maps, *JGR*, *102*(B4), 7547-7563.